Clemson University
TigerPrints

All Dissertations | Dissertations

12-2012

Sensitivity Analysis in Magnetic Resonance Elastography and a Local Wavelength Reconstruction based on Wave Direction

Christopher Gillam
Clemson University, cgillam0513@gmail.com

Follow this and additional works at: https://tigerprints.clemson.edu/all_dissertations

 Part of the Applied Mathematics Commons

Recommended Citation
Gillam, Christopher, "Sensitivity Analysis in Magnetic Resonance Elastography and a Local Wavelength Reconstruction based on Wave Direction" (2012). *All Dissertations*. 1023.
https://tigerprints.clemson.edu/all_dissertations/1023

This Dissertation is brought to you for free and open access by the Dissertations at TigerPrints. It has been accepted for inclusion in All Dissertations by an authorized administrator of TigerPrints. For more information, please contact kokeefe@clemson.edu.

Sensitivity Analysis in Magnetic Resonance Elastography and a Local Wavelength Reconstruction based on Wave Direction

---

A Dissertation
Presented to
the Graduate School of
Clemson University

In Partial Fulfillment
of the Requirements for the Degree
Doctor of Philosophy
Mathematical Sciences

---

by
Christopher John Gillam
December 2012

Accepted by:
Dr. Jeong-Rock Yoon, Committee Chair
Dr. Jim Brannan
Dr. Vincent Ervin
Dr. Taufiquar Khan

Abstract

Magnetic resonance elastography (MRE) is an example of emerging hybrid imaging techniques for the detection of early stage cancer. MRE utilizes interior data for its inverse problems, which greatly reduces the ill-posedness from which most traditional inverse problems suffer.

In this thesis, we first establish a sensitivity analysis for viscoelastic scalar medium with complex wave number and compare it with the purely elastic case. Also we estimate the smallest detectable inclusion for breast and liver, which is about twice larger than using the purely elastic model. We also found the existence of optimal frequency (50 Hz) that maximizes the detectability when the Voigt model is used.

Second, we propose a local wavelength reconstruction based on the wave direction estimate for purely elastic medium. The main observation is that the wave looks primarily like a plane wave on a small window. On the small window, we first estimate the wave direction by solving a one dimensional optimization problem related to the minimum variance of shifted identical signals. Then along the wave direction, we use a non-periodic Fourier transform to reconstruct the wave number. This algorithm is extremely resilient to the noise and combined with another direct inversion method, this hybrid reconstruction becomes accurate as well. Extensive test reconstructions on simulated and experimental data provided by the Mayo Clinic are included in this thesis. For the viscoelastic medium, this local wavelength reconstruction method will need an additional parameter for a scaling factor which leads to a two dimensional minimization problem. A slight modification in the Fourier transform part will also need to be created which is left for future work.

Table of Contents

List of Tables

List of Figures

Chapter 1

Introduction

Many traditional inverse problems are based on the data measured on the boundary, such as electrical impedance tomography [8] and optical tomography [5]. These inverse problems are ill-posed, which leads to poor and unstable reconstruction of the region far from the boundary. To overcome this ill-posedness, recently a group of new imaging techniques have been developed. They use one physics to stimulate the body and another physics to measure the response. This use of hybrid imaging allows scientists to utilize the interior data to get a better reconstruction of the region far from the boundary. This thesis will focus on a particular hybrid imaging process, magnetic resonance elastography (MRE) which is used for detecting early stage cancer.

Traditional medical imaging techniques such as computed tomography (CT), magnetic resonance imaging (MRI), and ultrasonography have sometimes not been able to detect some types of cancerous tumors that physicians were able to detect using palpation [21]. The goal of MRE experiments is to reconstruct the mechanical properties, such as elasticity, of soft tissue that makes palpation such a viable tool. Moreover, MRE has the potential to detect small tumors that are deep within the body where palpation is not an option.

In MRE experiments, a vibrating plate placed on the skin surface creates a mechanical wave, which propagates into the human body. The MRE machine captures the wave using an MRI enhanced with a motion encoding gradient. Since the cancerous tissue has experimentally been found to be stiffer (up to 10 times) than the healthy surrounding tissue, it distorts the wave

propagation in the amplitude, phase and wave speed, which can be observed in the MRE data. See [22] for the data acquisition in MRE.

The first part of this thesis investigates the viability of MRE as a detection tool for cancerous tumor. It is believed that the rough estimate of the size of early stage cancer is around 2 to 3 mm in radius, but it is very hard to detect that small inclusion in the actual MRE experiments. This limitation for the smallest detectable tumor could be a result of poor experimental design, or perhaps, it could be an inherent mathematical/physical limit of the MRE process. Previous work [19] has given a mathematical definition and study of detectability for purely elastic scalar model. However, a more realistic model of human tissue is viscoelastic material. For viscoelastic material, it is expected that the detectability will be more difficult since the wave will partially decay before it reaches the region of interest. Chapter 4 analyzes the theoretical limit of tumor detectability using MRE with the viscoelastic model, after defining the model and providing a solution for a spherical inclusion in Chapters 2 and 3.

In Chapter 2, we derive the linear viscoelastic wave equation for isotropic medium, which is an acceptable model for human soft tissue. Taking the Fourier transform with respect to time, this model is reduced to the Helmholtz equation with complex wave number. Because we are interested in the smallest detectable tumor size, we assume, for convenience, the medium is decomposed into two regions; one is for the tumor and the other is for the surrounding healthy tissue. When the wave hits the tumor, some of the waves propagate through and some are scattered. Physically across the surface of tumor, the displacement and the normal stress must be continuous, which leads to a well established mathematical problem, a transmission problem for the Helmholtz equation.

The derived transmission problem from Chapter 2 possesses a well-known spherical Bessel and Hankel series solution for the purely elastic case with real wave number, when the tumor is assumed to be a ball [19]. This assumption is acceptable when the tumor is small, and recall that our main goal is to check the detectability of small tumor. In Chapter 3, we extend this spherical Bessel and Hankel series solution to viscoelastic medium with complex wave number.

In MRE experiments, any distortion in the measured displacement images may indicate the presence of a tumor. In Chapter 4, a mathematical definition of detectability is given based on the

change of amplitude of the wave at the center point of the tumor. This definition is mathematically pleasing because it gives a simple form, which allows us to analyze the effect on the detectability of several physical parameters such as size of inclusion, wave speed, and attenuation of wave in the tumor and background.

In Chapter 4, we also introduce three spring-dashpot models as examples of viscoelastic medium: Maxwell, Voigt, and Standard Linear Solid (SLS) models. For each model, we investigate the effects of the spring and dashpot constants to our definition of detectability. Furthermore, it is discovered that the Voigt model exhibits an optimal frequency for detectability, which is near 50 Hz for breast tissue. Using realistic parameters, this thesis also quantifies the smallest detectable tumor under noisy conditions. For example, if noise level is 5%, the smallest detectable tumor, for breast tissue is about 3 mm in radius and for liver tissue, the smallest detectable tumor is about 4 mm in radius.

The second part of this thesis discusses a reconstruction method of stiffness in MRE experiments assuming purely elastic medium. A common reconstruction method is the direct inversion including the algebraic inversion of the differential equation (AIDE) which directly inverts the motion equations or the Helmholtz equation to reconstruct the stiffness ([14][15][16][17][18][23][24]). For example, a simple algebraic inversion of the Helmholtz equation, $\Delta u + k^2 u = 0$, will give the wavenumber $k = \sqrt{-\Delta u/u}$. However, these methods are not stable with respect to noise because it requires taking derivatives. Thus areas of low signal-to-noise ratio (SNR) are troublesome. Also, regions where $u \approx 0$ will cause poor reconstructions. Some success has been obtained using these methods with data smoothing or a statistics based filter ([14][15][18]). Local frequency estimation (LFE) uses instantaneous frequency and lognormal quadrature wavelet filters which provide stable estimates but poor resolution around the boundaries of the inclusion [16]. Variational methods have also been used in MRE experiments but is time consuming because of its iterative nature ([29][30]) when it does not start with a good initial guess. In this thesis, we present a new local wavelength reconstruction which is extremely stable with respect to noise without filtering and which is non-iterative. Moreover, when combined with a direct inversion method suggested in [18], our final reconstruction maintains stability and enhances the resolution of the reconstructed image.

This reconstruction can also provide an initial guess to enhance the speed of iterative methods.

Our local wavelength reconstruction method is motivated by the observation that the measured wave from the MRE experiments looks primarily like a single plane wave on a small window. Under this observation, the wave direction is calculated using a "stacking curves" technique, which is a one dimensional minimization problem on a bounded domain. Once the wave direction is determined, crosscuts in that direction are taken and the wavenumber $k = \sqrt{\rho\omega^2/\mu}$ is estimated via a non-periodic Fourier transform technique. This reconstruction method is shown to be extremely resilient to noise when compared with another known direct inversion method [18]. Moreover, when combined with this other method, the resulting hybrid reconstruction provides an accurate and stable reconstruction. These reconstruction methods are tested and compared on simulated and experimental data provided from the Mayo Clinic.

Finally in the Appendix, a detailed statistical analysis of the wave direction "stacking curves" method is given. In this chapter, we study the expected error and variance of the cost functional that needs to be minimized, and it was found that noise can cause a shift in the minimum of the functions. However, this shift is not large enough to significantly affect the final reconstruction.

Chapter 2

Modeling

In an elastography experiment, a plate is attached to the skin, and it vibrates at a certain frequency. The plate generates a wave propagating into the body and magnetic resonance imaging (MRI) can capture this propagating wave using motion encoding gradient [22]. To model the wave propagation, we investigate the relationship between displacement $\mathbf{U}(x,t)$, stress $\sigma(x,t)$, and strain $\epsilon(x,t)$ as described in [7]. For isotropic viscoelastic medium (e.g. human soft tissue), our strain tensor is assumed to be linear:

$$\epsilon = \frac{1}{2}(\nabla \mathbf{U} + \nabla \mathbf{U}^T)$$

since displacement is small (a few microns) in MRE experiments. Since the material is viscoelastic, stress depends on past strain states with memory kernels λ^* and μ^*:

$$\sigma = \left[\int_{-\infty}^{t} \lambda^*(\mathbf{x}, t-\tau)\frac{\partial}{\partial \tau}\left(\nabla \cdot \mathbf{U}\right)\, d\tau\right]\, \mathrm{I}_{3\times 3} + 2\int_{-\infty}^{t} \mu^*(\mathbf{x}, t-\tau)\frac{\partial}{\partial \tau}\epsilon\, d\tau,$$

while $\sigma = \lambda \nabla \cdot \mathbf{U}\ \mathrm{I}_{3\times 3} + 2\mu\epsilon$ for the purely elastic case. Then from the equation of motion $\nabla \cdot \sigma = \rho \mathbf{U}_{tt}$, where $\rho > 0$ is the density, we get

$$\nabla\left[\int_{-\infty}^{t} \lambda^*(\mathbf{x}, t-\tau)\frac{\partial}{\partial \tau}\left(\nabla \cdot \mathbf{U}\right)\, d\tau\right] + \nabla \cdot \int_{-\infty}^{t} \mu^*(\mathbf{x}, t-\tau)\frac{\partial}{\partial \tau}(\nabla \mathbf{U} + \nabla \mathbf{U}^T)\, d\tau = \rho \mathbf{U}_{tt}.$$

For this thesis, we assume that human tissue is locally homogeneous. In other words, the tissue is homogenous in the inclusion and homogenous in the surrounding healthy tissue. Then for

homogeneous material, λ^* and μ^* do not depend on $\mathbf{x}$ so we can simplify the equation to

$$\int_{-\infty}^{t} \mu^*(t-\tau)\frac{\partial}{\partial\tau}\Delta\mathbf{U} + (\lambda^*(t-\tau)+\mu^*(t-\tau))\,\frac{\partial}{\partial\tau}\nabla\left(\nabla\cdot\mathbf{U}\right)\,d\tau = \rho\mathbf{U}_{tt},$$

since $\nabla\cdot(\nabla\mathbf{U}^T) = \nabla(\nabla\cdot\mathbf{U})$.

When the excitation plate of the MRE machine is vibrating, it creates two kinds of waves. The first wave is a shear wave, which propagates into the body with its oscillation being perpendicular to its propagation. The second kind of wave is a compression wave, which oscillates parallel to the propagation direction. However, in human tissue, the compression wave speed ($\sim 1500\ m/sec$) is much greater than the shear wave speed ($\sim 2\ m/sec$), which implies that the compression wave length is much larger than the shear wave length (in fact, the compression wave length is larger than the width of the human body). The large wavelength implies a small amplitude, and hence, the compression wave is almost negligible compared to the shear wave in MRE data. Hence, neglecting the compression terms, our model is reduced to

$$\int_{-\infty}^{t} \mu^*(t-\tau)\frac{\partial}{\partial\tau}\Delta\mathbf{U}\,d\tau = \rho\mathbf{U}_{tt}.$$

Furthermore, our solution $\mathbf{U} = (\mathbf{U_1}, \mathbf{U_2}, \mathbf{U_3})$ is decoupled, so only look at one component of $\mathbf{U}$, say U_3. Now let $U = U_3$, then our (scalar) wave equation in a viscoelastic medium is

$$\int_{-\infty}^{t} \mu^*(t-\tau)\frac{\partial}{\partial\tau}\Delta U\,d\tau = \rho U_{tt}.$$

We can rewrite the equation as

$$\left[(\mu^*\mathrm{H}) * \left(\frac{\partial}{\partial\tau}\Delta U\right)\right](t) = \int_{-\infty}^{\infty} \mu^*(t-\tau)\mathrm{H}(t-\tau)\frac{\partial}{\partial\tau}\Delta U\,d\tau = \rho U_{tt}$$

where H is the heaviside function. Taking the Fourier transform, we get

$$\mu\Delta u = -\rho\omega^2 u$$

where u is the Fourier transform of U $\left(u := \widehat{U} = \int_{-\infty}^{\infty} Ue^{-i\omega t}\, dt\right)$, $\mu(\omega) := i\omega\widehat{\mu^*\mathrm{H}} = i\omega\int_0^{\infty} \mu^*(t)e^{-i\omega t}\, dt$, and $\omega = 2\pi f$ where $f > 0$ is the excitation frequency of the source wave. Then rearranging we have the Helmholtz equation with complex wavenumber, k

$$\Delta u + k^2 u = 0$$

where $k^2 = \dfrac{\rho\omega^2}{\mu(\omega)}$. In Chapter 4, we present three spring dashpot models which correspond to different $\mu(\omega)$.

A plane wave solution to the Helmholtz equation has the form

$$u_i(\mathbf{x}) := e^{ik\mathbf{d}\cdot\mathbf{x}} = e^{-Im(k)\mathbf{d}\cdot\mathbf{x}}e^{iRe(k)\mathbf{d}\cdot\mathbf{x}}, \tag{2.1}$$

where $\mathbf{d}$ is a propagation direction with $|\mathbf{d}| = 1$. For convenience, let $\mathbf{d} = (1, 0, 0)$, which implies that $\mathbf{d}\cdot\mathbf{x} = x_1$ and

$$u_i(\mathbf{x}) = e^{-Im(k)x_1}e^{iRe(k)x_1}.$$

Since the amplitude of the wave in viscoelastic (lossy) media is decreasing as it propagates, we must have $Im(k) \geq 0$. Furthermore, since it is assumed the wave moves along the x_1 direction, we must have $Re(k) > 0$.

In this thesis, we are interested in the smallest inclusion that can be detected in MRE. So for simplicity, we assume a small homogeneous inclusion is embedded in a homogeneous background medium, i.e. healthy tissue. This tumor acts as a penetrable object, so the wave travels through the tumor. Thus, if we let Ω represent the tumor region and $\partial\Omega$ be the boundary of the tumor, then we require that the Helmholtz equation be satisfied in Ω and in $\bar{\Omega}^c$, and across $\partial\Omega$ the displacement u and the normal stress, $\mu\frac{\partial u}{\partial\nu}$, must be continuous. Finally, it is also required that the scattered wave, $u_s = u - u_i$ satisfies Sommerfield's radiation condition, $\left(\frac{\partial}{\partial|\mathbf{x}|} - ik\right)u_s = o\left(\frac{1}{|\mathbf{x}|}\right)$ as $|\mathbf{x}| \to \infty$, which means the scattered wave is outgoing. Mathematically, when our plane wave, $u_i(\mathbf{x}) = e^{ikx_1}$, is incident, then it is scattered by an inclusion, $\Omega \subset \mathbb{R}^3$, and it is also transmitted through Ω (see

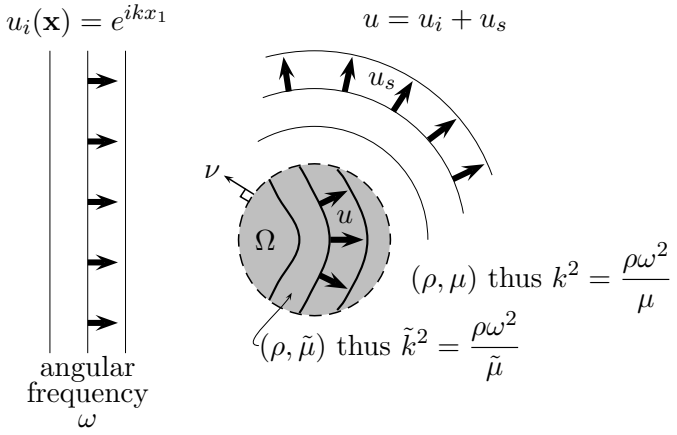

Figure 2.1: As the incident plane wave, u_i, hits the tumor some of the wave are transmitted through and some are scattered, u_s. Also, the outside medium and tumor have different physical properties,i.e. μ versus $\tilde{\mu}$. It is assumed that the density in the tumor is the same as that of healthy tissue.

Figure 2.1). Then the total displacement field u in $\mathbb{R}^3$ satisfies

$$\begin{cases} \Delta u + k^2 u = 0 & \text{in} \quad \bar{\Omega}^c, \\ \Delta u + \tilde{k}^2 u = 0 & \text{in} \quad \Omega, \\ u|_+ = u|_- & \text{on} \quad \partial\Omega, \\ \mu \dfrac{\partial u}{\partial \nu}\Big|_+ = \tilde{\mu} \dfrac{\partial u}{\partial \nu}\Big|_- & \text{on} \quad \partial\Omega, \\ \left(\dfrac{\partial}{\partial |\mathbf{x}|} - ik\right)\left[u - e^{ikx_1}\right] = o\left(\dfrac{1}{|\mathbf{x}|}\right) & \text{as} \quad |\mathbf{x}| \to \infty, \end{cases} \tag{2.2}$$

where $k^2 = \dfrac{\rho\omega^2}{\mu}$ and $\tilde{k}^2 = \dfrac{\rho\omega^2}{\tilde{\mu}}$, and $\mu = \mu(\omega)$ is the the complex shear modulus in $\bar{\Omega}^c$ and $\tilde{\mu} = \tilde{\mu}(\omega)$ is the complex shear modulus in Ω. For the elastography, since the difference in densities is small compared to the differences in the stiffness constant, it is assumed that the density in Ω, is just ρ (in human soft tissue, this density is about the density of water). It is well-known that (2.2) possesses the unique solution in $\mathcal{C}^2(\Omega) \cap \mathcal{C}^2(\bar{\Omega}^c) \cap \mathcal{C}^1(\bar{\Omega}) \cap \mathcal{C}^1(\Omega^c)$ when $Im(k), Im(\tilde{k}) \geq 0$, which is our case. See [4, 13].

Chapter 3

Solution for a Ball Inclusion

In this thesis, we are interested in an estimate for the smallest possible detectable inclusion in MRE with noisy data. Moreover, targeting an early stage cancer detection, we may assume our inclusion is small. To get an explicit estimate, we assume our inclusion is a small ball for which an analytic solution of (2.2) is well-known. Thus we assume $\Omega = B_R(0)$ with $R << 1$ for (2.2).

We start with $k, \tilde{k} \in \mathbb{R}$ (non-attenuating media) and extend the result to $k, \tilde{k} \in \mathbb{C}$ (lossy media). For $k \in \mathbb{R}$ and $k > 0$, using separation of variables we have a spherical Bessel and Hankel solution for the Helmholtz equation $\Delta u + k^2 u = 0$ (see [9]):

$$u_n^m(\mathbf{x}) = j_n(k|\mathbf{x}|)Y_n^m(\hat{\mathbf{x}}), \quad \forall \mathbf{x} \in \mathbb{R}^3, \qquad v_n^m(\mathbf{x}) = h_n^{(1)}(k|\mathbf{x}|)Y_n^m(\hat{\mathbf{x}}), \quad \forall \mathbf{x} \in \mathbb{R}^3 \setminus \{0\},$$

for $\hat{\mathbf{x}} = \frac{\mathbf{x}}{|\mathbf{x}|}$, $\forall n = 0, 1, 2, \ldots$, and $\forall m = -n, \ldots, n$. Furthermore, v_n^m is a radiating solution to the Helmholtz equation, i.e. it satisfies the Sommerfeld radiation condition. Here the radial parts j_n and $h_n^{(1)} = j_n + iy_n$ are the spherical Bessel function and spherical Hankel function of the first kind, respectively, defined as

$$j_n(t) = \sum_{p=0}^{\infty} \frac{(-1)^p t^{n+2p}}{2^p p! 1 \cdot 3 \cdots (2n+2p+1)}, \qquad y_n(t) = -\frac{(2n)!}{2^n n!} \sum_{p=0}^{\infty} \frac{(-1)^p t^{2p-n-1}}{2^p p!(-2n+1)(-2n+3)\cdots(-2n+2p-1)}.$$

Note that j_n is a regular solution and y_n is a singular solution to the spherical Bessel differential

equation

$$t^2 f''(t) + 2tf'(t) + (t^2 - n(n+1))f(t) = 0.$$

The angular part Y_n^m is the spherical harmonic defined as

$$Y_n^m(\theta, \phi) = \sqrt{\frac{2n+1}{4\pi}\frac{(n-|m|)!}{(n+|m|)!}} P_n^{|m|}(\cos\theta) e^{im\phi},$$

which forms a complete orthonormal system in $L^2(\partial B_1(0))$. Here $P_n^{|m|}(t)$ are the associated Legendre functions that satisfy the associated Legendre differential equation

$$(1-t^2)f''(t) - 2tf'(t) + \left(n(n+1) - \frac{m^2}{1-t^2}\right) f(t) = 0.$$

For the interior solution of (2.2) with $\tilde{k} > 0$, using a superposition principle, this transmitted wave has the following series form:

$$u(\mathbf{x}) = \sum_{n=0}^{\infty} \sum_{m=-n}^{n} b_n^m j_n(\tilde{k}|\mathbf{x}|) Y_n^m(\hat{\mathbf{x}}), \quad \forall \mathbf{x} \in \Omega.$$

For the exterior solution of (2.2) with $k > 0$, it is a sum of the incident wave and the (radiating) scattered wave:

$$u(\mathbf{x}) = e^{ik\mathbf{d}\cdot\mathbf{x}} + \sum_{n=0}^{\infty} \sum_{m=-n}^{n} c_n^m h_n^{(1)}(k|\mathbf{x}|) Y_n^m(\hat{\mathbf{x}}), \quad \forall \mathbf{x} \in \bar{\Omega}^c.$$

Note that the plane wave also has a spherical Bessel expansion (Jacobi-Anger expansion)

$$\begin{aligned} e^{ik\mathbf{d}\cdot\mathbf{x}} &= \sum_{n=0}^{\infty} i^n (2n+1) j_n(k|\mathbf{x}|) P_n(\cos\theta), \qquad \cos\theta = \frac{\mathbf{d}\cdot\mathbf{x}}{|\mathbf{x}|} \\ &= \sum_{n=0}^{\infty} i^n \sqrt{4\pi(2n+1)}\, j_n(k|\mathbf{x}|) Y_n^0(\hat{\mathbf{x}}). \end{aligned}$$

Because our source is the plane wave which has only Y_n^0 modes, we expect both the interior and exterior solutions possess also only Y_n^0 modes, i.e., $b_n^m = c_n^m = 0$ for $m \neq 0$, which is proved mathematically in the following theorem.

Theorem 3.1 *If $\Omega = B_R(0)$, the unique solution $u \in \mathcal{C}^2(\Omega) \cap \mathcal{C}^2(\bar{\Omega}^c) \cap \mathcal{C}^1(\bar{\Omega}) \cap \mathcal{C}^1(\Omega^c)$ to (2.2) for real $k, \tilde{k} > 0$ has the following series form:*

$$u(\mathbf{x}) = \begin{cases} \displaystyle\sum_{n=0}^{\infty} b_n j_n(\tilde{k}|\mathbf{x}|) P_n(\cos\theta) & \text{in} \quad \Omega, \\ e^{ik\mathbf{d}\cdot\mathbf{x}} + \displaystyle\sum_{n=0}^{\infty} c_n h_n^{(1)}(k|\mathbf{x}|) P_n(\cos\theta) & \text{in} \quad \bar{\Omega}^c, \end{cases} \tag{3.1}$$

where $\mathbf{d} = (1, 0, 0)$ in (2.2).

Proof. From the previous discussion, we know that the solution to the Helmholtz equation and the radiation condition is given by

$$u(\mathbf{x}) = \begin{cases} \displaystyle\sum_{n=0}^{\infty} \sum_{m=-n}^{n} b_n^m j_n(\tilde{k}|\mathbf{x}|) Y_n^m(\hat{\mathbf{x}}) & \text{in} \quad \Omega, \\ e^{ik\mathbf{d}\cdot\mathbf{x}} + \displaystyle\sum_{n=0}^{\infty} \sum_{m=-n}^{n} c_n^m h_n^{(1)}(k|\mathbf{x}|) Y_n^m(\hat{\mathbf{x}}) & \text{in} \quad \bar{\Omega}^c. \end{cases}$$

From the two boundary conditions, $u|_+ = u|_-$ and $\mu \frac{\partial u}{\partial \nu}\big|_+ = \tilde{\mu} \frac{\partial u}{\partial \nu}\big|_-$ on $\partial\Omega = \partial B_R(0)$, we get

$$\begin{aligned} \sum_{n=0}^{\infty} \sum_{m=-n}^{n} b_n^m j_n(\tilde{k}R) Y_n^m(\hat{\mathbf{x}}) &= \sum_{n=0}^{\infty} i^n \sqrt{4\pi(2n+1)} j_n(kR) Y_n^0(\hat{\mathbf{x}}) + \sum_{n=0}^{\infty} \sum_{m=-n}^{n} c_n^m h_n^{(1)}(kR) Y_n^m(\hat{\mathbf{x}}) \\ &= \sum_{n=0}^{\infty} \sum_{m=-n}^{n} \left[c_n^m h_n^{(1)}(kR) + d_n^m \right] Y_n^m(\hat{\mathbf{x}}), \\ \tilde{\mu}\tilde{k} \sum_{n=0}^{\infty} \sum_{m=-n}^{n} b_n^m j_n'(\tilde{k}R) Y_n^m(\hat{\mathbf{x}}) &= \mu k \sum_{n=0}^{\infty} i^n \sqrt{4\pi(2n+1)} j_n'(kR) Y_n^0(\hat{\mathbf{x}}) + \mu k \sum_{n=0}^{\infty} \sum_{m=-n}^{n} c_n^m (h_n^{(1)})'(kR) Y_n^m(\hat{\mathbf{x}}) \\ &= \mu k \sum_{n=0}^{\infty} \sum_{m=-n}^{n} \left[c_n^m (h_n^{(1)})'(kR) + D_n^m \right] Y_n^m(\hat{\mathbf{x}}), \end{aligned}$$

where $d_n^m = \begin{cases} i^n \sqrt{4\pi(2n+1)} j_n(kR) & \text{if } m = 0, \\ 0 & \text{if } m \neq 0, \end{cases}$ and $D_n^m = \begin{cases} i^n \sqrt{4\pi(2n+1)} j_n'(kR) & \text{if } m = 0, \\ 0 & \text{if } m \neq 0. \end{cases}$

Recalling that Y_n^m forms an orthonormal system, we obtain

$$b_n^m j_n(\tilde{k}R) = c_n^m h_n^{(1)}(kR) + d_n^m, \quad \frac{\tilde{\mu}\tilde{k}}{\mu k} b_n^m j_n'(\tilde{k}R) = c_n^m (h_n^{(1)})'(kR) + D_n^m \qquad \forall n, m.$$

Hence for each n and m, we have the following matrix equation:

$$\begin{pmatrix} j_n(\tilde{k}R) & -h_n^{(1)}(kR) \\ \frac{k}{\tilde{k}} j_n'(\tilde{k}R) & -(h_n^{(1)})'(kR) \end{pmatrix} \begin{pmatrix} b_n^m \\ c_n^m \end{pmatrix} = \begin{pmatrix} d_n^m \\ D_n^m \end{pmatrix}$$

where we use $\frac{\tilde{\mu}\tilde{k}}{\mu k} = \frac{\frac{\rho\omega^2}{\tilde{k}^2}}{\frac{\rho\omega^2}{k^2}} \frac{\tilde{k}}{k} = \frac{k}{\tilde{k}}$. In particular, if $m \neq 0$ we have

$$\begin{pmatrix} j_n(\tilde{k}R) & -h_n^{(1)}(kR) \\ \frac{k}{\tilde{k}} j_n'(\tilde{k}R) & -(h_n^{(1)})'(kR) \end{pmatrix} \begin{pmatrix} b_n^m \\ c_n^m \end{pmatrix} = \begin{pmatrix} 0 \\ 0 \end{pmatrix}.$$

We could show the matrix is nonsingular, and thus it has only a trivial solution, but this requires a complicated interrelation of the roots of special functions. So we give an indirect proof here. If the matrix is singular, then we have infinitely many possible b_n^m and c_n^m, so our solution u is not unique, which violates the uniqueness of (2.2). Hence the matrix must be nonsingular, thus $b_n^m = c_n^m = 0$ for $m \neq 0$.

As a result, the solution to (2.2) for real $k, \tilde{k} > 0$ is of the following form

$$u(\mathbf{x}) = \begin{cases} \displaystyle\sum_{n=0}^{\infty} b_n j_n(\tilde{k}|\mathbf{x}|) P_n(\cos\theta) & \text{in} \quad \Omega, \\ e^{ik\mathbf{x}\cdot d} + \displaystyle\sum_{n=0}^{\infty} c_n h_n^{(1)}(k|\mathbf{x}|) P_n(\cos\theta) & \text{in} \quad \bar{\Omega}^c, \end{cases}$$

since $Y_n^0(\hat{\mathbf{x}}) = \sqrt{\frac{2n+1}{4\pi}} P_n(\cos\theta)$. □

However in our viscoelastic medium problem, complex k and $\tilde{k}$ have been introduced, so we have to extend (3.1) to the complex case. First note that the spherical Bessel functions for $z \in \mathbb{C}$

have exactly the same series representation as real case:

$$j_n(z) = \sum_{p=0}^{\infty} \frac{(-1)^p z^{n+2p}}{2^p p! 1 \cdot 3 \cdots (2n+2p+1)},$$
$$y_n(z) = -\frac{(2n)!}{2^n n!} \sum_{p=0}^{\infty} \frac{(-1)^p z^{2p-n-1}}{2^p p! (-2n+1)(-2n+3) \cdots (-2n+2p-1)},$$

and they are solutions to the spherical Bessel differential equation with complex variable

$$z^2 f''(z) + 2z f'(z) + (z^2 - n(n+1)) f(z) = 0. \tag{3.2}$$

The spherical Hankel function of first kind is also defined as

$$h_n^{(1)}(z) = j_n(z) + i y_n(z).$$

Theorem 3.2 *The Jacobi-Anger expansion is also valid for $k \in \mathbb{C}$, i.e.,*

$$e^{ik\mathbf{d}\cdot\mathbf{x}} = \sum_{n=0}^{\infty} i^n (2n+1) j_n(k|\mathbf{x}|) P_n(\cos\theta), \qquad \cos\theta = \frac{\mathbf{d}\cdot\mathbf{x}}{|\mathbf{x}|}.$$

Proof. See p. 368 in [27]. □

Theorem 3.3 (*Interior Solution*) *If $\Omega = B_R(0)$, the function*

$$u = \sum_{n=0}^{\infty} b_n j_n(\tilde{k}|\mathbf{x}|) P_n(\cos\theta) \quad \textit{is a solution of} \quad \Delta u + \tilde{k}^2 u = 0 \quad \textit{in } \Omega, \quad \forall \tilde{k} \in \mathbb{C}.$$

Proof. Let $v(\mathbf{x}) = j_n(\tilde{k}r) Y_n^0(\theta, \phi)$ where $r = |\mathbf{x}|$. Since $Y_n^0(\theta, \phi)$ is independent of ϕ, we have

$$\Delta v = \frac{1}{r^2} \frac{\partial}{\partial r} \left(r^2 \frac{\partial}{\partial r} j_n(\tilde{k}r) \right) Y_n^0(\theta, \phi) + \frac{1}{r^2 \sin\theta} \frac{\partial}{\partial \theta} \left(\sin\theta \frac{\partial}{\partial \theta} Y_n^0(\theta, \phi) \right) j_n(\tilde{k}r).$$

Recalling that $\frac{1}{\sin\theta}\frac{\partial}{\partial\theta}\left(\sin\theta\frac{\partial}{\partial\theta}Y_n^0(\theta,\phi)\right) = -n(n+1)Y_n^0(\theta,\phi)$ (see [9]), we get

$$\begin{aligned}\Delta v &= Y_n^0(\theta,\phi)\left[\frac{1}{r^2}\frac{\partial}{\partial r}\left(r^2\frac{\partial}{\partial r}[j_n(\tilde{k}r)]\right) - \frac{n(n+1)}{r^2}j_n(\tilde{k}r)\right] = \frac{1}{r^2}Y_n^0(\theta,\phi)\left[\frac{\partial}{\partial r}\left(r^2\frac{\partial}{\partial r}[j_n(\tilde{k}r)]\right) - n(n+1)j_n(\tilde{k}r)\right] \\ &= \frac{1}{r^2}Y_n^0(\theta,\phi)\left[\frac{\partial}{\partial r}\left(\tilde{k}r^2 j_n'(\tilde{k}r)\right) - n(n+1)j_n(\tilde{k}r)\right] = \frac{1}{r^2}Y_n^0(\theta,\phi)\left[(\tilde{k}r)^2 j_n''(\tilde{k}r) + 2(\tilde{k}r)j_n'(\tilde{k}r) - n(n+1)j_n(\tilde{k}r)\right] \\ &= \frac{1}{r^2}Y_n^0(\theta,\phi)\left[-(\tilde{k}r)^2 j_n(\tilde{k}r)\right] = -\tilde{k}^2 v \quad \text{(we use the fact that } j_n(z) \text{ is a solution of (3.2))}.\end{aligned}$$

From the definition of Y_n^0, $w(\mathbf{x}) = j_n(\tilde{k}r)P_n(\cos\theta) = \sqrt{\frac{4\pi}{2n+1}}j_n(\tilde{k}r)Y_n^0(\theta,\phi)$ also satisfies $\Delta w + \tilde{k}^2 w = 0$. By the superposition principle, $u = \sum_{n=0}^{\infty} b_n j_n(\tilde{k}|\mathbf{x}|)P_n(\cos\theta)$ is a solution of $\Delta u + \tilde{k}^2 u = 0$.
□

Theorem 3.4 (*Radiating Solution*) *If $\Omega = B_R(0)$, the function*

$$u = \sum_{n=0}^{\infty} c_n h_n^{(1)}(k|\mathbf{x}|)P_n(\cos\theta) \quad \textit{is a radiating solution of} \quad \Delta u + k^2 u = 0 \quad \textit{in } \bar{\Omega}^c, \quad \forall k \in \mathbb{C} \textit{ with } Im(k) \geq 0.$$

Proof. First note that (see [1])

$$h_n^{(1)}(z) = i^{-n-1}z^{-1}e^{iz}\sum_{j=0}^{n}\binom{n+\frac{1}{2}}{j}(-2iz)^{-j}.$$

Since $e^{ikr} = e^{ik_R r - k_I r} = e^{-k_I r}e^{ik_R r}$ with $k_I = Im(k) \geq 0$, we have $\left|e^{ikr}\right| = e^{-k_I r} \leq 1$ for $r \geq 0$. As a result,

$$h_n^{(1)}(kr) = \frac{1}{i^{n+1}}\frac{1}{kr}e^{ikr} + O\left(\frac{1}{r^2}\right).$$

Then we get

$$\frac{\partial h_n^{(1)}(kr)}{\partial r} - ikh_n^{(1)}(kr) = \left(\frac{1}{i^n}\frac{1}{r}e^{ikr} + O\left(\frac{1}{r^2}\right)\right) - \left(\frac{1}{i^n}\frac{1}{r}e^{ikr} + O\left(\frac{1}{r^2}\right)\right) = O\left(\frac{1}{r^2}\right).$$

Hence it is clear that $u(\mathbf{x}) = \sum_{n=0}^{\infty} c_n h_n^{(1)}(k|\mathbf{x}|)P_n(\cos\theta)$ satisfies the Sommerfeld radiation condition. A similar argument used in Theorem 3.3 shows that it also satisfies $\Delta u + k^2 u = 0$, except at the origin. □

Corollary 3.5 (*Exterior Solution*) *If* $\Omega = B_R(0)$, *the function*

$$u = e^{ik\mathbf{d}\cdot\mathbf{x}} + \sum_{n=0}^{\infty} c_n h_n^{(1)}(k|\mathbf{x}|)P_n(\cos\theta) \quad \textit{is a solution of} \quad \Delta u + k^2 u = 0 \quad \textit{in } \bar{\Omega}^c, \quad \forall k \in \mathbb{C} \textit{ with } Im(k) \geq 0.$$

Proof. From (3.4) and utilizing $e^{ik\mathbf{d}\cdot\mathbf{x}}$ is a solution to the Helmholtz equation $\forall \mathbf{x} \in \mathbb{R}^3$, we get the desired result. □

As a result, we see that (3.1) is valid for $\forall k, \tilde{k} \in \mathbb{C}$ satisfying $Im(k) \geq 0$. Now we determine the coefficients b_n and c_n in (3.1). As in the proof of Theorem 3.1, using two matching boundary conditions we establish a matrix equation:

$$\begin{pmatrix} j_n(\tilde{k}R) & -h_n(kR) \\ \frac{k}{\tilde{k}} j_n'(\tilde{k}R) & -h_n'(kR) \end{pmatrix} \begin{pmatrix} b_n \\ c_n \end{pmatrix} = \begin{pmatrix} i^n(2n+1)j_n(kR) \\ i^n(2n+1)j_n'(kR) \end{pmatrix},$$

where we denote $h_n^{(1)}$ by h_n for convenience. From Cramer's rule, we get

$$\begin{aligned} b_n &= \frac{i^n(2n+1)(j_n'(kR)h_n(kR) - j_n(kR)h_n'(kR))}{\frac{k}{\tilde{k}} j_n'(\tilde{k}R)h_n(kR) - j_n(\tilde{k}R)h_n'(kR)} \\ &= \frac{i^n(2n+1)(j_n'(kR)j_n(kR) + ij_n'(kR)y_n(kR) - j_n(kR)j_n'(kR) - ij_n(kR)y_n'(kR))}{\frac{k}{\tilde{k}} j_n'(\tilde{k}R)h_n(kR) - j_n(\tilde{k}R)h_n'(kR)} \\ &= \frac{i^{n+1}(2n+1)(j_n'(kR)y_n(kR) - j_n(kR)y_n'(kR))}{\frac{k}{\tilde{k}} j_n'(\tilde{k}R)h_n(kR) - j_n(\tilde{k}R)h_n'(kR)}. \end{aligned}$$

Then by using the Wronskian and properties of Bessel functions [9],

$$j_n(t)y_n'(t) - j_n'(t)y_n(t) = \begin{vmatrix} j_n(t) & y_n(t) \\ j_n'(t) & y_n'(t) \end{vmatrix} = \frac{1}{t^2},$$

we obtain

$$b_n = \frac{-i^n(2n+1)}{j_n(\tilde{k}R)h_n'(kR) - \frac{k}{\tilde{k}}j_n'(\tilde{k}R)h_n(kR)} \left[\frac{1}{ik^2R^2}\right]. \tag{3.3}$$

Similarly, using Cramer's rule again, we obtain

$$c_n = \frac{-i^n(2n+1)}{j_n(\tilde{k}R)h_n'(kR) - \frac{k}{\tilde{k}}j_n'(\tilde{k}R)h_n(kR)} \left[j_n(\tilde{k}R)j_n'(kR) - \frac{k}{\tilde{k}}j_n'(\tilde{k}R)j_n(kR)\right]. \tag{3.4}$$

In summary, we proved the following theorem.

Theorem 3.6 *Let $\Omega = B_R(0)$ and $k, \tilde{k} \in \mathbb{C}$ satisfying $Im(k) \geq 0$. Then the unique solution of (2.2) where $\mathbf{d} = (1,0,0)$ is*

$$u(\mathbf{x}) = \begin{cases} \displaystyle\sum_{n=0}^{\infty} b_n j_n(\tilde{k}|\mathbf{x}|)P_n(\cos\theta) & \text{in} \quad \Omega = B_R(0), \\ e^{ik\mathbf{d}\cdot\mathbf{x}} + \displaystyle\sum_{n=0}^{\infty} c_n h_n^{(1)}(k|\mathbf{x}|)P_n(\cos\theta) & \text{in} \quad \bar{\Omega}^c, \end{cases}$$

$$\text{where} \quad \begin{cases} b_n = \dfrac{-i^n(2n+1)}{j_n(\tilde{k}R)h_n'(kR) - \frac{k}{\tilde{k}}j_n'(\tilde{k}R)h_n(kR)} \left[\dfrac{1}{ik^2R^2}\right], \\ c_n = \dfrac{-i^n(2n+1)}{j_n(\tilde{k}R)h_n'(kR) - \frac{k}{\tilde{k}}j_n'(\tilde{k}R)h_n(kR)} \left[j_n(\tilde{k}R)j_n'(kR) - \dfrac{k}{\tilde{k}}j_n'(\tilde{k}R)j_n(kR)\right]. \end{cases}$$

□

Chapter 4

Detectability

4.1 Definition and approximation of detectability

As the wave hits the tumor, a visual change is observed in the measured displacement data, so a quantitative analysis of this change would like to be calculated. In the purely elastic case, because the stiffness of the tumor is greater than the stiffness of the surrounding medium, the wave speed, c, is greater in the tumor, which implies that the wave is more spread in the tumor region. By the conservation of energy, this implies that the amplitude of the wave in the tumor must decrease. For a small inclusion, we expect similar results for the viscoelastic case. This change of amplitude in the tumor will be used to quantify the detectability of the tumor. Furthermore, for a small inclusion the amplitude at the center point is a good representative of this amplitude drop because we know the solution is continuous. The evaluation of the wave at the center point becomes much easier, since only the zeroth term survives in the series expansion given in Theorem 3.6.

Our *detectability* of the tumor via its relative amplitude drop will be defined as

$$Det = \frac{|u_i(0)| - |u(0)|}{|u_i(-L)|}$$

where $u(x)$ represents our solution with the tumor, $u_i(x) = u_i(x_1) = e^{ikx_1}$ is the incident plane wave without the inclusion of the tumor, and $|u_i(-L)|$ is the amplitude of the incident wave at the

source, $x_1 = -L$. Simplifying, we have

$$Det = \frac{1 - |u(0)|}{e^{L \cdot Im(k)}} = e^{-L \cdot Im(k)}(1 - |u(0)|), \tag{4.1}$$

which is bound by 1 since $Im(k) \geq 0$. From Theorem 3.6, the total field in the inclusion is

$$u(\mathbf{x}) = \sum_{n=0}^{\infty} \frac{-i^n(2n+1)}{j_n(\tilde{k}R)h_n'(kR) - \frac{k}{\tilde{k}} j_n'(\tilde{k}R)h_n(kR)} \frac{j_n(\tilde{k}r)P_n(\cos\theta)}{ik^2R^2}, \qquad |\mathbf{x}| = r < R. \tag{4.2}$$

Since $j_0(0) = 1$, $j_n(0) = 0$ for $n \geq 1$, $j_0'(x) = -j_1(x)$, $h_0'(x) = -h_1(x)$, and $P_0(t) = 1$, we get

$$u(0) = \frac{-1}{j_0(\tilde{k}R)h_0'(kR) - \frac{k}{\tilde{k}} j_0'(\tilde{k}R)h_0(kR)} \frac{1}{ik^2R^2} = \frac{-1}{ik^2R^2\left[\frac{k}{\tilde{k}} j_1(\tilde{k}R)h_0(kR) - j_0(\tilde{k}R)h_1(kR)\right]}.$$

Also note by definition and properties of Bessel functions,

$$ik^2R^2\left[\frac{k}{\tilde{k}} j_1(\tilde{k}R)h_0(kR) - j_0(\tilde{k}R)h_1(kR)\right] = ik^2R^2\left[\frac{k}{\tilde{k}} \frac{\sin\tilde{k}R - \tilde{k}R\cos\tilde{k}R}{\tilde{k}^2R^2} \frac{e^{ikR}}{ikR} + \frac{\sin\tilde{k}R}{\tilde{k}R} \frac{e^{ikR}}{kR}\left(1 + \frac{i}{kR}\right)\right]$$

$$= ik^2R^2\left[-i\frac{\sin\tilde{k}R - \tilde{k}R\cos\tilde{k}R}{\tilde{k}^3R^3} + \frac{\sin\tilde{k}R}{\tilde{k}k^2R^3}(kR + i)\right]e^{ikR} = \left[\frac{\sin\tilde{k}R - \tilde{k}R\cos\tilde{k}R}{(\tilde{k}/k)^2} + i\sin\tilde{k}R\,(kR + i)\right]\frac{e^{ikR}}{\tilde{k}R}$$

$$= \left[\frac{k^2}{\tilde{k}^2}\left(\frac{\sin\tilde{k}R}{\tilde{k}R} - \cos\tilde{k}R\right) - \frac{\sin\tilde{k}R}{\tilde{k}R} + i\frac{k}{\tilde{k}}\sin\tilde{k}R\right]e^{ikR} = \left[\left(\frac{k^2}{\tilde{k}^2} - 1\right)\frac{\sin\tilde{k}R}{\tilde{k}R} - \frac{k}{\tilde{k}}\left(\frac{k}{\tilde{k}}\cos\tilde{k}R - i\sin\tilde{k}R\right)\right]e^{ikR}.$$

Hence,

$$u(0) = \frac{e^{-ikR}}{\left(1 - \frac{k^2}{\tilde{k}^2}\right)\frac{\sin\tilde{k}R}{\tilde{k}R} + \frac{k}{\tilde{k}}\left(\frac{k}{\tilde{k}}\cos\tilde{k}R - i\sin\tilde{k}R\right)} \tag{4.3}$$

Since small tumors are of interest, the Taylor series expansion for small R is used to get

$$\begin{aligned}
u(0) &= \frac{1 - ikR - \frac{(kR)^2}{2} + i\frac{(kR)^3}{6} + O(R^4)}{\left(1 - \frac{k^2}{\tilde{k}^2}\right)\frac{\tilde{k}R - \frac{(\tilde{k}R)^3}{6} + O(R^5)}{\tilde{k}R} + \frac{k}{\tilde{k}}\left(\frac{k}{\tilde{k}}[1 - \frac{(\tilde{k}R)^2}{2}] - i[\tilde{k}R - \frac{(\tilde{k}R)^3}{6}] + O(R^4)\right)} \\
&= \frac{1 - ikR - \frac{(kR)^2}{2} + i\frac{(kR)^3}{6} + O(R^4)}{\left(1 - \frac{k^2}{\tilde{k}^2}\right)(1 - \frac{(\tilde{k}R)^2}{6}) + \frac{k}{\tilde{k}}\left(\frac{k}{\tilde{k}}[1 - \frac{(\tilde{k}R)^2}{2}] - i[\tilde{k}R - \frac{(\tilde{k}R)^3}{6}]\right) + O(R^4)} \\
&= \frac{1 - ikR - \frac{(kR)^2}{2} + i\frac{(kR)^3}{6} + O(R^4)}{1 - ikR - \frac{1}{6}\left(\tilde{k}^2 + 2k^2\right)R^2 + i\frac{k\tilde{k}^2}{6}R^3 + O(R^4)} \\
&= \left(1 - ikR - \frac{(kR)^2}{2} + i\frac{(kR)^3}{6} + O(R^4)\right)\left(1 + ikR + \frac{1}{6}(\tilde{k}^2 - 4k^2)R^2 + \frac{ik}{6}(\tilde{k}^2 - 2k^2)R^3 + O(R^4)\right) \\
&= 1 + \frac{R^2}{6}(\tilde{k}^2 - k^2) + O(R^4).
\end{aligned}$$

Separating the real and imaginary parts of k and $\tilde{k}$, we get

$$u(0) = 1 + \frac{R^2}{6}\Big(Re(\tilde{k})^2 - Im(\tilde{k})^2 - Re(k)^2 + Im(k)^2 + 2i[Re(\tilde{k})Im(\tilde{k}) - Re(k)Im(k)]\Big) + O(R^4).$$

So the amplitude squared becomes

$$\begin{aligned}
|u(0)|^2 &= \left[1 + \frac{R^2}{6}\Big(Re(\tilde{k})^2 - Im(\tilde{k})^2 - Re(k)^2 + Im(k)^2\Big)\right]^2 + \left[\frac{R^2}{3}\Big(Re(\tilde{k})Im(\tilde{k}) - Re(k)Im(k)\Big)\right]^2 + O(R^4) \\
&= 1 + \frac{R^2}{3}\Big(Re(\tilde{k})^2 - Im(\tilde{k})^2 - Re(k)^2 + Im(k)^2\Big) + O(R^4).
\end{aligned}$$

Since we assume $R << 1$, using the Taylor series again, $\sqrt{1+z} = 1 + \frac{1}{2}z + O(z^2)$ for $|z| < 1$, $z \in \mathbb{C}$, we get

$$|u(0)| = 1 + \frac{R^2}{6}\Big(Re(\tilde{k})^2 - Im(\tilde{k})^2 - Re(k)^2 + Im(k)^2\Big) + O(R^4).$$

Thus our detectability defined in (4.1) becomes

$$\begin{aligned} Det &= e^{-L\cdot Im(k)}\left[1-\left(1+\frac{R^2}{6}(Re(\tilde{k})^2-Im(\tilde{k})^2-Re(k)^2+Im(k)^2)+O(R^4)\right)\right] \\ &= -e^{-L\cdot Im(k)}\frac{R^2}{6}\Big(Re(\tilde{k})^2-Im(\tilde{k})^2-Re(k)^2+Im(k)^2\Big)+O(R^4) \\ &= -e^{-L\cdot Im(k)}\frac{R^2}{6}Re(\tilde{k}^2-k^2)+O(R^4)=e^{-L\cdot Im(k)}\frac{R^2}{6}Re(k^2-\tilde{k}^2)+O(R^4). \end{aligned}$$

We define estimated detectability as

$$Det_{est}(L,R,k,\tilde{k}) := e^{-L\cdot Im(k)}\frac{R^2}{6}Re(k^2-\tilde{k}^2). \tag{4.4}$$

4.2 Detectability as a function of wave speed and attenuation

By Equation (4.1), we expect the greatest detectability when $|u(0)|$ is the smallest. The two factors that we are most interested in that control $|u(0)|$ are wave speed ($c = \omega/Re(k)$) and attenuation ($\gamma = Im(k)$). In the purely elastic case, if the wave speed in the inclusion is greater than in the background ($\tilde{c} > c$), then the faster wave will cause a drop in amplitude at the center of the inclusion. Furthermore, if the wave speed is homogeneous, but the attenuation is larger in the inclusion ($\tilde{\gamma} > \gamma$), then the wave decays more in the inclusion, and there is an amplitude drop at the center. Note that the effect of $\tilde{\gamma}$ is small for small radius, because the wave does not have enough distance to decay. As a result, in Figure 4.1, for $R = 1.0\ mm$, Det is nearly constant with respect to $\tilde{\gamma}$. Overall, as $\tilde{c}$ or $\tilde{\gamma}$ increases, then Det increases, but it is bounded above.

If $\tilde{c} > c$ and $\tilde{\gamma} > \gamma$, then Det is expected to be positive and to increase as R increases, which is confirmed in Figure 4.1. However, in general it is possible to get negative detectability. For example, if $\tilde{c} > c$ and $\tilde{\gamma} < \gamma$ and the inclusion is small, then the effect of $\tilde{c}$ dominates and $Det > 0$, but as the inclusion size increases, the effect of $\tilde{\gamma}$ increases and Det will become negative. In particular from Equation (4.4), $Det_{est} < 0$ if and only if

$$Re(k^2 - \tilde{k}^2) < 0 \Leftrightarrow \omega^2 \left(\frac{1}{c^2} - \frac{1}{\tilde{c}^2} \right) < \gamma^2 - \tilde{\gamma}^2,$$

the region of which is separated by the dashed lines in Figure 4.1. Since $Det \approx Det_{est}$ for small R, we expect that this inequality will hold approximately for Det with small inclusions (compare the rows in Figure 4.1 for $R = 1, 3, 5\ mm$). In Figure 4.1, it appears that if $Det_{est} < 0$, then $Det < 0$, but the reverse may not be true. If $\tilde{c} \leq c$ and $\tilde{\gamma} < \gamma$, then the inequality is trivially satisfied and both Det and Det_{est} are negative. However this case ($\tilde{c} < c$) is unrealistic, so it is not pictured in the figure and not discussed, but mathematically the results follow similarly.

In Sections 4.4-4.6, we will discuss the cases when the model of the inclusion becomes rigid. When this occurs, wave speed approaches infinity, and attenuation becomes zero in the inclusion.

Lemma 4.1 *For fixed ω, $c \to \infty$ and the $\gamma \to 0$ if and only if $k \to 0$. Furthermore,* $\lim_{\tilde{k} \to 0} Det =$

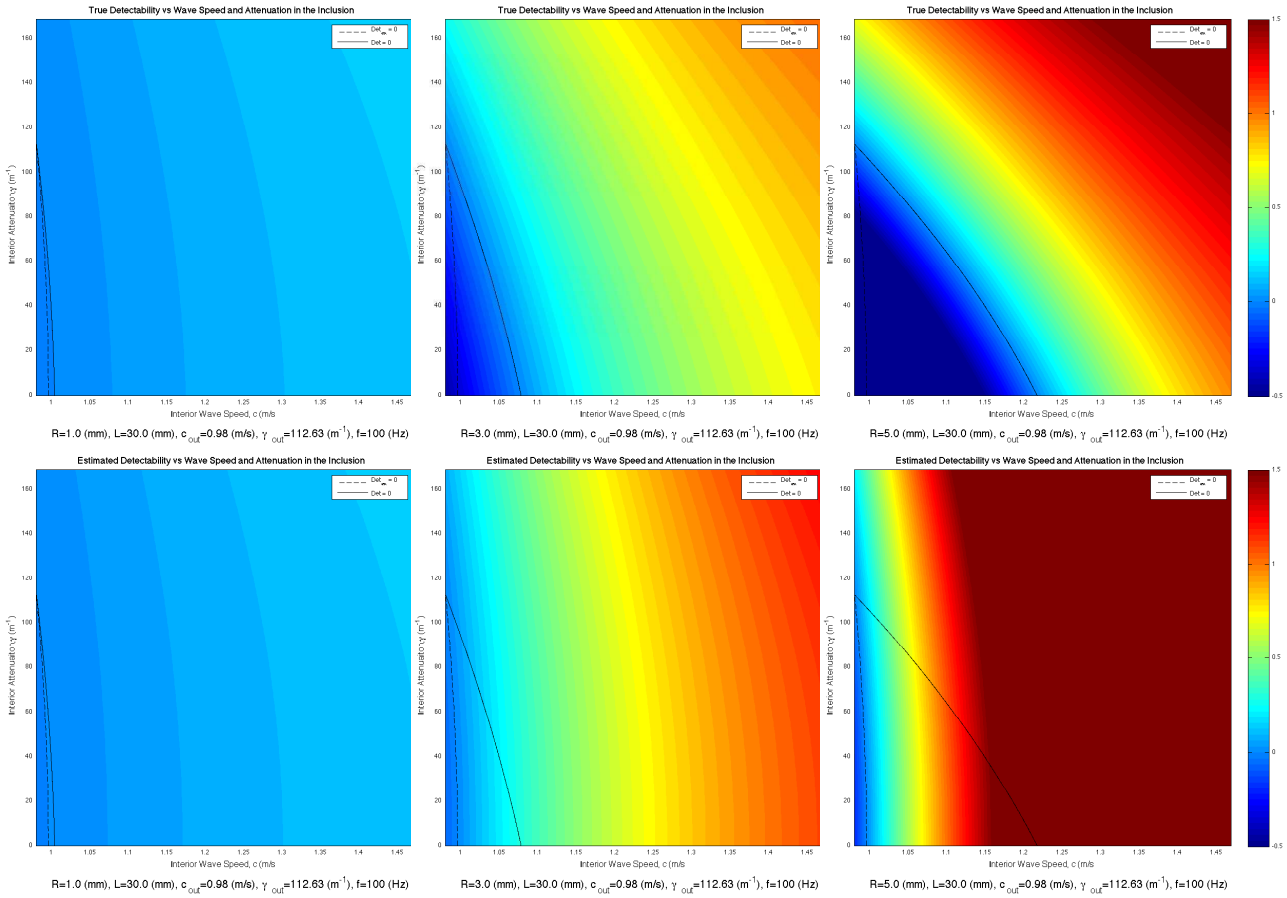

Figure 4.1: Detectability versus wave speed and attenuation in the inclusion. The rows represent true detectability and estimated detectability, and the columns represent radius size: 1.0 mm, 3.0 mm, and 5.0 mm. The solid and dashed lines mark where Det and Det_{est} equal zero, respectively. Realistic values for breast tissue [26] are used. We plot only for $\tilde{c} \geq c = 0.98\ m/s$.

$$e^{-L \cdot Im(k)} \left(1 - \frac{3e^{Im(k)R}}{|3 - k^2R^2 - 3ikR|}\right) \ when\ \Omega = B_R(0).$$

Proof. Recall that $c = \omega/Re(k)$ and $\gamma = Im(k)$. From this, it is clear that for fixed ω,

$$c \to \infty \text{ and } \gamma \to 0 \Leftrightarrow k \to 0.$$

Now note that for small $\tilde{k}$, using Taylor series and (4.3), we have

$$u(0) = \frac{e^{-ikR}}{1 - \frac{k^2R^2}{3} - ikR + O\left(\tilde{k}^2\right)}.$$

Then,

$$\lim_{\tilde{k}\to 0} u(0) = \frac{e^{-ikR}}{1 - \frac{k^2R^2}{3} - ikR}$$

and since the absolute value function is continuous for complex variables,

$$\lim_{\tilde{k}\to 0} |u(0)| = \frac{3e^{Im(k)R}}{|3 - k^2R^2 - 3ikR|}$$

Thus,

$$\lim_{\tilde{k}\to 0} Det = e^{-L\cdot Im(k)} \left(1 - \frac{3e^{Im(k)R}}{|3 - k^2R^2 - 3ikR|}\right).$$

□

Remark 4.2 *Note that Lemma 4.2 is a generalization of the purely elastic case where* $Im(k) = 0$ *[19]:*

$$\lim_{\tilde{k}\to 0} Det = 1 - \left(\frac{(kR)^4}{9} + \frac{(kR)^2}{3} + 1\right)^{-1/2}.$$

4.3 Spring-dashpot models

Using specific spring-dashpot models, we can further analyze detectabilty, but these models are usually defined in terms of μ. Thus, we need to rewrite k in terms of μ. First, note that $k^2 = \frac{\rho\omega^2}{\mu} = \frac{\rho\omega^2\bar{\mu}}{|\mu|^2} = \frac{\rho\omega^2}{|\mu|^2}\left(Re(\mu) - iIm(\mu)\right) = \frac{\rho\omega^2}{|\mu|}e^{i\theta}$ where $\theta = arg(k^2) = -arg(\mu) = \tan^{-1}\left(-\frac{Im(\mu)}{Re(\mu)}\right)$. Note that this implies $\cos(\theta) = \frac{Re(\mu)}{|\mu|}$ and $\sin(\theta) = -\frac{Im(\mu)}{|\mu|}$.

Then we have $k = \sqrt{\frac{\rho\omega^2}{|\mu|}e^{i\tilde{\theta}}} = \sqrt{\frac{\rho\omega^2}{|\mu|}}\left(\cos\tilde{\theta} + i\sin\tilde{\theta}\right)$, where $\tilde{\theta} = \frac{1}{2}\tan^{-1}\left(-\frac{Im(\mu)}{Re(\mu)}\right) = \frac{1}{2}\theta$. Then $\cos\tilde{\theta} = \cos\left(\frac{\theta}{2}\right) = \sqrt{\frac{1}{2}(1+\cos\theta)} = \sqrt{\frac{1}{2}\left(1 + \frac{Re(\mu)}{|\mu|}\right)}$ and $\sin\tilde{\theta} = \sin\left(\frac{\theta}{2}\right) = \sqrt{\frac{1}{2}(1-\cos\theta)} = \sqrt{\frac{1}{2}\left(1 - \frac{Re(\mu)}{|\mu|}\right)}$. Note that the positive square roots are chosen because we require that our waves moves from left to right implying $Re(k) > 0$, and that the wave decays implying $Im(k) \geq 0$. This further implies that $\tilde{\theta} \in \left[0, \frac{\pi}{2}\right)$. Thus,

$$Re(k) = \sqrt{\frac{\rho\omega^2}{2|\mu|}\left(1 + \frac{Re(\mu)}{|\mu|}\right)} \quad \text{and} \quad Im(k) = \sqrt{\frac{\rho\omega^2}{2|\mu|}\left(1 - \frac{Re(\mu)}{|\mu|}\right)},$$

which leads to $Im(\mu) \leq 0$.

In this thesis, we consider only the following three popular rheological models that consist of a few stiffness constants $m_i > 0$ and one viscosity constant $\eta > 0$.

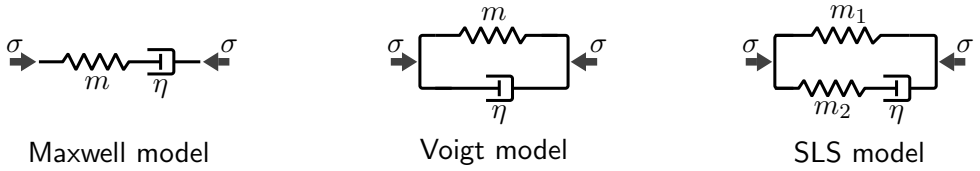

Figure 4.2: Spring and dashpot configurations for Maxwell, Voigt, and SLS models

	μ	$Re(\mu)$	$Im(\mu)$	$\lvert\mu\rvert$
Maxwell	$\left[\frac{1}{m}-\frac{1}{i\omega\eta}\right]^{-1}$	$\frac{m\omega^2\eta^2}{m^2+\omega^2\eta^2}$	$-\frac{m^2\omega\eta}{m^2+\omega^2\eta^2}$	$\frac{m\omega\eta}{\sqrt{m^2+\omega^2\eta^2}}$
Voigt	$m-i\omega\eta$	m	$-\omega\eta$	$\sqrt{m^2+\omega^2\eta^2}$
SLS	$\frac{m_1m_2-i\omega\eta(m_1+m_2)}{m_2-i\omega\eta}$	$\frac{m_1m_2^2+\omega^2\eta^2(m_1+m_2)}{m_2^2+\omega^2\eta^2}$	$-\frac{\omega\eta m_2^2}{m_2^2+\omega^2\eta^2}$	$\sqrt{\frac{m_1^2m_2^2+\omega^2\eta^2(m_1+m_2)^2}{m_2^2+\omega^2\eta^2}}$

Table 4.1: μ for Maxwell, Voigt, and SLS models: The signs for μ are different from other literatures, [10], because our time-harmonic term is not $e^{i\omega t}$, but $e^{-i\omega t}$. Observe that our restriction, $Im(\mu)\leq 0$, is satified. Here all of ρ, ω, m, m_1, m_2, and η are strictly positive.

	$Re(k)$	$Im(k)$	k^2
Maxwell	$\sqrt{\frac{\rho\omega^2}{2\lvert\mu\rvert}\left(1+\frac{\lvert\mu\rvert}{m}\right)}$	$\sqrt{\frac{\rho\omega^2}{2\lvert\mu\rvert}\left(1-\frac{\lvert\mu\rvert}{m}\right)}$	$\rho\omega^2\left(\frac{1}{m}+\frac{i}{\omega\eta}\right)$
Voigt	$\sqrt{\frac{\rho\omega^2}{2\lvert\mu\rvert}\left(1+\frac{m}{\lvert\mu\rvert}\right)}$	$\sqrt{\frac{\rho\omega^2}{2\lvert\mu\rvert}\left(1-\frac{m}{\lvert\mu\rvert}\right)}$	$\rho\omega^2\left[\frac{m+i\omega\eta}{m^2+(\omega\eta)^2}\right]$
SLS	$\sqrt{\frac{\rho\omega^2}{2\lvert\mu\rvert}\left(1+\frac{m_1}{\lvert\mu\rvert}+\frac{\omega^2\eta^2m_2}{\lvert\mu\rvert(m_2^2+\omega^2\eta^2)}\right)}$	$\sqrt{\frac{\rho\omega^2}{2\lvert\mu\rvert}\left(1-\frac{m_1}{\lvert\mu\rvert}-\frac{\omega^2\eta^2m_2}{\lvert\mu\rvert(m_2^2+\omega^2\eta^2)}\right)}$	$\frac{\rho\omega^2(m_2-i\omega\eta)}{m_1m_2-i\omega\eta(m_1+m_2)}$

Table 4.2: k for Maxwell, Voigt, and SLS models, where $k^2=\rho\omega^2/\mu$. Note that the wave speed will be $c=\omega/Re(k)$, and the attenuation constant will be $\gamma=Im(k)$

To compare these models, we will use realistic parameters for liver tissue given in [11].

4.4 Maxwell model

Using Table 4.2, we have for the Maxwell model

$$Det_{est}(L,R,\omega,m,\eta,\tilde{m},\tilde{\eta}) = e^{-L\sqrt{\frac{\rho}{2m\eta}\left(\frac{\omega m^2}{\sqrt{m^2+\omega^2\eta^2}+\omega\eta}\right)}}\frac{\rho\omega^2R^2}{6}\left(\frac{1}{m}-\frac{1}{\tilde{m}}\right).$$

Denoting the contrast of $\tilde{m}$ and m by $\alpha = \frac{\tilde{m}}{m}$, and the contrast of $\tilde{\eta}$ and η by $\beta = \frac{\tilde{\eta}}{\eta}$, we get

$$Det_{est}(L,R,\omega,m,\eta,\alpha,\beta) = e^{-L\sqrt{\frac{\rho}{2m\eta}\left(\frac{\omega m^2}{\sqrt{m^2+\omega^2\eta^2}+\omega\eta}\right)}}\frac{\rho\omega^2R^2}{6}\frac{\alpha-1}{\alpha m}.$$

Note that our estimated detectability does not depend on the viscosity of the inclusion. Thus the only noticeable difference between the inclusion and background is given by the contrast of elasticity, α. Below we list the limit behaviors of the detectability as $R \to 0$, $\alpha \to 1$, and $\alpha \to \infty$.

- As the inclusion shrinks ($R \to 0$), our estimated detectability converges to zero as expected, where the rate is $O(R^2)$. From Figure 4.3(a), Det_{est} is a good estimate of Det for small radius. Since we are focused on determining the smallest detectable tumor, Det_{est} will be useful in further studies.

- As the elasticity becomes homogeneous ($\alpha \to 1$), our detectability converges to zero as expected, since the viscosity of the inclusion does not appear in the equation. For Det, the limit is computable but complicated. With realistic parameters given in Figure 4.3(b), the limit of Det approaches different constants depending on β.

- As the contrast in elasticity approaches infinity ($\alpha \to \infty$), our detectability approaches a finite limit given by

$$\lim_{\alpha\to\infty} Det_{est} = e^{-L\sqrt{\frac{\rho}{2m\eta}\left(\frac{\omega m^2}{\sqrt{m^2+\omega^2\eta^2}+\omega\eta}\right)}}\frac{\rho\omega^2R^2}{6m}.$$

  When $\alpha \to \infty$, from Table 4.2, we can easily see $\tilde{c} \to \sqrt{\frac{2\omega\tilde{\eta}}{\rho}}$ and $\tilde{\gamma} \to \sqrt{\frac{\rho\omega}{2\tilde{\eta}}}$, which corresponds to $\tilde{k} \to \sqrt{\frac{\rho\omega}{\eta}}e^{i\frac{\pi}{4}}$. Thus, we expect both Det and Det_{est} to approach a finite limit as $\alpha \to$

∞. In fact $Det(L, R, k, \tilde{k}) \to Det\left(L, R, k, \sqrt{\frac{\rho\omega}{\eta}}e^{i\frac{\pi}{4}}\right)$ which can be calculated with realistic parameters as seen in Figure 4.3(b).

Since β does not appear in the definition of Det_{est}, we cannot investigate its limit. However, for the Maxwell model, larger viscosity means that the wave is less attenuating. In particular, if $\beta > 1$ and $\alpha = 1$, then the inclusion is less attenuating than the background, so $|u(0)| > 1$ and we expect negative detectability as seen in Figure 4.3(c) . Furthermore, as $\tilde{\eta} \to \infty$, then the dashpot in the Maxwell model (see Figure 4.2) becomes rigid implying that the inclusion will become non-attenuating. In other words, $\beta \to \infty$ implies that $\tilde{\mu} \to \tilde{m} \in \mathbb{R}$ (purely elastic) and hence $\tilde{\gamma} \to 0$. Thus, $\lim_{\beta\to\infty} Det(L, R, k, \tilde{k}) = Det(L, R, k, \sqrt{\rho\omega^2/\tilde{m}})$ which can be calculated with realistic parameters (see Figure 4.3(c)) and may be negative. If $\beta \to 0$, the inclusion is super-attenuating ($\tilde{\gamma} \to \infty$) and has zero wave speed. Thus, we expect $Det(L, R, k, \tilde{k}) \to e^{-L\cdot Im(k)}$ since $|u(0)| = 0$.

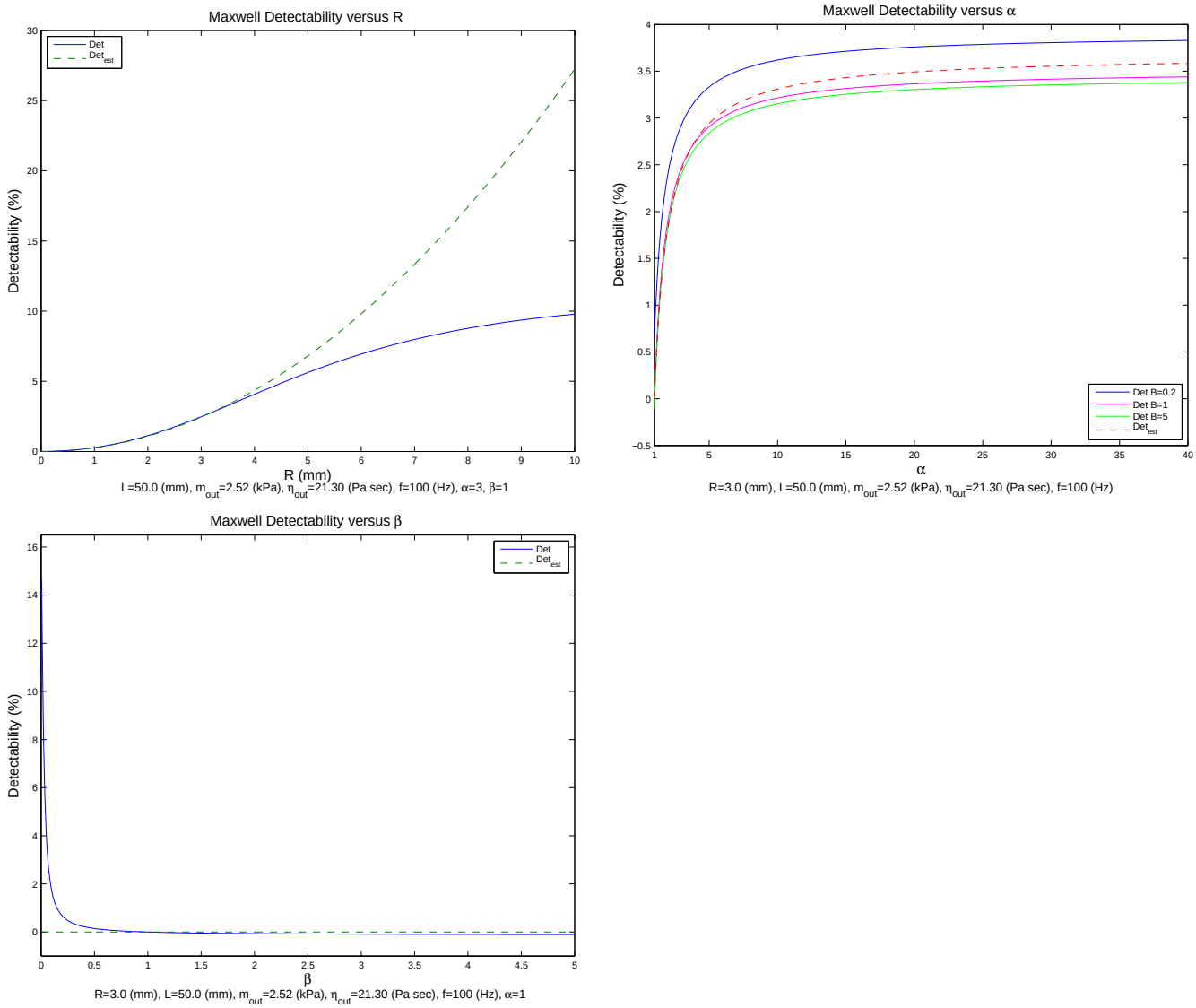

Figure 4.3: Det and Det_{est} for the Maxwell model as function of R, α, and β. Using the parameters given in the images, we found that $\lim_{\alpha\to 1} Det_{est} = 0\%$, $\lim_{\alpha\to 1} Det_{\beta=0.2} = 0.6611\%$, $\lim_{\alpha\to 1} Det_{\beta=1} = 0\%$, $\lim_{\alpha\to\infty} Det_{\beta=5} = -0.1055\%$, $\lim_{\alpha\to\infty} Det_{est} = 3.68\%$, $\lim_{\alpha\to\infty} Det_{\beta=0.2} = 3.897\%$, $\lim_{\alpha\to\infty} Det_{\beta=1} = 3.51\%$, $\lim_{\alpha\to\infty} Det_{\beta=5} = 3.453\%$, $\lim_{\beta\to 0} Det = 15.614\%$, and $\lim_{\beta\to\infty} Det = -0.13\%$

4.5 Voigt model

For the Voigt model, similarly with $\alpha = \frac{\tilde{m}}{m}$ and $\beta = \frac{\tilde{\eta}}{\eta}$, we have

$$Det_{est}(L, R, \omega, m, \eta, \alpha, \beta) = e^{-L\cdot\sqrt{\frac{\rho\omega^2}{2(m^2+\omega^2\eta^2)}\left(\sqrt{m^2+\omega^2\eta^2}-m\right)}}\frac{\rho\omega^2R^2}{6}\frac{m[\alpha m^2(\alpha-1)+\omega^2\eta^2(\beta^2-\alpha)]}{\alpha^2m^4+\beta^2\eta^4\omega^4+\omega^2m^2\eta^2(\beta^2+\alpha^2)},$$

which is now dependent on both the elasticity and viscosity of the inclusion. The limiting behaviors are as follows.

- As the inclusion shrinks ($R \to 0$), the estimated detectability converges to zero as expected, where the rate is $O(R^2)$ and for small R, Det_{est} is a good approximation to Det as seen in Figure 4.4 (a).

- As the elasticity becomes homogeneous ($\alpha \to 1$), the limit of the estimated detectability is a function of β:

$$\lim_{\alpha\to 1} Det_{est} = e^{-L\cdot\sqrt{\frac{\rho\omega^2}{2\sqrt{m^2+(\omega\eta)^2}}\left(1-\frac{m}{\sqrt{m^2+(\omega\eta)^2}}\right)}}\frac{\rho\omega^2R^2}{6}\frac{m\omega^2\eta^2(\beta^2-1)}{m^4+\beta^2\eta^4\omega^4+\omega^2m^2\eta^2(\beta^2+1)},$$

  which is not zero in general. If $\beta = 1$ (the inclusion becomes transparent), then the detectability approaches zero as expected (see Figure 4.4 (b)).

- As the contrast in elasticity approaches infinity ($\alpha \to \infty$), our estimated detectability approaches a finite limit given by

$$\lim_{\alpha\to\infty} Det_{est} = e^{-L\cdot\sqrt{\frac{\rho\omega^2}{2\sqrt{m^2+(\omega\eta)^2}}\left(1-\frac{m}{\sqrt{m^2+(\omega\eta)^2}}\right)}}\frac{\rho\omega^2R^2}{6}\frac{m}{m^2+\omega^2\eta^2}, \tag{4.5}$$

  which is independent of the viscosity contrast β. As $\alpha \to \infty$, the spring in the Voigt model becomes infinity stiff, and the inclusion then becomes modeled as a stiff rod (see Figure 4.2). Thus $\alpha \to \infty$ forces $\tilde{c} \to \infty$ and $\tilde{\gamma} \to 0$ independent of the viscosity of the inclusion $\tilde{\eta}$, and hence, the inclusion is now modeled as a stiff rod, so by Lemma 4.2, $Det(L, R, k, \tilde{k}) \to e^{-L\cdot Im(k)}\left(1 - \frac{3e^{Im(k)R}}{|3-k^2R^2-3ikR|}\right)$.

- As the viscosity becomes homogenous ($\beta \to 1$), the limit of the estimated detectability is a function of α:

$$\lim_{\beta\to 1} Det_{est} = e^{-L\cdot\sqrt{\frac{\rho\omega^2}{2\sqrt{m^2+(\omega\eta)^2}}\left(1-\frac{m}{\sqrt{m^2+(\omega\eta)^2}}\right)}}\frac{\rho\omega^2R^2}{6}\frac{m[\alpha m^2(\alpha-1)+\omega^2\eta^2(1-\alpha)]}{\alpha^2m^4+\eta^4\omega^4+\omega^2m^2\eta^2(1+\alpha^2)}.$$

  which is not zero in general. If $\alpha = 1$ (the inclusion becomes transparent), then the detectability approaches zero as seen in Figure 4.4.

- As the inclusion becomes infinitely viscous ($\beta \to \infty$), our detectability approaches the same limit as given in (4.5). This is not surprising because from Table 4.2 as $\beta \to \infty$ the attenuation within the inclusion approaches 0, but the wave speed in the inclusion approaches ∞, independent of $\tilde{m}$. Similar, to the case when $\alpha \to \infty$, in the inclusion, the model becomes a rigid rod as $\beta \to \infty$. Thus, we also get the same limit for Det as we did when $\alpha \to \infty$.

- When $\beta \to 0$, from Table 4.2, we see the inclusion becomes purely elastic ($\mu = m \in \mathbb{R}$), so

$$\lim_{\beta\to 0} Det_{est} = e^{-L\cdot\sqrt{\frac{\rho\omega^2}{2(m^2+\omega^2\eta^2)}\left(\sqrt{m^2+\omega^2\eta^2}-m\right)}}\frac{\rho\omega^2R^2}{6}\frac{m^2(\alpha-1)-\omega^2\eta^2}{\alpha m^3+\omega^2\eta^2m\alpha}$$

  and $Det(L,R,k,\tilde{k}) \to Det(L,R,k,\sqrt{\rho\omega^2/m})$. Note that our limits may be negative as in Figure 4.4 (c) since the inclusion is non-attenuating.

In Figure 4.4 (a), the attenuation is higher in the background than in the inclusion ($\gamma > \tilde{\gamma}$), but the wave speed is greater in the inclusion ($c < \tilde{c}$). Thus, for small radius, we have positive Det, but as the size of the inclusion increases, the effect of the attenuation increases and negative detectability is seen.

Remark 4.3 *In the Voigt model, attenuation approaches* 0*, when* $\eta \to 0$ *and when* $\eta \to \infty$*. One can show by simple calculus that maximum attenuation occurs when* $\eta = \frac{\sqrt{3}m}{\omega}$*. Thus, at maximum attenuation in the inclusion, we get* $\tilde{\eta} = \frac{\sqrt{3}\alpha m}{\omega}$ *and*

$$Det_{est} = e^{-L\cdot\sqrt{\frac{\rho\omega^2}{2(m^2+\omega^2\eta^2)}\left(\sqrt{m^2+\omega^2\eta^2}-m\right)}}\frac{\rho\omega^2R^2}{6}\left[\frac{m}{m^2+\omega^2\eta^2}-\frac{1}{4\alpha m}\right].$$

If the background and inclusion has maximum attenuation, then $\eta = \frac{\sqrt{3}m}{\omega}$, $\eta = \frac{\sqrt{3}m}{\omega}$, *and*

$$Det_{est} = e^{-L\cdot\sqrt{\frac{\rho\omega^2}{8m}}} \frac{\rho\omega^2 R^2}{24} \left[\frac{1}{m} - \frac{1}{\alpha m}\right].$$

Note the similarity between this and Det_{est} *for Maxwell.*

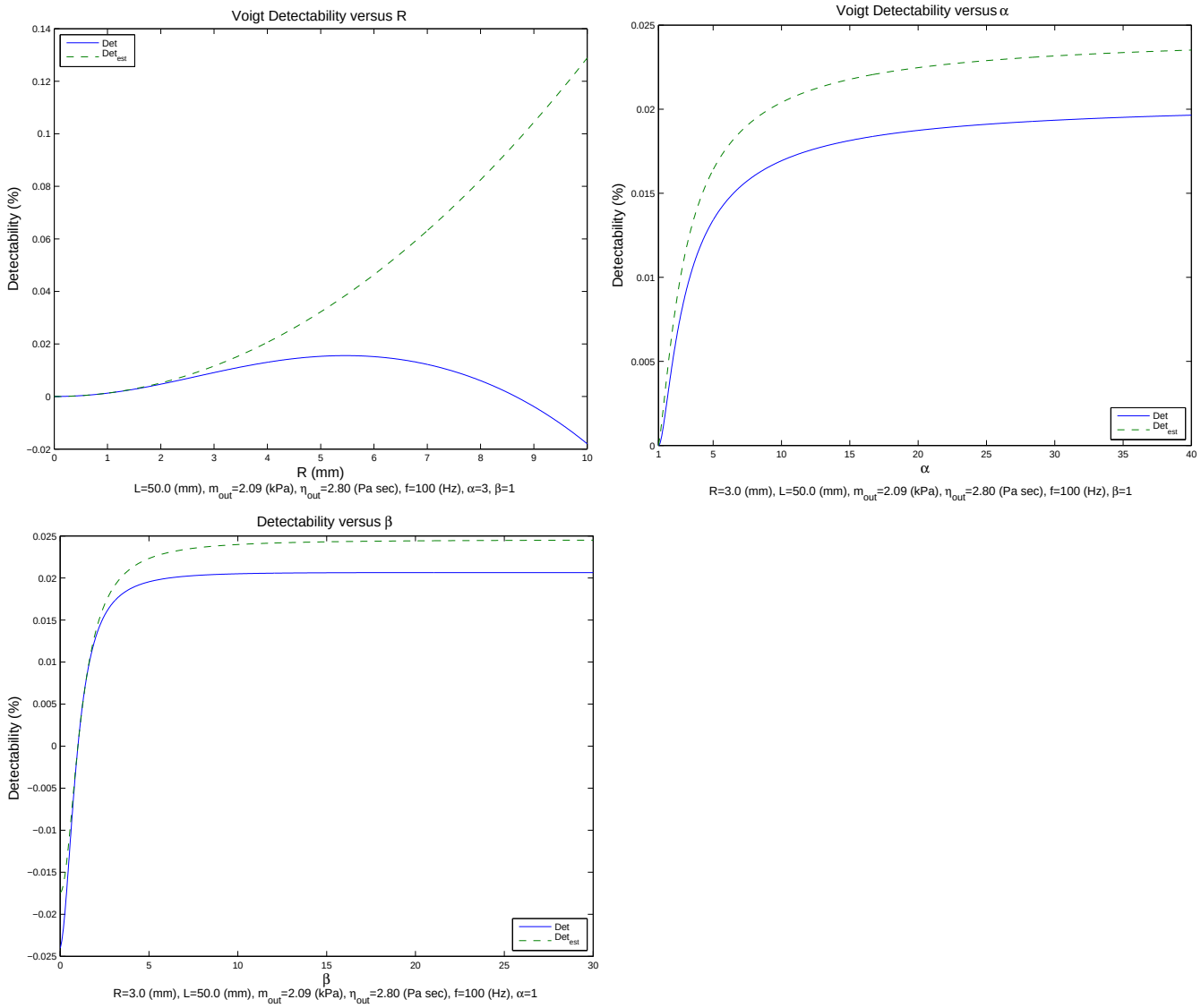

Figure 4.4: Det and Det_{est} for the Voigt model as function of R, α, and β. Using the parameters given in the images, we found that $\lim_{\alpha\to\infty} Det_{est} = 0.0246\%$, $\lim_{\alpha\to\infty} Det = 0.0205\%$, $\lim_{\beta\to 0} Det_{est} = -0.0174\%$, $\lim_{\beta\to 0} Det = -0.0240\%$, $\lim_{\beta\to\infty} Det_{est} = 0.0246\%$, and $\lim_{\beta\to\infty} Det = 0.0205\%$

4.6 SLS model

For the SLS model, we can rewrite (4.4) in terms of relevant parameters similar to the other models:

$$Det_{est}(L,R,\omega,m,\eta,\alpha_1,\alpha_2,\beta) = e^{-L\cdot Im(k)}\frac{\rho\omega^2R^2}{6}\left(\frac{m_1m_2^2+\omega^2\eta^2(m_1+m_2)}{m_1^2m_2^2+\omega^2\eta^2(m_1+m_2)^2}-\frac{\alpha_1\alpha_2^2m_1m_2^2+\omega^2\beta^2\eta^2(\alpha_1m_1+\alpha_2m_2)}{\alpha_1^2\alpha_2^2m_1^2m_2^2+\omega^2\beta^2\eta^2(\alpha_1m_1+\alpha_2m_2)^2}\right),$$

where $Im(k)$ is given in Table 4.2 and $\alpha_1 = \frac{\tilde{m}_1}{m_1}, \alpha_2 = \frac{\tilde{m}_2}{m_2}$, and $\beta = \frac{\tilde{\eta}}{\eta}$.

- As the inclusion shrinks ($R \to 0$), the estimated detectability converges to zero as expected, where the rate is $O(R^2)$, and for small R, Det_{est} is a good approximation to Det as seen in Figure 4.5 (a).

- As $\alpha_1 \to 1$, the limit of the estimated detectability is a function of α_2 and β:

$$\lim_{\alpha_1\to 1} Det_{est} = e^{-L\cdot Im(k)}\frac{\rho\omega^2R^2}{6}\left(\frac{m_1m_2^2+\omega^2\eta^2(m_1+m_2)}{m_1^2m_2^2+\omega^2\eta^2(m_1+m_2)^2}-\frac{\alpha_2^2m_1m_2^2+\omega^2\beta^2\eta^2(m_1+\alpha_2m_2)}{\alpha_2^2m_1^2m_2^2+\omega^2\beta^2\eta^2(m_1+\alpha_2m_2)^2}\right)$$

  which is not zero in general. If $\alpha_2 = \beta = 1$ (the inclusion vanishes), then the detectability approaches zero as expected (see Figure 4.5 (b)).

- As $\alpha_1 \to \infty$, our detectability approaches a finite limit given by

$$\lim_{\alpha_1\to\infty} Det_{est} = e^{-L\cdot Im(k)}\frac{\rho\omega^2R^2}{6}\left(\frac{m_1m_2^2+\omega^2\eta^2(m_1+m_2)}{m_1^2m_2^2+\omega^2\eta^2(m_1+m_2)^2}\right),$$

  which is independent of the viscosity of the inclusion $\tilde{\eta}$ and α_2. Similar to the Voigt model, as $\alpha_1 \to \infty$, the inclusion becomes modeled as stiff rod, so the wave speed in the inclusion approaches infinity and the attenuation in the inclusion approaches zero. Thus, $Det(L,R,k,\tilde{k}) \to e^{-L\cdot Im(k)}\left(1-\frac{3e^{Im(k)R}}{|3-k^2R^2-3ikR|}\right)$ (see Figure 4.5 (b)).

- As $\alpha_2 \to 1$, the limit of the estimate detectability is a function of α_1 and β:

$$\lim_{\alpha_2 \to 1} Det_{est} = e^{-L \cdot Im(k)} \frac{\rho \omega^2 R^2}{6} \left(\frac{m_1 m_2^2 + \omega^2 \eta^2 (m_1 + m_2)}{m_1^2 m_2^2 + \omega^2 \eta^2 (m_1 + m_2)^2} - \frac{\alpha_1 m_1 m_2^2 + \omega^2 \beta^2 \eta^2 (\alpha_1 m_1 + m_2)}{\alpha_1^2 m_1^2 m_2^2 + \omega^2 \beta^2 \eta^2 (\alpha_1 m_1 + m_2)^2} \right)$$

  which is not zero in general. If $\alpha_1 = \beta = 1$ (the inclusion vanishes), then the detectability approaches zero as expected (see Figure 4.5 (c)).

- As $\alpha_2 \to \infty$, our detectability approaches a finite limit given by

$$\lim_{\alpha_2 \to \infty} Det_{est} = e^{-L \cdot Im(k)} \frac{\rho \omega^2 R^2}{6} \left(\frac{m_1 m_2^2 + \omega^2 \eta^2 (m_1 + m_2)}{m_1^2 m_2^2 + \omega^2 \eta^2 (m_1 + m_2)^2} - \frac{\alpha_1 m_1}{\alpha_1^2 m_1^2 + \omega^2 \beta^2 \eta^2} \right).$$

  Note that as $\alpha_2 \to \infty$, the interior becomes modeled by the Voigt model with parameters $\tilde{m}_1$ and $\tilde{\eta}$. Thus, $Det(L, R, k, \tilde{k}) \to Det(L, R, k, \tilde{k}_{Voigt}(\tilde{m}_1, \tilde{\eta}))$ (see Figure 4.5 (c)). If $m_2 \to \infty$, then the estimated and true detectability will be the exact same as the estimated and true detectability for the Voigt model.

- As the viscosity becomes homogeneous ($\beta \to 1$), the limit of the estimated detectability is a function of α_1 and α_2:

$$\lim_{\beta \to 1} Det_{est} = e^{-L \cdot Im(k)} \frac{\rho \omega^2 R^2}{6} \left(\frac{m_1 m_2^2 + \omega^2 \eta^2 (m_1 + m_2)}{m_1^2 m_2^2 + \omega^2 \eta^2 (m_1 + m_2)^2} - \frac{\alpha_1 \alpha_2^2 m_1 m_2^2 + \omega^2 \eta^2 (\alpha_1 m_1 + \alpha_2 m_2)}{\alpha_1^2 \alpha_2^2 m_1^2 m_2^2 + \omega^2 \eta^2 (\alpha_1 m_1 + \alpha_2 m_2)^2} \right)$$

  which is not zero in general. If $\alpha_1 = \alpha_2 = 1$ (the inclusion vanishes), then the detectability approaches zero as expected (see Figure 4.5 (d)).

- When $\beta \to 0$, the estimated detectability approaches a finite limit given by:

$$\lim_{\beta \to 0} Det_{est} = e^{-L \cdot Im(k)} \frac{\rho \omega^2 R^2}{6} \left(\frac{m_1 m_2^2 + \omega^2 \eta^2 (m_1 + m_2)}{m_1^2 m_2^2 + \omega^2 \eta^2 (m_1 + m_2)^2} - \frac{1}{\alpha_1 m_1} \right),$$

  which is independent of α_2. This is not surprising, when $\beta = 0$, $\tilde{\eta} = 0$ will nullify the effect of $\tilde{m}_2$ (see Figure 4.2), thus the SLS unit become purely elastic ($\tilde{\mu} = \tilde{m}_1 \in \mathbb{R}$) and $Det(L, R, k, \tilde{k}) \to Det\left(L, R, k, \sqrt{\frac{\rho \omega^2}{\alpha_1 m_1}}\right)$ (see Figure 4.5 (d)).

  Note that our limit may be negative since the inclusion is non-attenuating.

- As the inclusion becomes infinitely viscous ($\beta \to \infty$), our detectability approaches a finite limit given by

$$\lim_{\beta\to\infty} Det_{est} = e^{-L\cdot Im(k)}\frac{\rho\omega^2 R^2}{6}\left(\frac{m_1 m_2^2 + \omega^2\eta^2(m_1+m_2)}{m_1^2 m_2^2 + \omega^2\eta^2(m_1+m_2)^2} - \frac{1}{\alpha_1 m_1 + \alpha_2 m_2}\right).$$

  In this case, the inclusion has become purely elastic ($\tilde{\mu} = \tilde{m}_1 + \tilde{m}_2 \in \mathbb{R}$), since the dashpot has become rigid (see Figure 4.2). Thus, $Det(L, R, k, \tilde{k}) \to Det\left(L, R, k, \sqrt{\frac{\rho\omega^2}{\alpha_1 m_1 + \alpha_2 m_2}}\right)$ (see Figure 4.5 (d)). If either α_1 or α_2 approaches infinity as $\beta \to \infty$, then the inclusion is modeled by a rigid rod and $Det(L, R, k, \tilde{k}) \to e^{-L\cdot Im(k)}\left(1 - \frac{3e^{Im(k)R}}{|3-k^2R^2-3ikR|}\right)$. Once again, our limit may be negative since the inclusion is non-attenuating.

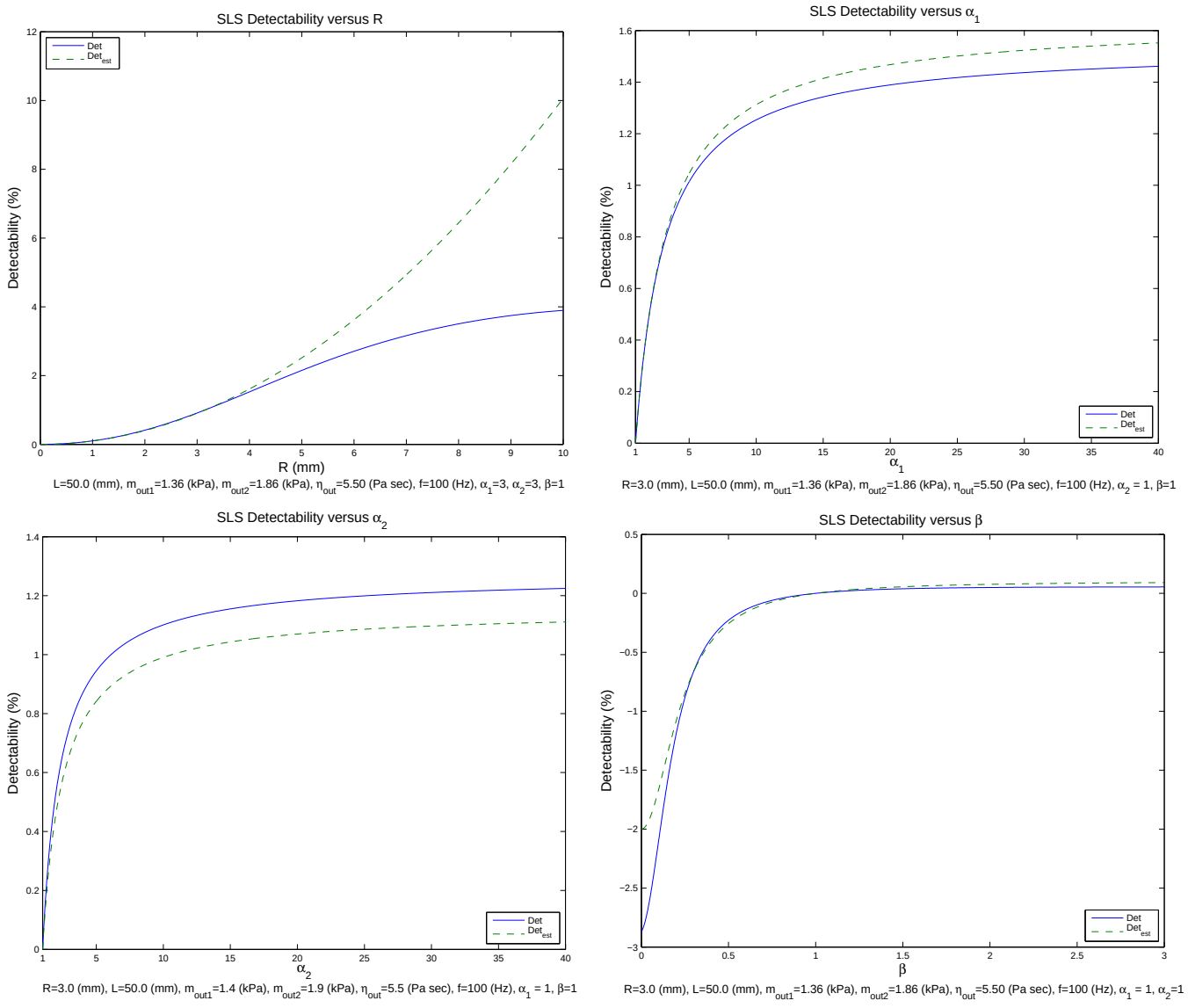

Figure 4.5: Det and Det_{est} for the SLS model as function of R, α_1, α_2 and β. Using the parameters given in the images, we found that $\lim_{\alpha_1\to\infty} Det_{est} = 1.6407\%$, $\lim_{\alpha_1\to\infty} Det = 1.5366\%$, $\lim_{\alpha_2\to\infty} Det_{est} = 1.1525\%$, $\lim_{\alpha_2\to\infty} Det = 1.2673\%$, $\lim_{\beta\to 0} Det_{est} = -1.9992\%$, $\lim_{\beta\to 0} Det = -2.8714\%$, $\lim_{\beta\to\infty} Det_{est} = 0.103\%$, and $\lim_{\beta\to\infty} Det = 0.0451\%$

4.7 Detectability as a function of frequency

It would also be useful to see the effect of frequency on detectability. However, the Taylor series we used for small inclusions in the previous sections is for kR and $\tilde{k}R$. Here the real components of k and $\tilde{k}$ are increasing functions of ω, so (4.4) obtained by this Taylor expansion is no more valid for high frequency, even if $R << 1$.

Hence, we analyze the original detectability before small inclusion approximation, (4.1):

$$Det(L,R,k,\tilde{k}) = e^{-L\cdot Im(k)}\left(1 - \left|\frac{\cos kR - i\sin kR}{\left(1-\frac{k^2}{\tilde{k}^2}\right)\frac{\sin\tilde{k}R}{\tilde{k}R} + \frac{k}{\tilde{k}}\left(\frac{k}{\tilde{k}}\cos\tilde{k}R - i\sin\tilde{k}R\right)}\right|\right).$$

For each model, we will investigate the behavior of $u(0)$ as $\omega \to \infty$, using the fact that

$$k_R := Re(k) = \sqrt{\frac{\rho\omega^2}{2|\mu|}\left(1+\frac{Re(\mu)}{|\mu|}\right)}$$
$$k_I := Im(k) = \sqrt{\frac{\rho\omega^2}{2|\mu|}\left(1-\frac{Re(\mu)}{|\mu|}\right)}$$

where each model differs by their definition of μ. Furthermore, using $\sin x = \frac{e^{ix}-e^{-ix}}{2i}$ and $\cos x = \frac{e^{ix}+e^{-ix}}{2}$, we will take advantage of the following form of $|u(0)|$:

$$|u(0)| = \frac{2Re^{k_I R}}{\left|\left(\frac{1}{\tilde{k}}\left(1-\frac{k^2}{\tilde{k}^2}\right)+iR\left(\frac{k^2}{\tilde{k}^2}-\frac{k}{\tilde{k}}\right)\right)e^{-\tilde{k}_I R}e^{i\tilde{k}_R R} + \left(\frac{1}{\tilde{k}}\left(\frac{k^2}{\tilde{k}^2}-1\right)+iR\left(\frac{k^2}{\tilde{k}^2}+\frac{k}{\tilde{k}}\right)\right)e^{\tilde{k}_I R}e^{-i\tilde{k}_R R}\right|}.$$

4.7.1 Maxwell

Using Tables 4.1 and 4.2, we note that

$$Re(k) = \sqrt{\frac{\rho\omega^2}{2}\left(\sqrt{\frac{1}{m^2}+\frac{1}{\omega^2\eta^2}}+\frac{1}{m}\right)} \qquad Im(k) = \sqrt{\frac{\rho\omega^2}{2}\left(\sqrt{\frac{1}{m^2}+\frac{1}{\omega^2\eta^2}}-\frac{1}{m}\right)}.$$

Then by taking the limit as $\omega \to \infty$, after a simple substitution we obtain the following.

Remark 4.4 *For the Maxwell model, as* $\omega \to \infty$,

$$c = \frac{\omega}{Re(k)} \to \sqrt{\frac{m}{\rho}}, \qquad \gamma = Im(k) \to \frac{\sqrt{m\rho}}{2\eta}, \qquad \frac{k^2}{\tilde{k}^2} \to \frac{\tilde{m}}{m} = \alpha.$$

Futhermore, since $arg(k^2) \in [0, \pi)$ *and the square root function is continuous in these quadrants,* $\frac{k}{\tilde{k}} \to \sqrt{\alpha}$.

In Figure 4.6, we can see the limit behavior for the wave speed, c, and attenuation, γ, for realistic parameters for the Maxwell model.

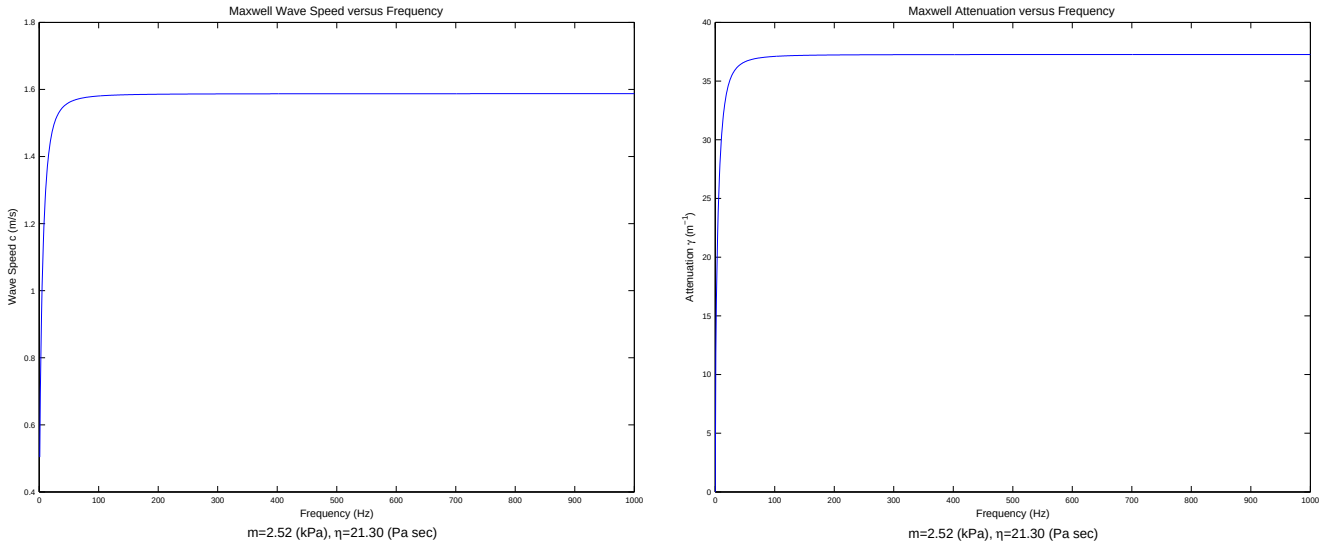

Figure 4.6: Wave speed and attenuation verus frequency for the Maxwell model. For these parameters, $\lim_{\omega\to\infty} c = 1.5875\ m/s$ and $\lim_{\omega\to\infty} \gamma = 37.2625\ m^{-1}$.

Using Remark 4.4, it follows that if $m < \tilde{m}$, then

$$\begin{aligned}
\lim_{\omega\to\infty} |u(0)| &\geq \lim_{\omega\to\infty} \frac{2Re^{k_I R}}{\left|\left(\frac{1}{\tilde{k}}\left(1-\frac{k^2}{\tilde{k}^2}\right)+iR\left(\frac{k^2}{\tilde{k}^2}-\frac{k}{\tilde{k}}\right)\right)e^{-\tilde{k}_I R}\right| + \left|\left(\frac{1}{\tilde{k}}\left(\frac{k^2}{\tilde{k}^2}-1\right)+iR\left(\frac{k^2}{\tilde{k}^2}+\frac{k}{\tilde{k}}\right)\right)e^{\tilde{k}_I R}\right|} \\
&\geq \lim_{\omega\to\infty} \frac{2Re^{k_I R}}{\left(\frac{1}{|\tilde{k}|}\left|1-\frac{k^2}{\tilde{k}^2}\right|+R\left|\frac{k^2}{\tilde{k}^2}-\frac{k}{\tilde{k}}\right|\right)e^{-\tilde{k}_I R}+\left(\frac{1}{|\tilde{k}|}\left|\frac{k^2}{\tilde{k}^2}-1\right|+R\left|\frac{k^2}{\tilde{k}^2}+\frac{k}{\tilde{k}}\right|\right)e^{\tilde{k}_I R}} \\
&= \frac{2e^{\frac{\sqrt{m\rho}}{2\eta}R}}{(\alpha-\sqrt{\alpha})\,e^{-\frac{\sqrt{\alpha m\rho}}{2\beta\eta}R}+(\alpha+\sqrt{\alpha})\,e^{\frac{\sqrt{\alpha m\rho}}{2\beta\eta}R}}
\end{aligned}$$

since $|\tilde{k}| \to \infty$ and $\alpha > 1$ and where we recall $\beta = \frac{\tilde{\eta}}{\eta}$. Thus, for the Maxwell model,

$$\lim_{\omega \to \infty} Det \leq e^{-L\frac{\sqrt{m\rho}}{2\eta}} \left(1 - \frac{2e^{\frac{\sqrt{m\rho}}{2\eta}R}}{(\alpha - \sqrt{\alpha})\, e^{-\frac{\sqrt{\alpha m\rho}}{2\beta\eta}R} + (\alpha + \sqrt{\alpha})\, e^{\frac{\sqrt{\alpha m\rho}}{2\beta\eta}R}} \right) \tag{4.6}$$

This implies that the detectability of the tumor is bounded when the frequency is increased. From Figure 4.7, we can see that Det for the Maxwell model oscillates, but for realistic parameters, the limit given in (4.6) is a very tight upper bound for high frequency.

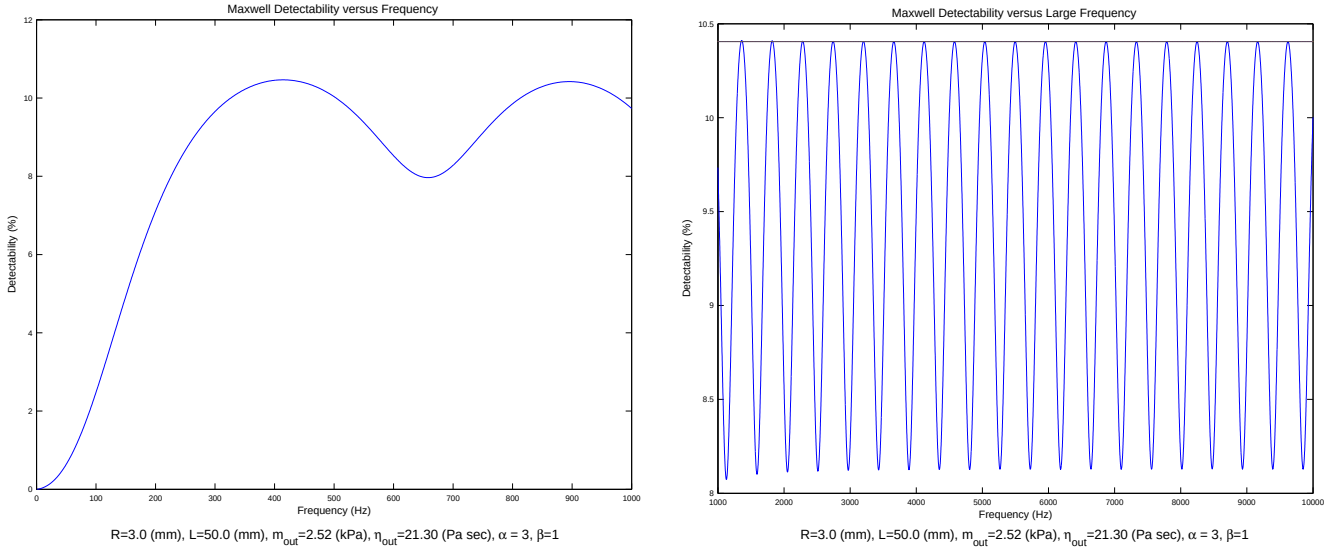

Figure 4.7: Maxwell detectability as a function of frequency. For realistic parameters, $\lim_{\omega \to \infty} Det \leq 10.4045\%$.

4.7.2 Voigt

From Tables 4.1 and 4.2, we get

$$Re(k) = \sqrt{\frac{\rho\omega^2}{2}\left(\frac{\sqrt{m^2 + \omega^2\eta^2} + m}{m^2 + \omega^2\eta^2}\right)} \qquad Im(k) = \sqrt{\frac{\rho\omega^2}{2}\left(\frac{\sqrt{m^2 + \omega^2\eta^2} - m}{m^2 + \omega^2\eta^2}\right)}.$$

After a simple substitution and by taking the limit, with respect to ω, we get the following.

Remark 4.5 *For the Voigt model, as* $\omega \to \infty$,

$$c = \frac{\omega}{Re(k)} \to \infty \qquad \gamma = Im(k) \to \infty \qquad \frac{k^2}{\tilde{k}^2} \to \frac{\tilde{\eta}}{\eta} = \beta.$$

Furthermore, since $arg(k^2) \in [0, \pi)$ *and the square root function is continuous in these quadrants,* $\frac{k}{\tilde{k}} \to \sqrt{\beta}$.

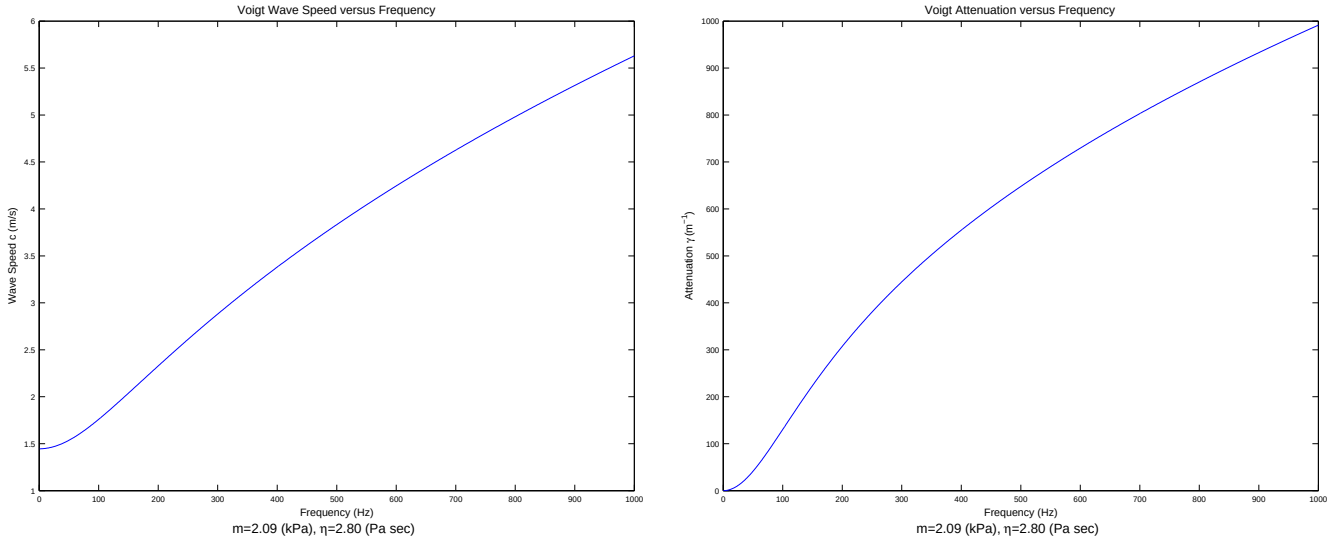

Figure 4.8: Wave speed and attenuation verus frequency for the Voigt model. Note, $\lim_{\omega\to\infty} c = \infty$ and $\lim_{\omega\to\infty} \gamma = \infty$.

From Figure 4.8, we can see that both wave speed and attenuation are increasing functions with respect to ω.

Using Remark 4.5, we get that

$$\begin{aligned}\lim_{\omega\to\infty} e^{(\tilde{k}_I - k_I)R}|u(0)| &= \lim_{\omega\to\infty} \frac{2R}{\left|\left(\frac{1}{\tilde{k}}\left(1 - \frac{k^2}{\tilde{k}^2}\right) + iR\left(\frac{k^2}{\tilde{k}^2} - \frac{k}{\tilde{k}}\right)\right) e^{-2\tilde{k}_I R} e^{i\tilde{k}_R R} + \left(\frac{1}{\tilde{k}}\left(\frac{k^2}{\tilde{k}^2} - 1\right) + iR\left(\frac{k^2}{\tilde{k}^2} + \frac{k}{\tilde{k}}\right)\right) e^{-i\tilde{k}_R R}\right|} \\ &= \frac{2}{\beta + \sqrt{\beta}}.\end{aligned}$$

And hence,

$$\lim_{\omega\to\infty} e^{-k_I L}|u(0)| = \lim_{\omega\to\infty} \frac{2}{\beta+\sqrt{\beta}} e^{-\tilde{k}_I R} e^{k_I(R-L)} = 0$$

since $R < L$. Thus,

$$\lim_{\omega\to\infty} Det = \lim_{\omega\to\infty} e^{-k_I L}\left(1 - |u(0)|\right) = 0.$$

Unlike the Maxwell model, Det for the Voigt model approaches 0 for high frequency, rather than oscillating. This is not suprising since the attenuation approaches infinity for high frequency implying that the wave decays completely before it reaches the inclusion. Furthermore, since $\lim_{\omega\to 0} Det = \lim_{\omega\to\infty} Det = 0$ and Det is continuous for $\omega > 0$, then there exists a maximum Det for given parameters and inclusion size. From Figure 4.9, we see that for realistic parameters for liver tissue the optimal frequency is about 33 Hz, and for breast tissue the optimal frequency is about 50 Hz.

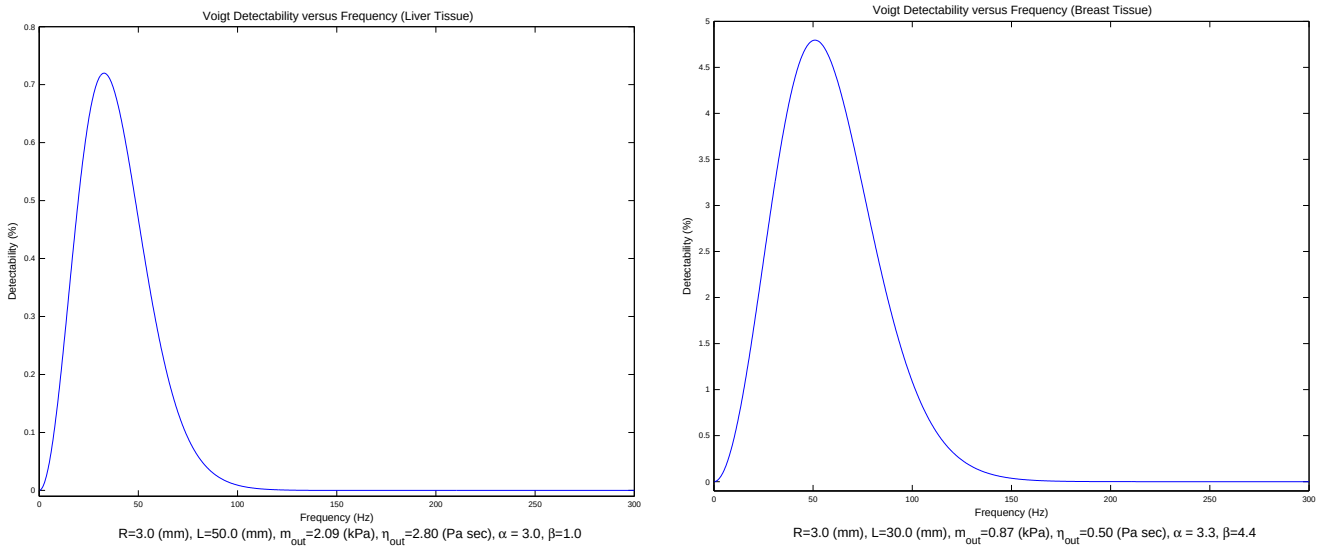

Figure 4.9: Voigt detectability as a function of frequency. For liver tissue, the optimal frequency is about $f = 33\ Hz$ and for breast tissue, it is about 50 Hz. In both cases, $\lim_{\omega\to\infty} Det = 0$.

4.7.3 SLS

From Tables 4.1 and 4.2, we get

$$Re(k) = \sqrt{\frac{\rho\omega^2}{2m_1}\left(\frac{\sqrt{(1+(\omega\tau_\epsilon)^2)(1+(\omega\tau_\sigma)^2)}+(1+\omega^2\tau_\epsilon\tau_\sigma)}{1+(\omega\tau_\sigma)^2}\right)}$$

$$Im(k) = \sqrt{\frac{\rho\omega^2}{2m_1}\left(\frac{\sqrt{(1+(\omega\tau_\epsilon)^2)(1+(\omega\tau_\sigma)^2)}-(1+\omega^2\tau_\epsilon\tau_\sigma)}{1+(\omega\tau_\sigma)^2}\right)}$$

where $\tau_\epsilon = \frac{\eta}{m_2}$ and $\tau_\sigma = \eta\left(\frac{1}{m_1}+\frac{1}{m_2}\right)$. Then after a simple substitution and by taking the limit with respect to ω, we get the following.

Remark 4.6 *For the SLS model, as* $\omega \to \infty$,

$$c = \frac{\omega}{Re(k)} \to \sqrt{\frac{m_1+m_2}{\rho}} \qquad \gamma = Im(k) \to \frac{m_2^2\sqrt{\rho}}{2\eta(m_1+m_2)^{3/2}} \qquad \frac{k^2}{\tilde{k}^2} \to \frac{\tilde{m}_1+\tilde{m}_2}{m_1+m_2} =: \chi.$$

Futhermore, since $arg(k^2) \in [0,\pi)$ *and the square root function is continuous in these quadrants,* $\frac{k}{\tilde{k}} \to \sqrt{\chi}$.

From Figure 4.10, we see the limit behaviors of wave speed and attenuation for realistic parameters for the SLS model.

From Remark 4.6, it follows that if $\chi > 1$, then

$$\begin{aligned}
\lim_{\omega\to\infty}|u(0)| &\geq \lim_{\omega\to\infty}\frac{2Re^{k_I R}}{\left|\left(\frac{1}{\tilde{k}}\left(1-\frac{k^2}{\tilde{k}^2}\right)+iR\left(\frac{k^2}{\tilde{k}^2}-\frac{k}{\tilde{k}}\right)\right)e^{-\tilde{k}_I R}\right|+\left|\left(\frac{1}{\tilde{k}}\left(\frac{k^2}{\tilde{k}^2}-1\right)+iR\left(\frac{k^2}{\tilde{k}^2}+\frac{k}{\tilde{k}}\right)\right)e^{\tilde{k}_I R}\right|} \\
&\geq \lim_{\omega\to\infty}\frac{2Re^{k_I R}}{\left(\frac{1}{|\tilde{k}|}\left|1-\frac{k^2}{\tilde{k}^2}\right|+R\left|\frac{k^2}{\tilde{k}^2}-\frac{k}{\tilde{k}}\right|\right)e^{-\tilde{k}_I R}+\left(\frac{1}{|\tilde{k}|}\left|\frac{k^2}{\tilde{k}^2}-1\right|+R\left|\frac{k^2}{\tilde{k}^2}+\frac{k}{\tilde{k}}\right|\right)e^{\tilde{k}_I R}} \\
&= \frac{2e^{\frac{m_2^2 R\sqrt{\rho}}{2\eta(m_1+m_2)^{3/2}}}}{\left(\chi-\sqrt{\chi}\right)e^{-\frac{(\alpha_2 m_2)^2 R\sqrt{\rho}}{2\beta\eta(\chi(m_1+m_2))^{3/2}}}+\left(\chi+\sqrt{\chi}\right)e^{\frac{(\alpha_2 m_2)^2 R\sqrt{\rho}}{2\beta\eta(\chi(m_1+m_2))^{3/2}}}}
\end{aligned}$$

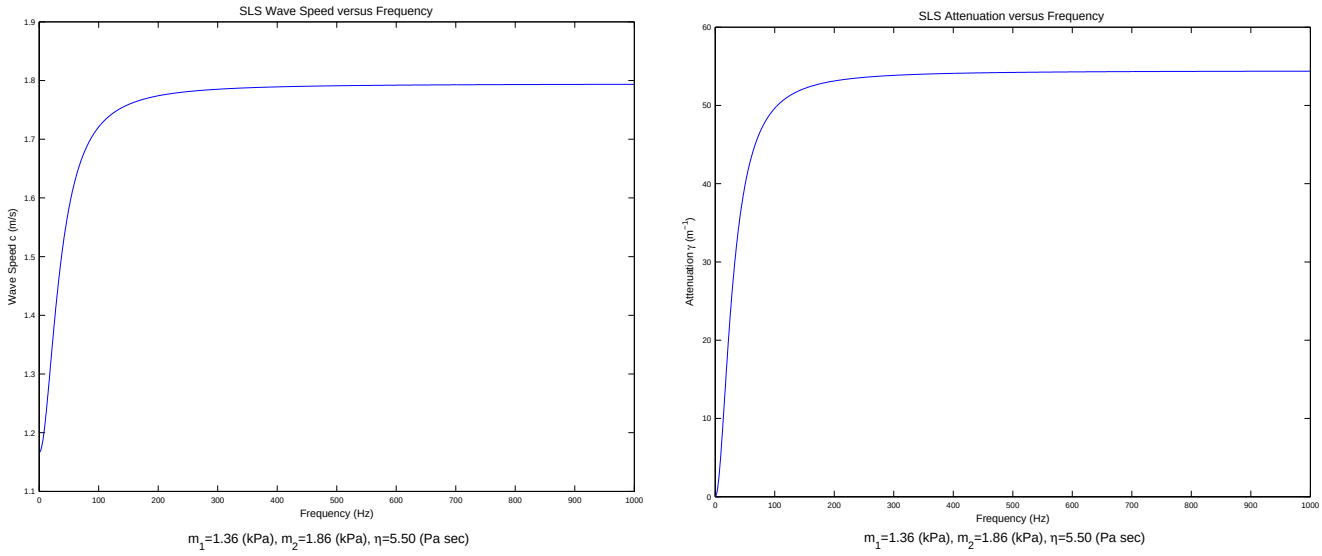

Figure 4.10: Wave speed and attenuation verus frequency for the SLS model. For these parameters, $\lim_{\omega\to\infty} c = 1.7944\ m/s$ and $\lim_{\omega\to\infty} \gamma = 54.4314\ m^{-1}$.

since $|\tilde{k}| \to \infty$. Hence, detectability is bounded for large ω:

$$\lim_{\omega\to\infty} Det \leq e^{-\frac{m_2^2 L\sqrt{\rho}}{2\eta(m_1+m_2)^{3/2}}} \left(1 - \frac{2e^{\frac{m_2^2 R\sqrt{\rho}}{2\eta(m_1+m_2)^{3/2}}}}{\left(\chi-\sqrt{\chi}\right)e^{-\frac{(\alpha_2 m_2)^2 R\sqrt{\rho}}{2\beta\eta(\chi(m_1+m_2))^{3/2}}} + \left(\chi+\sqrt{\chi}\right)e^{\frac{(\alpha_2 m_2)^2 R\sqrt{\rho}}{2\beta\eta(\chi(m_1+m_2))^{3/2}}}}\right).$$

Similar to the Maxwell model, *Det* for SLS oscillates with respect to ω, but the limit given above is a tight upper bound for high frequency for realistic parameters as seen in Figure 4.11.

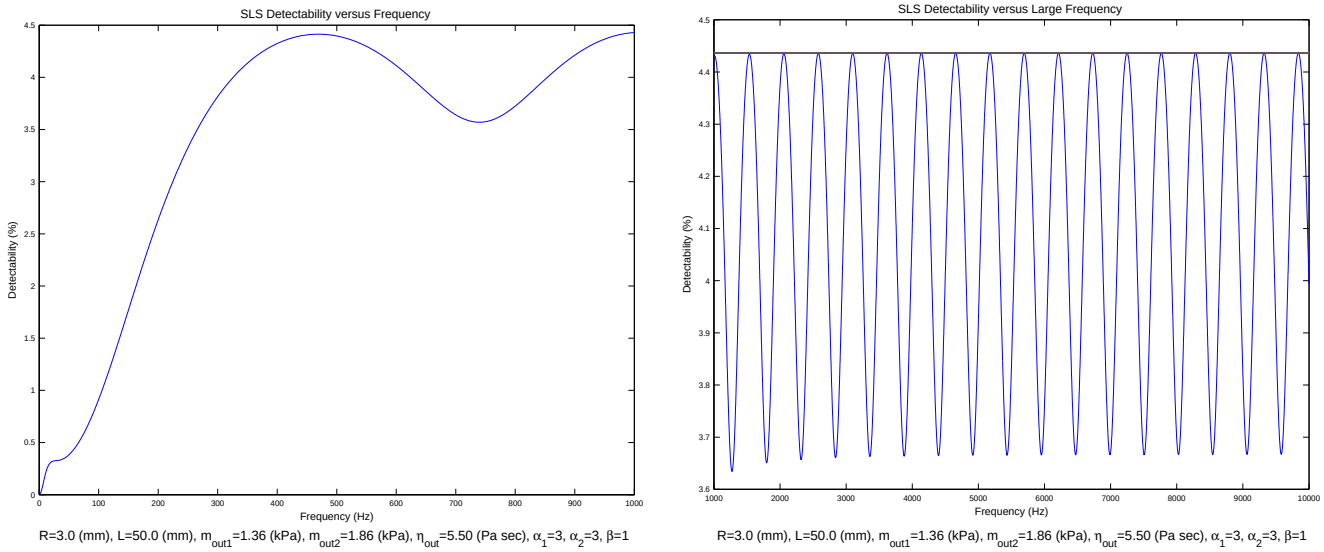

Figure 4.11: SLS detectability with respect to frequency. For the given parameters, $\lim_{\omega \to \infty} Det \leq 4.4363\%$.

4.8 Smallest detectable tumor

In this section, we try to determine the smallest detectable tumor under noisy conditions for breast and liver tissue. In order for an inclusion to be detectable, we require that the detectability be greater than the noise level ϵ. R_{true} and R_{est} will be the radii of the smallest inclusions that satisfies $Det > \epsilon$ and $Det_{est} > \epsilon$, respectively. Note that R_{true} does not have a nice exact form, but

$$R_{est} = \sqrt{\frac{6e^{LIm(k)}\epsilon}{Re(k^2 - \tilde{k}^2)}},$$

and we hope that R_{est} is a good approximation to R_{true}. For breast tissue, we use realistic parameters for the Voigt model given in [26], and for liver tissue, we use realistic parameters for the SLS model given in [2]. These parameters can be found in Table 4.3.

	Voigt Model (Breast Tissue)		SLS Model (Liver Tissue)		
	μ (kPa)	η (Pa sec)	μ_1 (kPa)	μ_2 (kPa)	η (Pa sec)
Background	0.87	0.5	1.160	1.970	7.3
Inclusion	2.871	2.2	2.910	4.830	14.40

Table 4.3: Realistic parameter for healthy and cancerous tissue. For breast tissue, the Voigt model was used with data obtained from [26] and for liver tissue, the SLS model was used with data from [2].

For the breast tissue, we use a near optimal frequency of 50 Hz, and for the liver, we use 100 Hz, since SLS does not have an optimal frequency. In both cases, the center of the tumor was assumed to be 30 mm from the wave source. The results for these parameters can be found in Table 4.4 for both the viscoelastic case and the purely elastic case.

	Breast Tissue ($f = 50\ Hz$)				Liver Tissue ($f = 100\ Hz$)			
	Voigt		Elastic		SLS		Elastic	
Noise (ϵ)	R_{true}	R_{est}	R_{true}	R_{est}	R_{true}	R_{est}	R_{true}	R_{est}
1%	1.37	1.38	0.87	0.88	1.73	1.75	0.87	0.88
5%	3.07	3.08	1.93	1.96	4.05	3.90	1.92	1.96
10%	4.54	4.35	2.71	2.78	7.05	5.52	2.69	2.77

Table 4.4: Smallest detectable tumor for breast and liver tissue under noisy conditions. Values were used from Table 4.3, and the center of the tumor was assumed to be 30 mm from the wave source. R_{true} (mm) represents the radius of the smallest detectable inclusion using Det, and R_{est} (mm) represents the radius of the smallest detectable inclusion using Det_{est}.

As can be see in the table, estimated detectability is a good approximation of the true detectability in breast tissue for both the viscoelastic and purely elastic model. For liver tissue, estimated detectability is also a good estimate for true detectability for low noise. For 10% noise, R_{true} for the viscoelastic case is large, so we do not expect R_{est} to be a good approximation. Also, note that the viscoelastic models are not able to detect smaller inclusions than the elastic model, which is expected.

Chapter 5

Reconstruction

5.1 Introduction

In this section, we propose a reconstruction algorithm for MRE data, where if we recall, u satisfies the Helmholtz equation, $\Delta u + k^2 u = 0$. For convenience, here we reconstruct k instead of μ, but observe that $k^2 = \frac{\rho\omega^2}{\mu}$. We also assume in this section that the material is purely elastic, so $\mu > 0$.

Our local wavelength reconstruction method is motivated by the observation that the measured wave from the MRE experiments looks primarily like a single plane wave on a small window, see Figure 5.1. So on this small window, the solution is assumed to have the form $u = Ae^{ik\mathbf{d}\cdot\mathbf{x}}$, where $A \in \mathbb{C}$ and $|\mathbf{d}| = 1$. Within the inclusion, we also assume a dominant plane wave exists. Both $Re(u)$ and $Im(u)$ show the dominant wave structure, and the algorithm will be run on both independently.

On a small window (33 pixels by 33 pixels in practice), our algorithm will first determine the direction of the wave. Once the direction is determined, crosscuts of the data will be taken in that direction. The wavelength of these crosscuts will be determined by a non-periodic Fourier transform technique, which will give the desired k.

This reconstruction algorithm will be tested on simulated and experimental data and will also be compared with another known direct inversion reconstruction method.

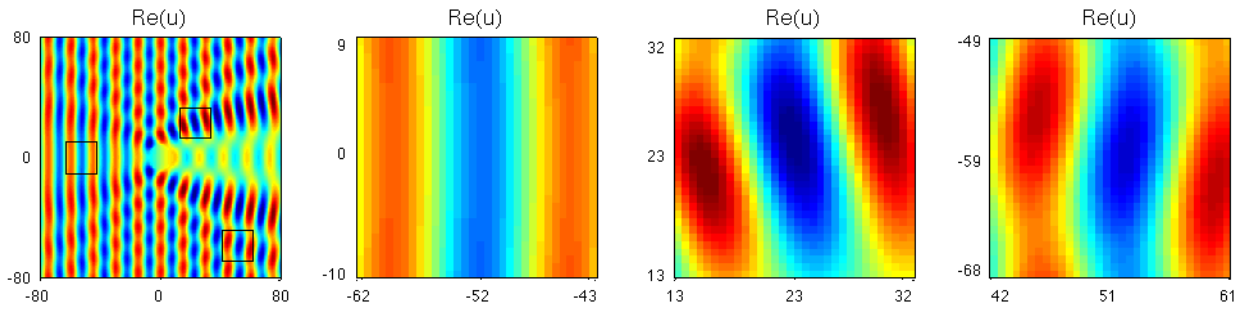

Figure 5.1: A small window is placed at three locations on $Re(u)$ to demonstrate the plane wave assumption.

5.2 Algorithm details for $Re(u)$

Around each point, $\mathbf{x_0} = (x_0, y_0)$, a square window $S = [-L, L] \times [-L, L]$ is placed, and it is assumed the solution has a dominant single plane wave on $\mathbf{x_0} + S$. Then the solution is represented by

$$u(\mathbf{x}) \approx \tilde{A} e^{ik\mathbf{d}\cdot(\mathbf{x_0}+\mathbf{x})} = A e^{ik\mathbf{d}\cdot\mathbf{x}}, \quad \forall \mathbf{x} \in S$$

where $A \in \mathbb{C} \setminus \{0\}$ depends on $\mathbf{x_0}$, $\mathbf{d}$ is the unit propagation direction, and $k \in \mathbb{R}$ is the desired wavenumber. Note for the detailed description of the algorithm, this paper will focus on just $Re(u)$, since the case for $Im(u)$ is very similar.

5.2.1 Finding the propagation direction, d

Let

$$f(\mathbf{x}) = |A| \cos\left(k\mathbf{d} \cdot \mathbf{x} + \phi\right) \approx Re(u), \quad \mathbf{x} \in S,$$

where $A = |A|e^{i\phi}$. It can be easily shown that $f(\mathbf{x}) = f(\mathbf{x}')$ if $(\mathbf{x} - \mathbf{x}') \perp \mathbf{d}$. Here we assume

$$\mathbf{d} = \left(\cos\theta, \sin\theta\right), \quad \theta \in [-\tfrac{\pi}{4}, \tfrac{\pi}{4}],$$

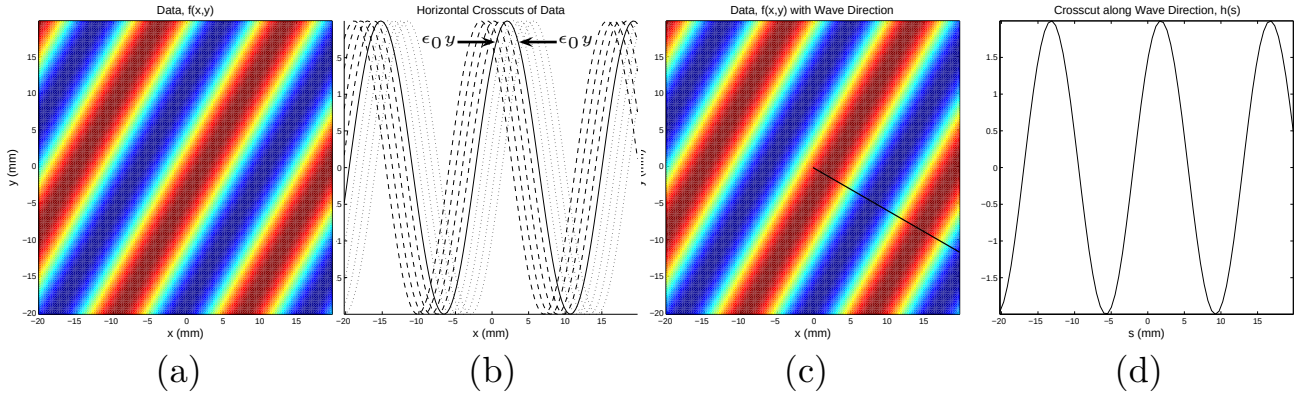

Figure 5.2: (a) The data, $f(x, y) \approx Re(u(x, y))$. (b) Several horizontal crosscuts of the data with $y > 0$ (dashed) and $y < 0$ (dotted). With proper shift $\epsilon_0 y$, all of the crosscuts will be shifted to the crosscut at $y = 0$ (solid). (c) The estimated wave direction is denoted by the solid line. (d) The crosscut along $\mathbf{d}$, $h(s)$, which will be an input of the estimation of k.

which means the propagation direction is *mainly horizontal* (the general case is discussed in section 5.3.2). Under this assumption, we have

$$f(x - \epsilon_0 y, y) = f(x, 0) \quad \text{for } \epsilon_0 = \tan\theta \in [-1, 1].$$

Thus we have

$$f(x - \epsilon_0 y, y) = \frac{1}{2L_y} \int_{-L_y}^{L_y} f(x - \epsilon_0 y', y')\, dy', \quad (x, y) \in S' = [-L_x, L_x] \times [-L_y, L_y]$$

where $S' \subseteq S$. Our goal is to find this optimal $\epsilon_0 \in [-1, 1]$. To do this we minimize the following average variance over $\epsilon \in [-1, 1]$:

$$\mathrm{Var}_f(\epsilon) := \frac{1}{4L_x L_y} \int_{-L_x}^{L_x} \int_{-L_y}^{L_y} \left| f(x - \epsilon y, y) - \frac{1}{2L_y} \int_{-L_y}^{L_y} f(x - \epsilon y', y')\, dy' \right|^2 dy\, dx. \tag{5.1}$$

Since we require $(x - \epsilon y, y) \in S$ for all $(x, y) \in S'$, our space S' will be dependent on ϵ. Later in section 5.3.1, we discuss how we chose L_x and L_y.

Figure 5.2.1 (a)-(c) illustrates the aforementioned steps to reconstruct $\mathbf{d}$. Figure 5.2.1 (d) becomes an input of the following step to reconstruct k.

5.2.2 Estimation of k

Once the propagation direction, $\mathbf{d}$, is determined, then consider a new coordinate system (s,t) with respect to $\mathbf{d}$ and $\mathbf{d}^{\perp}$: $\mathbf{x} = s\mathbf{d} + t\mathbf{d}^{\perp}$. Recalling that $f(\mathbf{x}) = f(\mathbf{x}')$ if $(\mathbf{x} - \mathbf{x}') \perp \mathbf{d}$, we get $f(s\mathbf{d}+t\mathbf{d}^{\perp}) = f(s\mathbf{d}) = |A|\cos(ks+\phi)$. Now we reduced our problem to a function of one variable. We expect to recover k by taking the Fourier transform of $h(s) := f(s\mathbf{d})$, $s \in [-L, L]$. Here the domain of s was maximized so that $s\mathbf{d}$ is in the window independent of $\mathbf{d}$. Look at the Fourier transform of $h(s)$; for $n \in \mathbb{Z} \setminus \{0\}$,

$$\begin{aligned}\hat{h}(n) &= \int_{-L}^{L} (|A|\cos(ks+\phi))\, e^{-i\frac{n\pi s}{L}}\, ds \\ &= |A|L\left(\mathrm{sinc}(kL - n\pi)e^{i\phi} + \mathrm{sinc}(kL + n\pi)e^{-i\phi}\right).\end{aligned}$$

Note that $\hat{h}(n) = 0$ if and only if $kL = p\pi$ for some $p \in \mathbb{N}$ and $n \neq \pm p$. Thus we can always find $n \in \mathbb{N}$ such that $\hat{h}(n) \neq 0$.

Lemma 5.1 *For $n \in \mathbb{N}$, let $w(n) := (-1)^n Re\left(\hat{h}(n)\right)$ and $v(n) := (-1)^n Im\left(\hat{h}(n)\right)$. Then*

$$\begin{aligned}\left((kL)^2 - (n\pi)^2\right) w(n) &= 2|A|kL^2\cos(\phi)\sin(kL), \\ \left((kL)^2 - (n\pi)^2\right)\frac{v(n)}{n} &= 2|A|\pi L\sin(\phi)\sin(kL).\end{aligned}$$

Proof. By performing integration by parts twice on $\hat{h}(n)$, one can easily derive the above equation. □

Theorem 5.2 *Let $n \in \mathbb{N}$ be such that $\hat{h}(n) \neq 0$ and $m \in \mathbb{N}$ with $m \neq n$. Then*

$$k = \frac{\pi}{L}\left(\frac{(nv(n) - mv(m))^2 + (n^2w(n) - m^2w(m))^2}{\left(\frac{v(n)}{n} - \frac{v(m)}{m}\right)^2 + (w(n) - w(m))^2}\right)^{1/4}. \tag{5.2}$$

Proof. Since the right hand sides of two identities in Lemma 5.1 are independent of n, equating the left hand sides with n and m, we get

$$(kL)^2(w(n)-w(m)) = \pi^2(n^2w(n)-m^2w(m)), \quad (kL)^2\left(\frac{v(n)}{n}-\frac{v(m)}{m}\right) = \pi^2(nv(n)-mv(m)),$$

which gives

$$(kL)^4\left[\left(\frac{v(n)}{n}-\frac{v(m)}{m}\right)^2+(w(n)-w(m))^2\right] = \pi^4\left[(nv(n)-mv(m))^2+(n^2w(n)-m^2w(m))^2\right].$$

Now it suffices to show that the left hand side never vanishes: Since $\hat{h}(n) \neq 0$, we must have $kL/\pi \notin \mathbb{N}$ or $kL = n\pi$. First, if $kL/\pi \notin \mathbb{N}$, then $\sin(kL) \neq 0$. From Lemma 5.1 we can easily see $w(n) \neq w(m)$ or $v(n)/n \neq v(m)/m$. If $kL = n\pi$, then $\hat{h}(m) = |A|L\left(\mathrm{sinc}((n-m)\pi)e^{i\phi}+\mathrm{sinc}(n+m)\pi)e^{-i\phi}\right) = 0$, which gives $v(m) = w(m) = 0$. Since $v(n) \neq 0$ or $w(n) \neq 0$ from $\hat{h}(n) \neq 0$, we can easily see the left hand side is not vanishing.

□

In practice, we will pick $n = \underset{j\in\mathbb{N}}{\mathrm{argmax}} \left|\hat{h}(j)\right|$ and m as the second largest component of the Fourier transform to minimize the noise effect.

5.3 Algorithm implementation

5.3.1 How to choose L_x and L_y

For a given $\epsilon \in [-1,1]$, recall the fact that we require $(x-\epsilon y, y) \in S$, for all $(x,y) \in [-L_x, L_x] \times [-L_y, L_y]$ in order for (5.1) to be well defined. This condition yields $L_x + |\epsilon|L_y \leq L$. Here, the size of L_y corresponds to the *number of crosscuts* which enhances the noise reduction, and the size of L_x corresponds to the *number of points* compared which enhances the field of view. Under the assumption that the noise levels are the same throughout the data, it is natural to maintain a constant noise reduction effect.

So we consider a constant L_y independent of ϵ in our implementation: When $|\epsilon| = 1$, the horizontal dominant wave assumption is barely satisfied since $|\theta| = \frac{\pi}{4}$. In order to handle this worst case, we pick $L_y = \frac{L}{2}$ which maximizes the *total number of points* in S involved in our comparison. With this $L_y = \frac{L}{2}$, we have $L_x = L - |\epsilon|\frac{L}{2}$ for all $\epsilon \in [-1, 1]$. For $|\epsilon| \neq 1$, this does not maximize the total number of points, but allows for a larger field of view maintaining the same level of noise reduction.

5.3.2 On the admissible set for $Var(\epsilon)$

In section 5.2.1 under the assumption of mainly horizontal propagation,

$$\epsilon_h := \underset{\epsilon\in[-1,1]}{\operatorname{argmin}} Var_f(\epsilon) \tag{5.3}$$

was used for ϵ_0, in the estimation of $\mathbf{d} = (\cos\theta, \sin\theta)$ where $\theta = \tan^{-1}(\epsilon_0)$. However, for the *mainly vertical* propagation directions, we may have $|\epsilon_0| \geq 1$ though $\epsilon_h \in [-1, 1]$. In this case, with the transposed data, $f^T(x, y) := f(y, x)$ on S, we may obtain

$$\epsilon_v := \underset{\epsilon\in[-1,1]}{\operatorname{argmin}} Var_{f^T}(\epsilon), \tag{5.4}$$

which can be used for $1/\epsilon_0$. Thus the use of the original and transposed data cover all possible $\mathbf{d}$ exclusively, and it suggests to use (5.3) while $\epsilon_h \in (-1, 1)$ and switch to (5.4) when $|\epsilon_h| = 1$. However, with actual data, the estimated ϵ_h and ϵ_v could be both in $(-1, 1)$; in this case, the minimum of $Var_f(\epsilon_h)$ and $Var_{f^T}(\epsilon_v)$ will decide ϵ_0.

5.3.3 Averaging $h(s)$

In section 5.2.2, in the estimation of k, we take the Fourier transform on $h(s) = f(s\mathbf{d})$. However, to achieve another level of noise reduction, we replace $h(s)$ by the following line integral:

$$h(s) \approx \frac{1}{|\gamma_s|}\int_{\gamma_s} f\, d\ell_t, \quad \gamma_s := \{s\mathbf{d} + t\mathbf{d}^\perp \in S'\}, \tag{5.5}$$

recalling the fact that $f(s\mathbf{d}) = f(s\mathbf{d} + t\mathbf{d}^\perp)$ on γ_s.

5.3.4 Discretization

We suppose f on S is discretized as follows:

$$F(i,j) := f(i\Delta x, j\Delta y), \quad i,j = 0, \pm 1, \pm 2, \ldots, \pm 2l,$$

which means $S = [-2l\Delta x, 2l\Delta x] \times [-2l\Delta y, 2l\Delta y]$ is discretized with $(4l+1)^2$ equidistant samples. Here the pixel size parameters, Δx and Δy, are provided along with MRE data. For simplicity, assume $\Delta x = \Delta y$. Then from section 5.3.1, $L_y = l\Delta x$ and set $L_x = \texttt{fl}[(2-|\epsilon|)l]\Delta x$. For the estimation of $\mathbf{d}$, we minimize the discretized version of (5.1):

$$\frac{1}{(2l_x^\epsilon + 1)(2l+1)} \sum_{i=-l_x^\epsilon}^{l_x^\epsilon} \sum_{j=-l}^{l} \left| F(i-\epsilon j, j) - \frac{1}{2l+1} \sum_{j'=-l}^{l} F(i-\epsilon j', j') \right|^2 .$$

where $l_x^\epsilon := \texttt{fl}[(2-|\epsilon|)l]$ which is always between l and $2l$, and $F(i-\epsilon j, j)$ is a linear interpolation of nearby data points for $i - \epsilon j \notin \mathbb{Z}$. For this one-dimensionl bounded minimization problem for ϵ_0, the golden section search algorithm is used through `fminbnd` in MATLAB. For (5.5), we also use a linear interpolation, and to calculate $\hat{h}(n)$, we use `fft` in MATLAB.

In our case, $N = 256$ and best results were found with $l = 8$, which corresponds to total box size of $4l + 1 = 33$.

5.4 Direct inversion method

Recall the scalar Helmholtz equation, $\Delta u + k^2 u = 0$, and that our goal is to reconstruct k. So a direct inversion method would be to solve for k by just using $k = \sqrt{\frac{-\Delta u}{u}}$; however, the second derivative on noisy u could be troublesome. From the experimental data, we observe that amplitude of the wave is more robust to the noise than the phase. So decompose u into amplitude and phase as in [18]: $u(x,y) = M(x,y)e^{i\phi(x,y)}$, where $M = |u| \geq 0$ and $\phi \in \mathbb{R}$. Plugging back into the Helmholtz equation and multiplying by $e^{-i\phi}$, we get

$$(\Delta M - M|\nabla\phi|^2 + k^2 M) + i(M\Delta\phi + 2\nabla M \cdot \nabla\phi) = 0.$$

Solving for k, we see that

$$k = \sqrt{\frac{M|\nabla\phi|^2 - \Delta M}{M}},$$

where only the first derivative of phase appears. Here note that $|\nabla\phi|^2 = \left|\nabla\left(\frac{Re(u)}{|u|}\right)\right|^2 + \left|\nabla\left(\frac{Im(u)}{|u|}\right)\right|^2$ can be easily obtained from the given data. To estimate ΔM and $\nabla\phi$, we use the five point stencil and the centered difference, both of which have $O(h^2)$ convergence for $\phi, M \in C^2$. In actual implementation, we adopt Anderssen's idea [3] to get a stable estimate of the numerical derivatives:

$$\nabla g \approx \left(\frac{G(x+h,y) - G(x-h,y)}{2h}, \frac{G(x,y+h) - G(x,y-h)}{2h}\right),$$

and

$$\Delta g \approx \frac{G(x-2h,y) + G(x+2h,y) + G(x,y-2h) + G(x,y+2h) - 4G(x,y)}{h^2},$$

where $G(X,Y)$ is the average of g on a square of side $2h$ centered at (X,Y). We will denote this reconstruction of k by k_{DIM}.

5.5 Simulations

We consider a constant background medium of stiffness μ that contains a small circular inclusion of constant stiffness $\tilde{\mu}$ and radius R with the following physical parameters, which are matching to the experimental data from Mayo clinic:

$$R = 8\ mm,\ \rho = 1000\ kg/m^3,\ \mu = 20\ kPa,\ \tilde{\mu} = 130\ kPa, \text{ and frequency is } 300\ Hz, \tag{5.6}$$

which give $k \approx 421\ m^{-1}$, $\tilde{k} \approx 165\ m^{-1}$ and wavelengths $\lambda \approx 15\ mm$, $\tilde{\lambda} \approx 38\ mm$. It should be noted that the diameter of the inclusion is similar to λ_{ext} and much smaller than $\tilde{\lambda}$. For the discrete data, we use $\Delta x = \Delta y = 0.6275\ mm$ to match the Mayo clinic phantom data. We assume a plane wave, $u_i = e^{ikx}$, is incident.

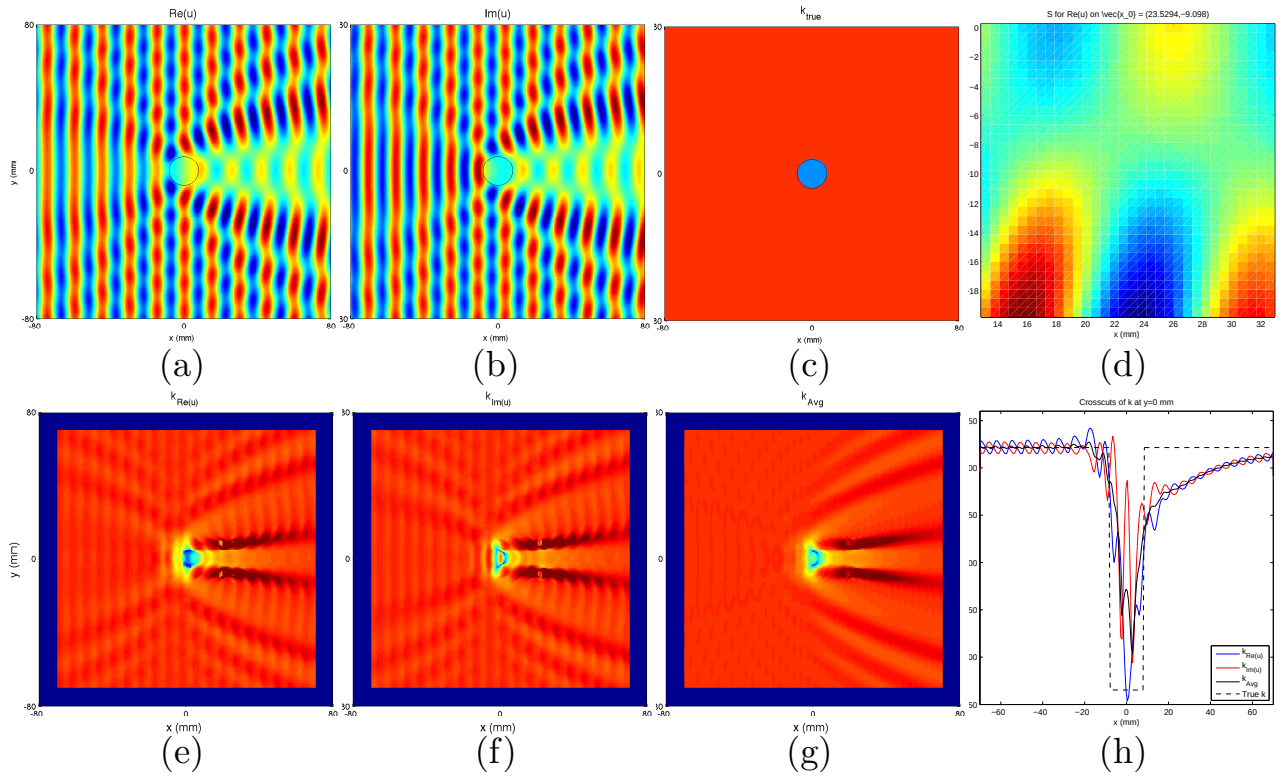

Figure 5.3: (a) and (b) show $Re(u)$ and $Im(u)$ of the simulated data with the parameters given in (5.6). (c) shows the true value for k. (d) is an example of the data on a reconstruction window, which in particular shows a strong interference pattern. (e) and (f) show the reconstruction on $Re(u)$ and $Im(u)$ respectively, and (g) is the average of the two reconstructions. (h) shows the crosscuts of $k_{Re(u)}$, $k_{Im(u)}$ and k_{Avg} at $y = 0$.

5.5.1 Comparison of reconstructions from $Re(u)$ and $Im(u)$

Solving the Helmholtz equation with the given parameters, we obtain $Re(u)$ and $Im(u)$ which are shown in Figure 5.3 (a) and (b). Observe the interference patterns, stronger behind the inclusion (for example, see (d)), which deviate from the plane wave assumption and yield unwanted patterns in the reconstructions shown in Figure 5.3 (e) and (f). However, the patterns in the reconstructions are in fact alternating to each other, seen in Figure 5.3 (h). So we expect an averaging of the reconstructions will smooth out the patterns, which suggests $k_{Avg} := (k_{Re(u)} + k_{Im(u)})/2$ shown in Figure 5.3 (g). k_{Avg} greatly reduces the pattern except two overestimated regions which are shown in dark red behind the inclusion, where the interference pattern is too

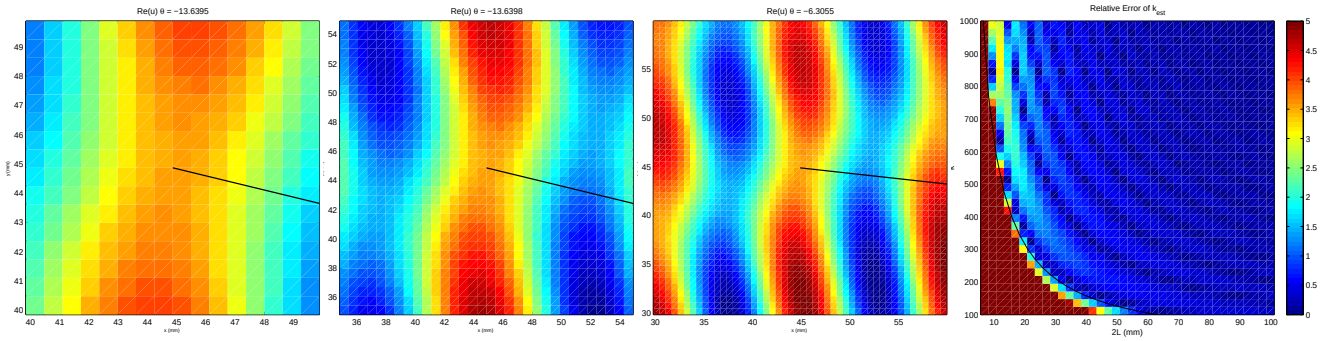

Figure 5.4: (a)-(c) show the calculated propagation direction, $\mathbf{d}$, at the same point for window sizes $17\Delta x, 33\Delta x,$ and $49\Delta x$. (d) is the relative error of the calculated wave number with varying k and box size $2L$. The black line in (d) is $k = \pi/L$, which represents when S covers one wavelength exactly.

strong as shown in Figure 5.3 (d). Overall, the average reconstructed value in the background is $422 \pm 19\ m^{-1}$, and in the inclusion $300 \pm 63\ m^{-1}$.

5.5.2 Effect of window size

Our reconstruction algorithm consists of two parts, the propagation direction using minimum variance and the wave number using Fourier transform. Because the wave is not a plane wave, it is not possible to estimate the error in the direction. However, our algorithm seems to capture the average propagation direction of the shown data, as window size varies in Figure 5.4 (a)-(c). On the other hand, to see the effect of the window size on the Fourier transform based wave number reconstruction, a plane wave is tested with known direction.

Figure 5.4 (d) indicates that the Fourier Transform part produces less than 3.4% error as long as $2L \geq \lambda$, where the error is relative error averaged over arbitrary phase. When $2L = n_0\lambda$, then the error is exactly zero since $\hat{h}$ shows only one peak at n_0, which is represented by the dark blue strips. However, if $2L < \lambda$, our algorithm may perform poorly because our algorithm does not utilize $\hat{h}(0)$. Also, as $2L$ approaches zero, the error becomes increasingly large. In summary, $2L \geq \lambda$ will be enough for the reconstruction of the homogeneous medium.

When the homogeneous background contains a stiffer inclusion, it will require $2L \geq \lambda$ for a

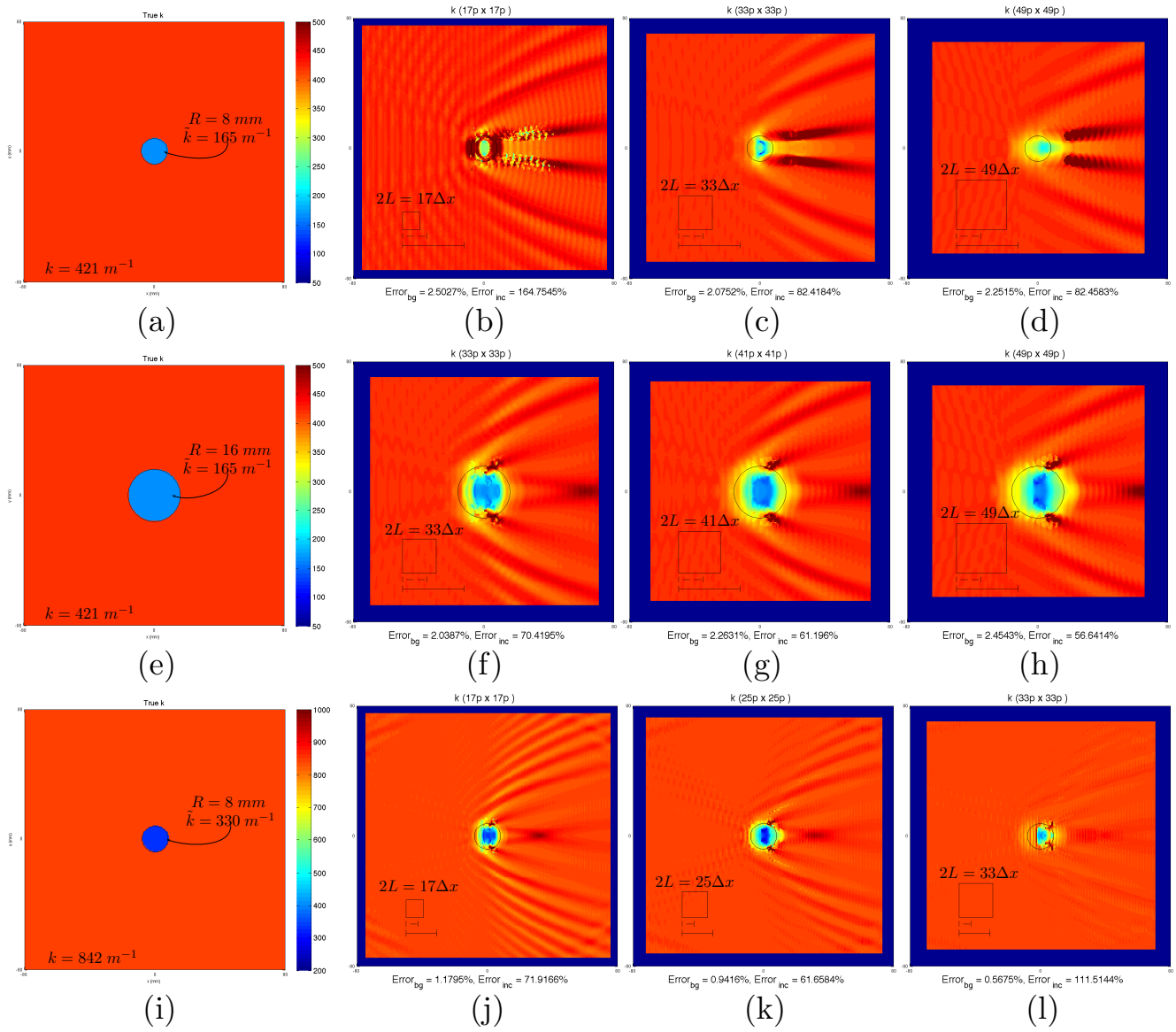

Figure 5.5: Reconstruction results with varying box sizes. Box sizes, with sides of length $2L$, are drawn along with $\tilde{\lambda}$ in the solid line and λ in the dashed line. $\Delta x = 0.6275\ mm$.

good background reconstruction, since the scattered wave away from the inclusion is dominated by the incident plane wave. Figure 5.5 verifies our expectation. If $2L > \lambda$, which occurs for all cases except for (b), the errors in the background are within 2.5% where the error is defined as

$$\frac{1}{|\Omega_{bg}|} \int_{\Omega_{bg}} \left| \frac{k(x) - k}{k} \right| dx.$$

In (b), the error happens to be 2.5% even though $2L < \lambda$.

A larger $2L$ smoothes out the interference patterns but also the interface of the inclusion. For the inclusion reconstruction, it will require a larger box because the corresponding wavelength is larger. However, if S is large in comparison to the inclusion, it cannot avoid containing the unwanted background points, which results in poor resolution. Thus, small inclusion with large stiffness is the most challenging case, which can be seen in (a)–(d). For this case the optimal $2L$ seems to occur at (c).

For a larger inclusion, it is possible to use larger box sizes without harming the resolution. As a result, the larger box sizes will cover more of the interior wavelength which will improve the reconstruction as seen in Figure 5.5 (e)–(h). In this case, the box size for (g) seems to compromise the best between interior wavelength and resolution.

If k is large, then the wavelength will be small, and we have a chance to use small boxes. This is beneficial if the inclusion is small, since small boxes will improve the resolution of the tumor as seen in Figure 5.5 (i)–(l). For (j) and (k), both box sizes are smaller than the inclusion and cover $0.56\tilde{\lambda}$ and $0.88\tilde{\lambda}$, but the smaller box size in (j) shows more interference pattern in the background. Furthermore, the larger box size of (l) harms the resolution of the inclusion, so in this case (k) seems to be the best reconstruction.

5.5.3 Effect of Noise

We investigate the noise effect using the absolute noise in the data proportional to the amplitude of the incident wave:

$$Re(u) = Re(u_{true}) + n|u_i|X$$

where X is uniformly distributed random variable between -1 and 1, n is the noise level, and we use the optimal box size obtained in the previous section. Also, a similar noise characteristics for $Im(u)$ is assumed. To study the effects of the noise only, the noisy reconstructions will be compared with the zero noise reconstruction given in Figure 5.5 (c).

For the simple plane wave case, where the zero noise reconstruction is simply $k_{true} = 421$,

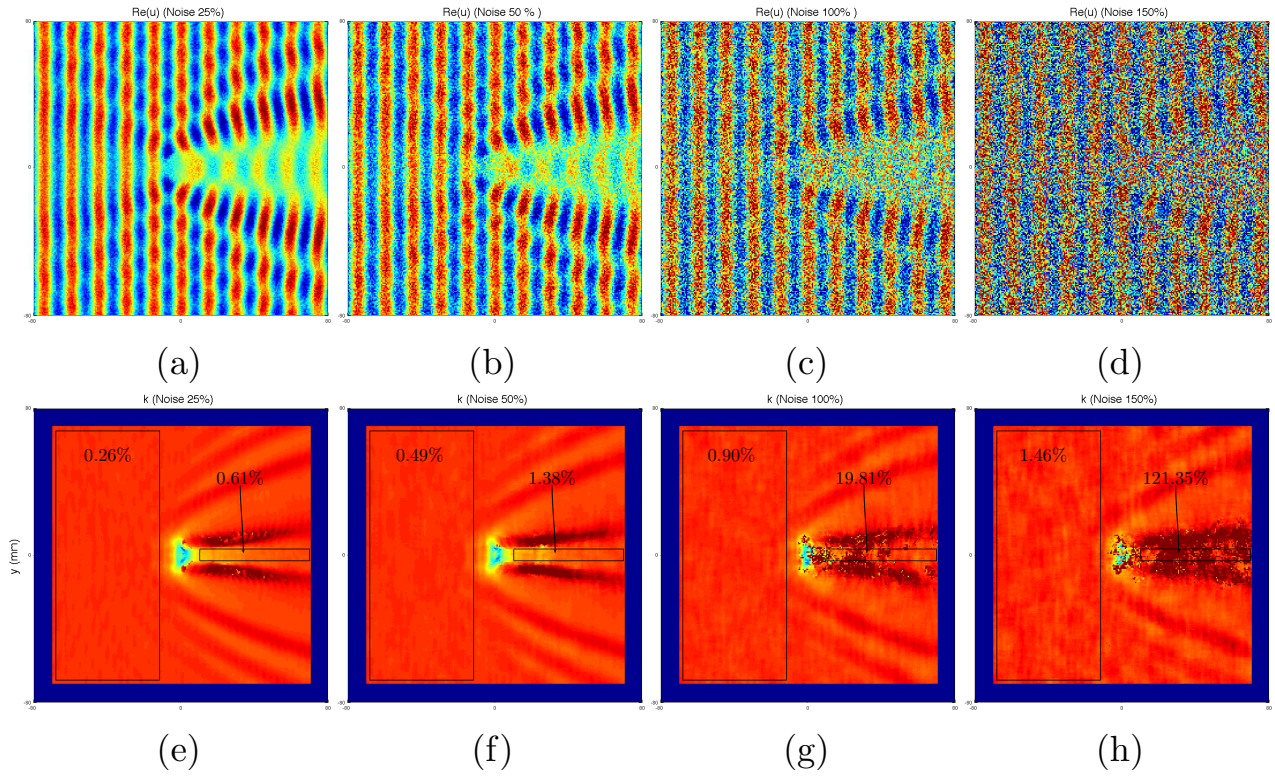

Figure 5.6: The top row shows the data and the bottom row shows the reconstruction for noise levels $10\%, 50\%, 100\%, 150\%$ from left to right. The numbers in the boxes are the average relative error, with respect to the zero noise reconstruction, in that region.

more than 1000 reconstructions were performed to obtain the average relative error shown in Table 5.1.

Noise Level (%)	50	100	150	200	250	300	350	400	450
Avg. Rel. Error (%)	0.46	0.91	1.35	2.04	3.92	19.50	29.49	62.43	123.71

Table 5.1: Average relative error for the simple plane wave case.

For the inclusion case, it should be noted that areas of low amplitude experience much higher noise level in a relative sense. Roughly, behind and in the inclusion, the amplitude is 33% of $|u_i|$ which corresponds to 3 times higher relative noise than that in front of the inclusion. For any method, it is expected that these low amplitude regions will have less stable reconstructions under noisy conditions. For example, when the absolute noise level is 50% as in Figure 5.6 (f), the

region behind the inclusion has an average relative error of 1.38%, while in front of the inclusion the average relative error is 0.49%. This is consistent with Table 5.1.

Figure 5.6 shows the overall stable reconstructions up to 100%, compared to the zero noise case given in Figure 5.5 (c). For the regions in front of the inclusion, the reconstruction is still stable up to 150% noise, but the low amplitude regions are poorly reconstructed as expected by the exponential growth in Table 5.1.

Note that the poor reconstruction of inclusion and the caustic regions is not from the noise, but from violation of the plane wave assumption which already exists in the 0% noise case.

The effects of the noise to the variance function $Var_f(\epsilon)$ was also investigated. Recall that in actual implementation, the data is discrete as described in Section 5.3.4. Thus, let $var_f(\epsilon)$ be the discretized version of $Var_f(\epsilon)$. Since noise is a function of random variables, we can calculate the expectation of our variance functions as given in the following theorem:

Theorem 5.3 *When $\tilde{f} = f + \delta$ where $\delta \sim nU[-1,1]$, we have*

$$E[\mathrm{Var}_{\tilde{f}}(\epsilon)] = \mathrm{Var}_f(\epsilon) + \frac{n^2}{3},$$

$$E\left[var_{\tilde{f}}(\epsilon)\right] = var_f(\epsilon) + \frac{2ln^2\bar{\beta}(\epsilon)}{3(2l+1)}.$$

where $2l+1$ corresponds to the box size and $\bar{\beta} : [-1,1] \to \left(\frac{1}{2}, 1\right]$ is an even function determined by the interpolation as defined in the Appendix.

Proof. See Theorem 6.2 and 6.5 in the Appendix for the proof. □

In Figure 5.7, the angle reconstruction with noise and the corresponding variance function are shown for a region in front of the inclusion. As noise increases, local peaks due to $\bar{\beta}(\epsilon)$ (see Figure 6.4) are amplified causing errors in the reconstruction of the angle. In Figure 5.7, this error is about 5°. As shown in Figure 5.6, the overall reconstruction is not significantly altered by this minor error in angle.

A more complete statistical analysis of $Var_{\tilde{f}}(\epsilon)$ and $var_{\tilde{f}}(\epsilon)$ is provided at the end of the thesis in the Appendix.

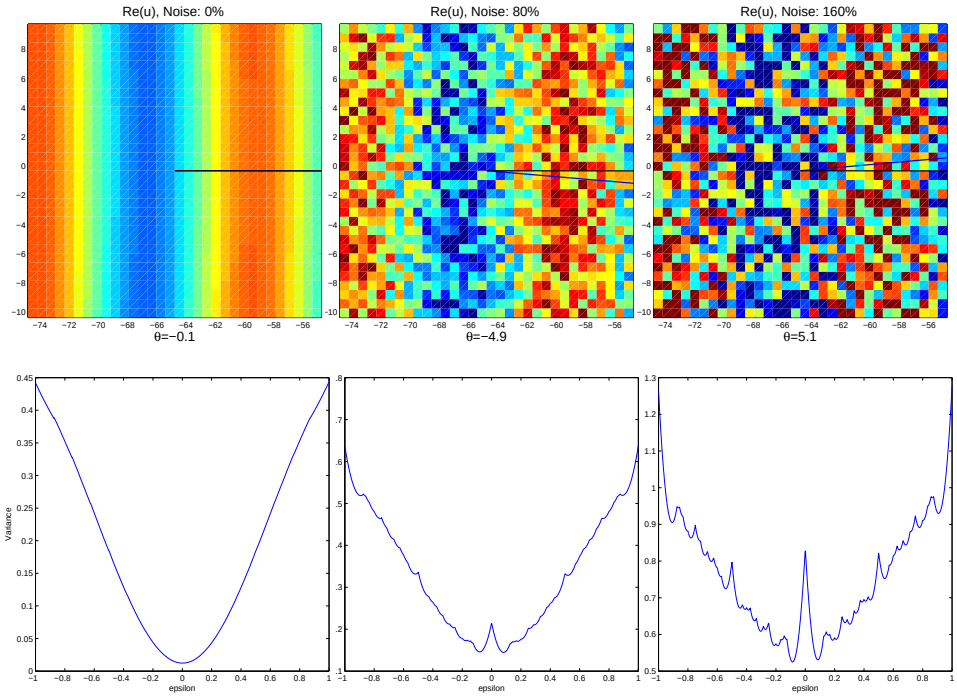

Figure 5.7: The first row shows the data and angle reconstruction for noise levels $0\%, 80\%$, and 160% for a window in front of the inclusion. The blue lines represent the calculated angle and the black lines are the calculated angle for the 0% noise case. The second row is the corresponding variance function which was minimized to calculate the angle.

5.6 Direct inversion method simulations

We also would like to look at how the direct inversion method is affected by box size and noise level. Since the direct inversion method is a derivative based algorithm, smaller boxes are expected to give a better reconstruction with no noise. However, with noise, the larger boxes will be more stable. Because the direct inversion method is derivative based, it is expected that it will be less stable in the low amplitude regions, behind and in the inclusion. Figure 5.8 verifies our expectation with $2h = (2s+1)\Delta x$, $s = 1, 2, 3$. When $s = 1$, the reconstruction becomes

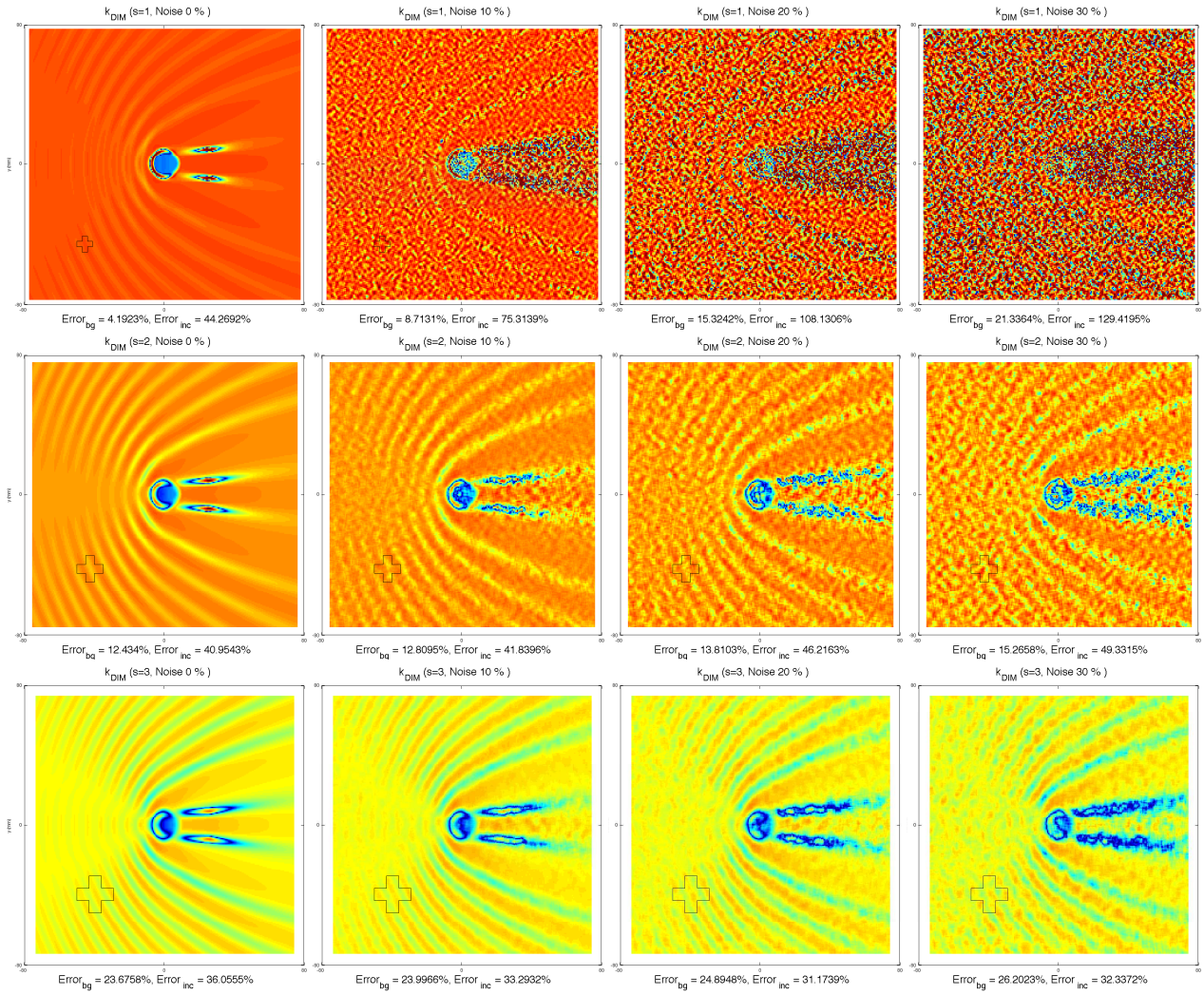

Figure 5.8: Reconstruction of k using the direct inversion method with varying box size and noise level. The rows are for $s = 1, 2, 3$ with corresponding boxes depicted in each figure. The columns are for $0\%, 10\%, 20\%, 30\%$ noise

very unstable with the noise. When $s = 3$, the reconstruction values are overall very poor, even though it is more stable to the noise. Thus, $s = 2$ compromises between the values and the stability, which gives nice circular inclusions with more accurate values (excluding the very front on the interior). However, when compared to the wave direction-based reconstruction method, the background reconstruction is worse in all aspects, such as poor values, unwanted patterns, and unwanted shadow behind the inclusion.

5.7 Hybrid method combining k_{Avg} and k_{DIM}

From previous sections, we may expect the direct inversion method can enhance the inclusion reconstruction from the wave direction-based method. For the inclusion reconstructions, note also that the direct inversion method underestimate k while the wave direction-based method overestimates it. A simple way of such hybrid is a weighted average of k_{Avg} and k_{DIM}:

$$k_p = pk_{Avg} + (1-p)k_{DIM}, \quad 0 \le p \le 1.$$

A natural choice is $p = \frac{1}{2}$. Another choice is $p = \frac{2}{3}$, since k_{Avg} is in fact a combination of two reconstructions from $Re(u)$ and $Im(u)$. Figure 5.9 shows these two choices; up to 30% noise, $k_{\frac{2}{3}}$ gives acceptable reconstructions. Though $k_{\frac{2}{3}}$ is not as good as k_{Avg} in the background, it shows a better reconstruction of inclusion, both in the value and the shape. Compare Figure 5.9 (g) with Figure 5.6 (e) or (f).

5.8 Experimental data

Using a gelatin-agar phantom data from the Mayo Clinic, we compare the different reconstruction methods as seen in Figure 5.10.

The Mayo Clinic phantom contains two 3.5% agar cylinder inclusions embedded in the homogeneous background with 1.5% agar. One has diameter 16 mm at $x = 70$ mm and $y = 90$ mm, and the other one has diameter 3 mm at $x = 77$ mm and $y = 58$ mm. The external compression test shows the designed stiffness values; $\tilde{\mu} = 130(\pm 10)$ kPa and $\mu = 20(\pm 3)$ kPa, which corresponds to $\tilde{k} = 165(\pm 7)$ m^{-1} and $k = 421(\pm 36)$ m^{-1}. A 300 Hz shear plane wave is generated by the attached transducer which vibrates parallel to the cylinders. See Figure 5.10(a) for this configuration.

As expected from the simulations, k_{Avg}, shown in Figure 5.10 (c), gives a smooth reconstruction in the background, and k_{DIM} in (d) gives a better reconstruction of inclusion. However, k_{DIM} gives unwanted patterns in the background which could be misdiagnosed, especially behind the inclusion, where the amplitude is low. From a visual inspection between Figure 5.10 (b) and Figure 5.6 (a), the phantom data seems to correspond to 25% absolute noise simulation case (62.5%

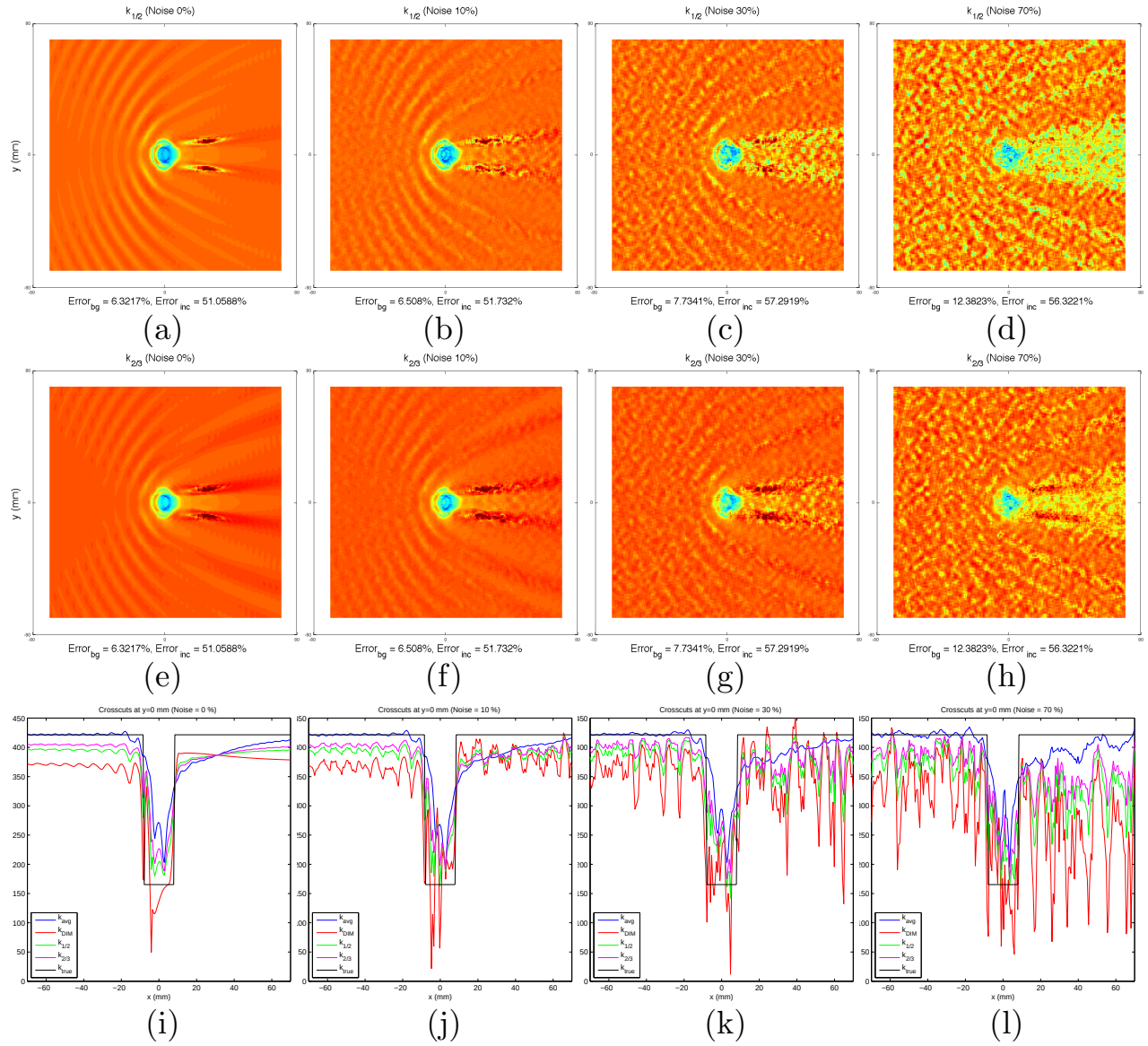

Figure 5.9: The first two rows are the hybrid reconstructions, $k_{\frac{1}{2}}$ and $k_{\frac{2}{3}}$. The third row is the crosscuts of k_{Avg}, k_{DIM}, $k_{\frac{1}{2}}$, $k_{\frac{2}{3}}$ at $y = 0\ mm$. The columns are for 0%, 10%, 30%, and 70% noise.

relative noise behind and in the inclusion).

The wave direction-based reconstruction, which is based on the plane wave assumption, was unable to reconstruct the smaller cylinder inclusion, since no distinguishable wave patterns could be found in the data from this inclusion. The direct inversion method, which is derivative based, may be able to reconstruct it. To maintain a fair comparison, in this paper, all of the methods have

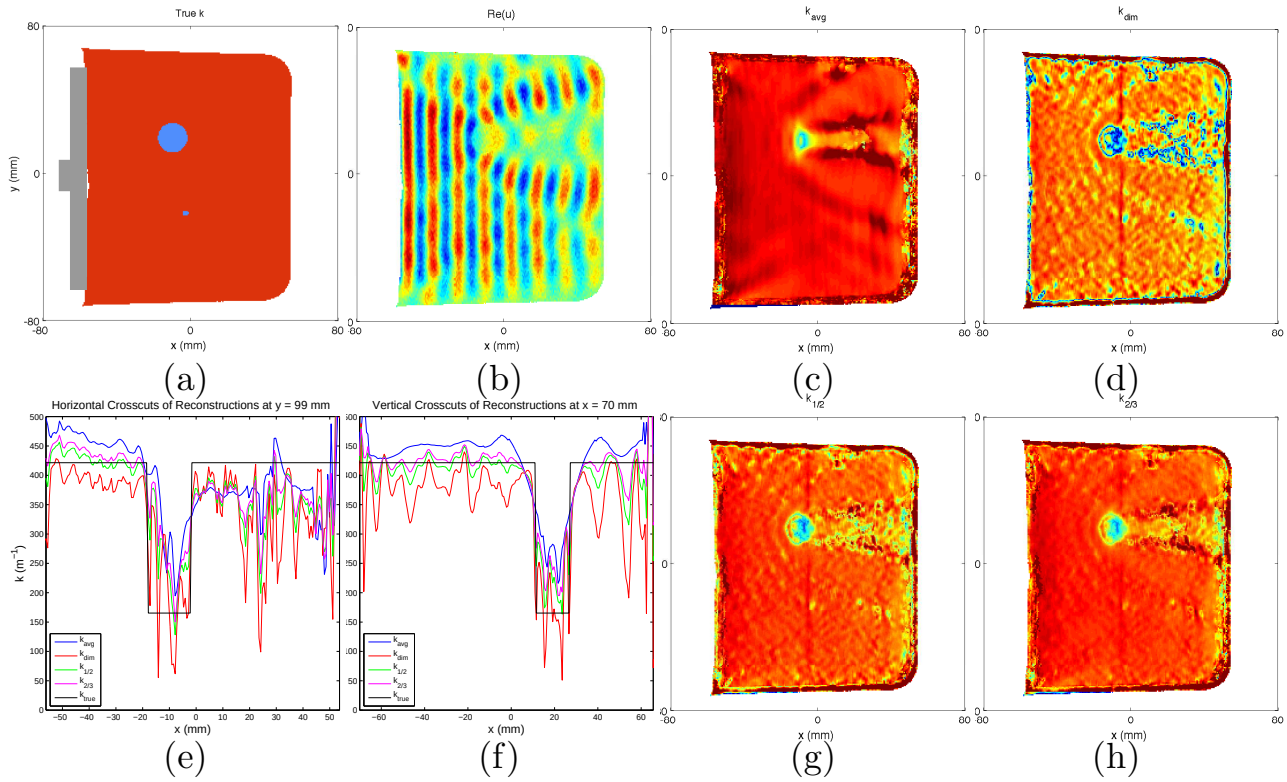

Figure 5.10: (a) is $Re(u)$ from experimental data. (b)-(d) are the k_{Avg}, k_{DIM}, and $k_{\frac{2}{3}}$ reconstructions.

no post processing like median filter, so in Figure 5.10 (d), the small inclusion is indistinguishable from other artifacts. Using the hybrid method, $k_{\frac{2}{3}}$ in (h) maintained the strong reconstruction of the background from k_{Avg}, and k_{DIM} enhanced the reconstruction of the inclusion, both value-wise and in shape. $k_{\frac{1}{2}}$ in (g) shows similar features, but not as strong as $k_{\frac{2}{3}}$.

Chapter 6

Conclusions and Future Work

By using the viscoelastic model, our given definition of detectability gives a more realistic limitation of MRE machines than the purely elastic case. In particular, the smallest detectable tumor is larger than in the purely elastic case because of the wave decay, which was successfully quantified in this thesis. For example, in breast tissue with a noise level of 5%, the smallest detectable tumor is 1.93 mm for the purely elastic case and 3.07 mm for the viscoelastic case. It also gives a good model for why tumors farther from the source wave are harder to detect as expected. Detectability also gives some insight about the spring-dashpot models such as the optimal frequency in the Voigt model, which was approximately 50 Hz for breast tissue. However, this definition of detectability assumed the effects from the compression wave were negligible. A more complete analysis has been performed within the research group which studies viscoelastic medium with respect to both the shear and compression wave [28]. The definition of detectability may also be extended to include the visible phase shift that also occurs because of the inclusion. Detectability may also be extended to other hybrid imaging techniques for cancer detection to provide a fair comparison.

The local wavelength reconstruction is a stable reconstruction and when combined with the direct inversion method suggested in [18], it provides an accurate reconstruction as well, which was extensively tested with simulated and clinical data in this thesis. Moreover, in order to improve the reconstruction for actual human tissue, the method needs to be extended to viscoelastic medium.

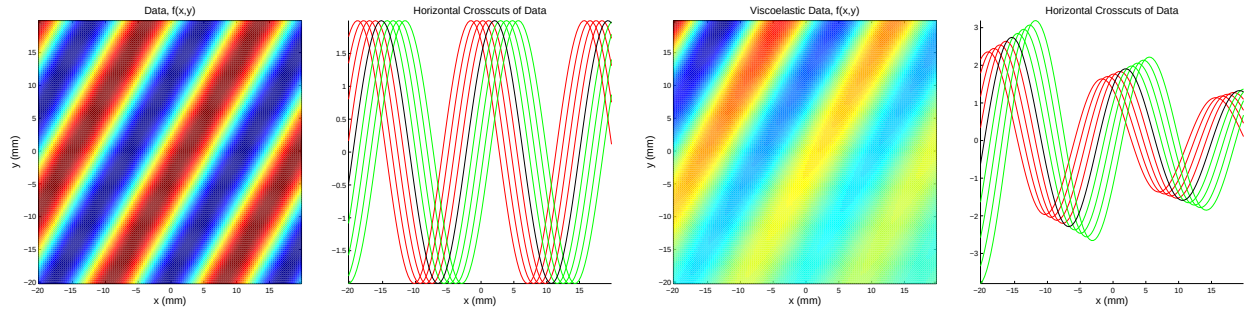

Figure 6.1: A graph of purely elastic data and its crosscuts used for "stacking" in the wave direction based algorithm, and a graph of viscelastic data and its crosscuts. For viscoelastic data, the crosscuts can longer be simply stacked.

The difficulty in this extension is that the "stacking curves" portion may not be valid, because we do not have shifted copies any more (see Figure 6). Both the incident wave and the scattering wave will be decaying, resulting in a shifted and scaled copies. As a result, a new minimization parameter will need to be introduced which controls the scaling factor when shifted. Thus, we have a two dimensional minimization problem rather than the simple one dimensional minimization problem. However, by solving the new minimization parameter, it is the hope that we will be able simultaneously reconstruct the elasticity and viscosity of the medium.

Appendix

6.1 Continuous case

Let $S = [-L_x, L_x] \times [-L_y, L_y]$ be a fixed rectangular domain and $g : [-L_x - L_y, L_x + L_y] \times [-L_y, L_y] \to \mathbb{R}$. For each $\epsilon \in [-1, 1]$, define *the average variance of ϵy-translated signals* as follows:

$$\mathrm{Var}_g(\epsilon) := \frac{1}{4L_xL_y} \int_{-L_x}^{L_x} \int_{-L_y}^{L_y} \big(g(x-\epsilon y, y) - \bar{g}_\epsilon(x)\big)^2 \, dydx \quad \text{where} \quad \bar{g}_\epsilon(x) = \frac{1}{2L_y} \int_{-L_y}^{L_y} g(x-\epsilon y, y) \, dy.$$

Consider a noisy signal, $\tilde{f}(x, y) = f(x, y) + \delta(x, y)$, where $\delta(x, y) = nX(x, y)$ with a noise level $n \geq 0$. Here we assume $X(x, y) \sim U[-1, 1]$, a uniform distribution for each (x, y) and they are independent for distinct (x, y).

6.1.1 Expectation and variance of $\mathbf{Var}_{\tilde{f}}(\epsilon)$

Lemma 6.1 *For any fixed (x, y) and $\epsilon \in [-1, 1]$, the expectations are*

$$E[\delta(x-\epsilon y, y)] = 0, \quad E[\delta^2(x-\epsilon y, y)] = \frac{n^2}{3}, \quad E[\bar{\delta}_\epsilon(x)] = E[\bar{\delta}_\epsilon^2(x)] = 0, \quad E[\delta(x-\epsilon y, y) \cdot \bar{\delta}_\epsilon(x)] = 0.$$

Proof. Since $X(x, y) \sim U[-1, 1]$, we know $E[X(x, y)] = 0$ and $V[X(x, y)] = \frac{1}{3}$ for each (x, y). So we easily get $E[\delta(x - \epsilon y, y)] = nE[X(x - \epsilon y, y)] = 0$ and $V[\delta(x - \epsilon y, y)] = n^2V[X(x - \epsilon y, y)] = \frac{n^2}{3}$. Therefore

$$E[\delta^2(x-\epsilon y, y)] = V\left[\delta(x-\epsilon y, y)\right] + E[\delta(x-\epsilon y, y)]^2 = \frac{n^2}{3}.$$

For $\bar{\delta}_\epsilon$ related terms, recall the Bates distribution, $B_N = \frac{1}{N}\sum_{k=1}^{N} X_k$ where $X_k \underset{iid}{\sim} U[-1,1]$ and $E[B_N] = 0$ and $V[B_N] = \frac{1}{3N}$ [6]. Since $\bar{\delta}_\epsilon(x) = n \lim_{N\to\infty} B_N$ in the sense of a Riemann sum, using the dominated convergence theorem we get

$$E[\bar{\delta}_\epsilon(x)] = n \lim_{N\to\infty} E[B_N] = 0, \quad E[\bar{\delta}_\epsilon^2(x)] = V[\bar{\delta}_\epsilon(x)] + E[\bar{\delta}_\epsilon(x)]^2 = n^2 \lim_{N\to\infty} V[B_N] = 0.$$

For $E[\delta(x-\epsilon y, y)\cdot\bar{\delta}_\epsilon(x)] = \mathrm{Cov}[\delta(x-\epsilon y, y), \bar{\delta}_\epsilon(x)] + E[\delta(x-\epsilon y, y)]\cdot E[\bar{\delta}_\epsilon(x)] = \mathrm{Cov}[\delta(x-\epsilon y, y), \bar{\delta}_\epsilon(x)] = 0$, we use the Cauchy-Schwarz inequality [20]:

$$|\mathrm{Cov}[\delta(x-\epsilon y, y), \bar{\delta}_\epsilon(x)]|^2 \le V[\delta(x-\epsilon y, y)] \cdot V[\bar{\delta}_\epsilon(x)] = \frac{n^2}{3}\cdot 0 = 0.$$

□

Theorem 6.2 *When $\tilde{f} = f + \delta$ where $\delta \sim nU[-1,1]$, we have*

$$E[\mathrm{Var}_{\tilde{f}}(\epsilon)] = \mathrm{Var}_f(\epsilon) + \frac{n^2}{3}, \qquad V[\mathrm{Var}_{\tilde{f}}(\epsilon)] = 0.$$

Proof. Since $\mathrm{Var}_g(\epsilon)$ is quadratic in g, it is straightforward to have $\mathrm{Var}_{\tilde{f}}(\epsilon) = \mathrm{Var}_f(\epsilon) + \mathrm{Var}_\delta(\epsilon) + 2\mathrm{Cov}_{f,\delta}(\epsilon)$, where

$$\mathrm{Cov}_{f,\delta}(\epsilon) := \frac{1}{4L_xL_y}\int_{-L_x}^{L_x}\int_{-L_y}^{L_y} \big(f(x-\epsilon y, y) - \bar{f}_\epsilon(x)\big)\cdot\big(\delta(x-\epsilon y, y) - \bar{\delta}_\epsilon(x)\big)\, dydx.$$

Since $\mathrm{Var}_f(\epsilon)$ is deterministic, it suffices to show $E[\mathrm{Var}_\delta(\epsilon)] = \frac{n^2}{3}$ and $E[\mathrm{Cov}_{f,\delta}(\epsilon)] = 0$. Again, using the Riemann sum and dominated convergence theorem and then Lemma 6.1, we can show

$$E[\mathrm{Var}_\delta(\epsilon)] = \frac{1}{4L_xL_y}\int_{-L_x}^{L_x}\int_{-L_y}^{L_y} E\left[\big(\delta(x-\epsilon y, y) - \bar{\delta}_\epsilon(x)\big)^2\right] dydx = \frac{n^2}{3},$$
$$E[\mathrm{Cov}_{f,\delta}(\epsilon)] = \frac{1}{4L_xL_y}\int_{-L_x}^{L_x}\int_{-L_y}^{L_y} \big(f(x-\epsilon y, y) - \bar{f}_\epsilon(x)\big)\cdot E\left[\big(\delta(x-\epsilon y, y) - \bar{\delta}_\epsilon(x)\big)\right] dydx = 0.$$

Since $\mathrm{Var}_f(\epsilon)$ is deterministic, note that

$$\begin{aligned} V\left[\mathrm{Var}_{\tilde{f}}(\epsilon)\right] =& V\left[\mathrm{Var}_f(\epsilon) + \mathrm{Var}_\delta(\epsilon) + 2\mathrm{Cov}_{f,\delta}(\epsilon)\right] = V\left[\mathrm{Var}_\delta(\epsilon) + 2\mathrm{Cov}_{f,\delta}(\epsilon)\right] \\ =& V[\mathrm{Var}_\delta(\epsilon)] + 4V[\mathrm{Cov}_{f,\delta}(\epsilon)] + 4\mathrm{Cov}[\mathrm{Var}_\delta(\epsilon), \mathrm{Cov}_{f,\delta}(\epsilon)]. \end{aligned}$$

Again, using the Riemann sum and dominated convergence theorem, we have

$$\begin{aligned} &\mathrm{Cov}[\mathrm{Var}_\delta(\epsilon), \mathrm{Cov}_{f,\delta}(\epsilon)] \\ =&\mathrm{Cov}\left[\frac{1}{|S|}\int_S \left(\delta(x-\epsilon y, y) - \bar{\delta}_\epsilon(x)\right)^2 dydx, \frac{1}{|S|}\int_S \left(f(x-\epsilon y, y) - \bar{f}_\epsilon(x)\right)\cdot\left(\delta(x-\epsilon y, y) - \bar{\delta}_\epsilon(x)\right) dydx\right] \\ =&\frac{1}{|S|^2}\int_{S\times S} \mathrm{Cov}\left[\left(\delta(x-\epsilon y, y) - \bar{\delta}_\epsilon(x)\right)^2, \left(f(x'-\epsilon y', y') - \bar{f}_\epsilon(x')\right)\cdot\left(\delta(x'-\epsilon y', y') - \bar{\delta}_\epsilon(x')\right)\right] dydxdy'dx'. \end{aligned}$$

If $x \neq x'$, the integrand is zero from the independence. Since the case where $x = x'$ is of measure zero in $S \times S$, we may conclude $\mathrm{Cov}[\mathrm{Var}_\delta(\epsilon), \mathrm{Cov}_{f,\delta}(\epsilon)] = 0$. The proofs of $V[\mathrm{Var}_\delta(\epsilon)] = \mathrm{Cov}[\mathrm{Var}_\delta(\epsilon), \mathrm{Var}_\delta(\epsilon)] = 0$ and $V[\mathrm{Cov}_{f,\delta}(\epsilon)] = \mathrm{Cov}[\mathrm{Cov}_{f,\delta}(\epsilon), \mathrm{Cov}_{f,\delta}(\epsilon)] = 0$ are similar. □

6.2 Discrete case

We suppose g on S is discretized as follows:

$$G(i,j) := g(i\Delta x, j\Delta y), \quad i = -m, \ldots, m, \quad j = -l \ldots l,$$

which means $S = [-L_x, L_x] \times [-L_y, L_y]$ is discretized with $(2m+1) \times (2l+1)$ samples, where $L_x = m\Delta x$ and $L_y = l\Delta y$.

Since $g(i\Delta x - \epsilon j\Delta y, j\Delta y)$ is not on our grid structure if $\epsilon \neq 0, \pm 1$, we interpolate with a distance based weight; for simplicity, assume $\Delta x = \Delta y$.

$$g(i\Delta x - \epsilon j\Delta y, j\Delta y) = g((i-\epsilon j)\Delta x, j\Delta x) \approx (1-\alpha_j(\epsilon))G(i-\lfloor \epsilon j \rfloor, j) + \alpha_j(\epsilon)G(i-\lfloor \epsilon j \rfloor - 1, j) =: g_{i,j}(\epsilon)$$

where $\alpha_j(\epsilon) = \epsilon j - \lfloor \epsilon j \rfloor$. Here $\lfloor\ \rfloor$ denotes the floor function.

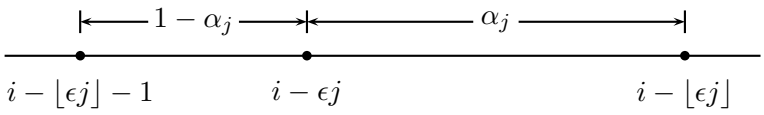

Figure 6.2: Interpolation of discrete data points to estimate the ϵj shift.

Then the discretized version of $\mathrm{Var}_g(\epsilon)$ is given by

$$var_g(\epsilon) := \frac{1}{(2m+1)(2l+1)} \sum_{i=-m}^{m} \sum_{j=-l}^{l} \left(g_{i,j}(\epsilon) - \overline{g}_i(\epsilon)\right)^2 \quad where \quad \overline{g}_i(\epsilon) = \frac{1}{2l+1} \sum_{j=-l}^{l} g_{i,j}(\epsilon). \quad (6.1)$$

Thus, following this notation, we can interpolate the discretized noisy signal,

$$\tilde{f}(x,y) = f(x,y) + \delta(x,y) \approx f_{i,j}(\epsilon) + \delta_{i,j}(\epsilon),$$

where $\delta_{i,j}(\epsilon) = nX_{i,j}(\epsilon)$. Here $n \geq 0$ is the noise level and $X_{i,j}(\epsilon)$ is the interpolated $X(x,y) \underset{iid}{\sim} U[-1,1]$ for each (x,y). Thus, we have

$$X_{i,j}(\epsilon) = (1-\alpha_j(\epsilon))X((i-\lfloor \epsilon j \rfloor)\Delta x, j\Delta x) + \alpha_j(\epsilon)X((i-\lfloor \epsilon j \rfloor - 1)\Delta x, j\Delta x) \quad (6.2)$$

and $\delta_{i,j}(\epsilon)$ and $\delta_{i',j'}(\epsilon)$ are independent if and only if $|i-i'| > 1$ or $j \neq j'$. Similarly to the continuous case, we define our variance for noisy data as

$$var_{\tilde{f}}(\epsilon) = var_f(\epsilon) + var_\delta(\epsilon) + 2cov_{f,\delta}(\epsilon),$$

where the variances follows (6.1) and the covariance is defined similarly by

$$cov_{f,\delta}(\epsilon) := \frac{1}{(2m+1)(2l+1)} \sum_{i=-m}^{m} \sum_{j=-l}^{l} \left(f_{i,j}(\epsilon) - \overline{f}_i(\epsilon)\right)\left(\delta_{i,j}(\epsilon) - \overline{\delta}_i(\epsilon)\right).$$

Remark 6.3 *For convenience, we assume the data is given even outside of S, so when the translated data is not supported by S, we use the exterior values. However, in actual simulations, we use an ϵ dependent L_x described in section 5.3.1 .*

6.2.1 Expectation

We start with the discrete version of Lemma 6.1.

Lemma 6.4 *For any fixed (i,j) and $\epsilon \in [-1,1]$, the expectations are*

$$E\left[\delta_{i,j}(\epsilon)\right] = E\left[\bar{\delta}_i(\epsilon)\right] = 0, \quad E[\delta_{i,j}(\epsilon)^2] = \frac{n^2\beta_j(\epsilon)}{3}, \quad E\left[\bar{\delta}_i(\epsilon)^2\right] = \frac{n^2\bar{\beta}(\epsilon)}{3(2l+1)}, \quad E[\delta_{i,j}(\epsilon)\cdot\bar{\delta}_i(\epsilon)] = \frac{n^2\beta_j(\epsilon)}{3(2l+1)},$$

where $\beta_j(\epsilon) = (1-\alpha_j(\epsilon))^2 + \alpha_j(\epsilon)^2 = 1 - 2\alpha_j(\epsilon) + 2\alpha_j(\epsilon)^2$ *and* $\bar{\beta}(\epsilon) = \dfrac{1}{2l+1}\displaystyle\sum_{j=-l}^{l}\beta_j(\epsilon)$.

Proof. From (6.2) and the fact that $E[X(x,y)] = 0$, it is straightforward to have $E\left[\delta_{i,j}\right] = 0$, and thus $E\left[\overline{\delta}_i\right] = 0$. Here we drop ϵ in the notations for simplicity. Again, from (6.2) and the fact that $E[X(x,y)^2] = V[X(x,y)] = \frac{1}{3}$, we easily get

$$E\left[\delta_{i,j}^2\right] = \frac{n^2}{3}[(1-\alpha_j)^2 + \alpha_j^2] = \frac{n^2\beta_j}{3}.$$

Since $\delta_{i,j}$ and $\delta_{i,j'}$ are independent when $j \neq j'$, and $E[\delta_{i,j}] = 0$, we have

$$E[\delta_{i,j}\cdot\bar{\delta}_i] = \frac{1}{2l+1}\sum_{j'=-l}^{l} E[\delta_{i,j}\cdot\delta_{i,j'}] = \frac{1}{2l+1}\left(E[\delta_{i,j}^2] + \sum_{j'\neq j} E[\delta_{i,j}]E[\delta_{i,j'}]\right) = \frac{1}{2l+1}E[\delta_{i,j}^2] = \frac{n^2\beta_j}{3(2l+1)},$$

and $E[\bar{\delta}_i^2] = \dfrac{1}{2l+1}\displaystyle\sum_{j=-l}^{l} E[\delta_{i,j}\cdot\bar{\delta}_i] = \frac{n^2\bar{\beta}}{3(2l+1)}$. □

Now we prove the discretized version of expectation in Theorem 6.2. First, note that

$$E\left[var_{\tilde{f}}(\epsilon)\right] = var_f(\epsilon) + E\left[var_\delta(\epsilon)\right] + 2E\left[cov_{f,\delta}(\epsilon)\right].$$

Theorem 6.5 *For a fixed $\epsilon \in [-1,1]$ with noise level $n \geq 0$, we have*

$$E\left[var_{\tilde{f}}(\epsilon)\right] = var_f(\epsilon) + \frac{2ln^2\bar{\beta}(\epsilon)}{3(2l+1)}.$$

Proof. From Lemma 6.4, we have

$$E\left[cov_{f,\delta}(\epsilon)\right] = \frac{1}{(2m+1)(2l+1)} \sum_{i=-m}^{m} \sum_{j=-l}^{l} \left(f_{i,j}(\epsilon) - \overline{f}_i(\epsilon)\right) \left(E[\delta_{i,j}(\epsilon)] - E[\bar{\delta}_i(\epsilon)]\right) = 0,$$

$$\begin{aligned} E\left[var_{\delta}(\epsilon)\right] &= \frac{1}{(2m+1)(2l+1)} \sum_{i=-m}^{m} \sum_{j=-l}^{l} \left(E\left[\delta_{i,j}^2\right] - 2E\left[\delta_{i,j} \cdot \bar{\delta}_i\right] + E\left[\bar{\delta}_i^2\right]\right) \\ &= \frac{1}{(2m+1)(2l+1)} \sum_{i=-m}^{m} \left((2l+1)\frac{n^2\bar{\beta}}{3} - 2\frac{n^2\bar{\beta}}{3} + \frac{n^2\bar{\beta}}{3}\right) = \frac{2ln^2\bar{\beta}}{3(2l+1)}, \end{aligned}$$

which yields the desired result. □

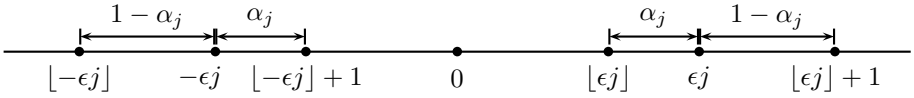

Figure 6.3: Illustration for the symmetry of $\beta_j(\epsilon)$.

Remark 6.6 *Here $\bar{\beta}$ satisfies the following properties.*

(a) *$\bar{\beta}$ is an even function on $[-1, 1]$.*

(b) *$\bar{\beta}(\epsilon) = 1 - \frac{4}{2l+1}\sum_{j=1}^{l} \alpha_j(1-\alpha_j) \in (\frac{1}{2}, 1)$ except $\epsilon = 0, \pm 1$. For $\epsilon = 0, \pm 1$, we have $\bar{\beta}(\epsilon) = 1$.*

Proof. Since $\beta_j(\epsilon)$ is the sum of the squared distance from ϵj to the nearest left and right integers (see Figure 6.3), we immediately get $\beta_j(\epsilon) = \beta_{-j}(\epsilon)$ and $\beta_j(\epsilon) = \beta_j(-\epsilon)$. For (a), $\bar{\beta}(\epsilon) = \bar{\beta}(-\epsilon)$ is obvious from the evenness of each β_j. For (b), first note that $\beta_0(\epsilon) = 1$ from $\alpha_0(\epsilon) = 0 - \lfloor 0 \rfloor = 0$. Hence

$$\bar{\beta}(\epsilon) = \frac{1}{2l+1}\left(1 + 2\sum_{j=1}^{l} \beta_j(\epsilon)\right) = \frac{1}{2l+1} + \frac{2}{2l+1}\sum_{j=1}^{l}(1 - 2\alpha_j + 2\alpha_j^2) = 1 - \frac{4}{2l+1}\sum_{j=1}^{l} \alpha_j(1-\alpha_j).$$

Since $\alpha_j \in [0, 1)$, we have $\alpha_j(1-\alpha_j) \in [0, \frac{1}{4}]$, thus $\frac{1}{2} < 1 - \frac{l}{2l+1} \le \bar{\beta} \le 1$. In order to have $\bar{\beta} = 1$, we should have $\alpha_j(\epsilon) = 0$ for all j. This occurs if and only if $\epsilon = 0, \pm 1$. □

Recalling Theorem 6.2, the factor gained from interpolation is $\frac{2l}{2l+1}\bar{\beta}(\epsilon) < 1$ in the expectation sense. In fact, for a fair comparison with continuous case given in Theorem 6.2, we have to assume infinitely many samples, $l = \infty$. Then the factor of gain will be $\lim_{l\to\infty} \bar{\beta}(\epsilon)$, which is given in the following theorem. Notice that $\lim_{l\to\infty} \bar{\beta}(\epsilon) = 1$ for $\epsilon = 0, \pm 1$, which is expected since no interpolation is taken in these cases.

Theorem 6.7 $\lim_{l\to\infty} \bar{\beta}(\epsilon)$ *is an even function on* $[-1, 1]$ *and*

$$\lim_{l\to\infty} \bar{\beta}(\epsilon) = \begin{cases} \frac{2}{3} + \frac{1}{3q^2}, & \epsilon = \frac{p}{q} \in (0,1) \cap \mathbb{Q} \text{ (in the lowest form)}, \\ 1, & \epsilon = 0 \text{ or } 1, \\ \frac{2}{3}, & \epsilon \in (0,1) \cap \mathbb{Q}^c. \end{cases}$$

Proof. Since $\bar{\beta}$ is an even function, so is the limit. For $\epsilon = 0$ or 1, we have $\bar{\beta}(\epsilon) = 1$ for all l, so its limit is also 1. Now let $\epsilon = p/q \in (0,1)$ where $p, q \in \mathbb{N}$ are relatively prime. We claim

$$\{\alpha_j(p/q) \,|\, j = 1, 2, \ldots, q\} = \{k/q \,|\, k = 0, 1, \ldots, q-1\}.$$

Since $\alpha_j(p/q) = jp/q - m = (jp - mq)/q \in [0, 1)$ and $jp - mq \in \{0, 1, \ldots, q-1\}$ where $m = \lfloor jp/q \rfloor \in \mathbb{N} \cup \{0\}$, $\alpha_j(p/q) = k/q$ for some $k \in \{0, 1, \ldots, q-1\}$. Moreover, this correspondence is one-to-one: Suppose $\alpha_j(p/q) = \alpha_{j'}(p/q)$ and we assume $j \geq j'$ without loss of generality. Then

$$\frac{(j-j')p}{q} = \left\lfloor \frac{jp}{q} \right\rfloor - \left\lfloor \frac{j'p}{q} \right\rfloor \in \mathbb{N} \cup \{0\} \quad \Rightarrow \quad j - j' \in \{0, q, 2q, \cdots\} \quad \Rightarrow \quad j = j'.$$

since p and q are relatively prime and $j, j' = 1, 2, \ldots, q$. Similarly, we can easily extend this to

$$\{\alpha_j(p/q) \,|\, j = 1 + nq, 2 + nq, \ldots, (n+1)q\} = \{k/q \,|\, k = 0, 1, \ldots, q-1\}, \quad \forall n \in \mathbb{N} \cup \{0\}. \tag{6.3}$$

Now let $l = n_l q + r_l$ where $n_l, r_l \in \mathbb{N} \cup \{0\}$ satisfying $r_l < q$. Then we have

$$\sum_{j=1}^{l} \alpha_j(1-\alpha_j) = \sum_{j=1}^{n_l q} \alpha_j(1-\alpha_j) + \sum_{j=n_l q+1}^{n_l q+r_l} \alpha_j(1-\alpha_j),$$

where the second term, I_2, is bounded as $0 \le I_2 \le \dfrac{r_l}{4} < \dfrac{q}{4}$ and the first term is further computed from (6.3) as follows:

$$\sum_{j=1}^{n_l q} \alpha_j(1-\alpha_j) = n_l \sum_{k=1}^{q-1} \frac{k}{q}\left(1-\frac{k}{q}\right) = \frac{n_l}{q^2}\sum_{k=1}^{q-1}\left(qk-k^2\right) = \frac{n_l(q^2-1)}{6q}.$$

Finally, taking the limit, we get

$$\lim_{l\to\infty} \bar{\beta}(\epsilon) = 1 - \lim_{l\to\infty} \frac{4}{2l+1}\frac{n_l(q^2-1)}{6q} - \lim_{l\to\infty}\frac{4I_2}{2l+1} = 1 - \frac{q^2-1}{6q}\lim_{l\to\infty}\frac{4n_l}{2l+1} = \frac{2q^2+1}{3q^2},$$

because $\displaystyle\lim_{l\to\infty}\frac{4n_l}{2l+1} = \lim_{l\to\infty}\frac{4(l-r_l)}{q(2l+1)} = \frac{2}{q}$.

For an irrational $\epsilon \in (0,1)$, $\{\alpha_j(\epsilon) \,|\, j = 1, 2, \ldots, l\}$ will be uniformly distributed on $(0,1)$ as $l \to \infty$. This is the consequence of Weyl's equidistribution theorem [12], thus we have

$$\lim_{l\to\infty}\bar{\beta}(\epsilon) = 1 - \lim_{l\to\infty}\left(\frac{4l}{2l+1}\right)\left(\frac{1}{l}\sum_{j=1}^{l}\alpha_j(1-\alpha_j)\right) = 1 - 2\int_0^1 t(1-t)\,dt = \frac{2}{3}.$$

□

See Figure 6.4 for the graphs of $\bar{\beta}(\epsilon)$ as l increases. Notice that all the $\bar{\beta}(\epsilon)$ are continuous functions on $[-1,1]$ with cusps at corresponding rational numbers, while $\displaystyle\lim_{l\to\infty}\bar{\beta}(\epsilon)$ is continuous at all irrational points but discontinuous at all rational points.

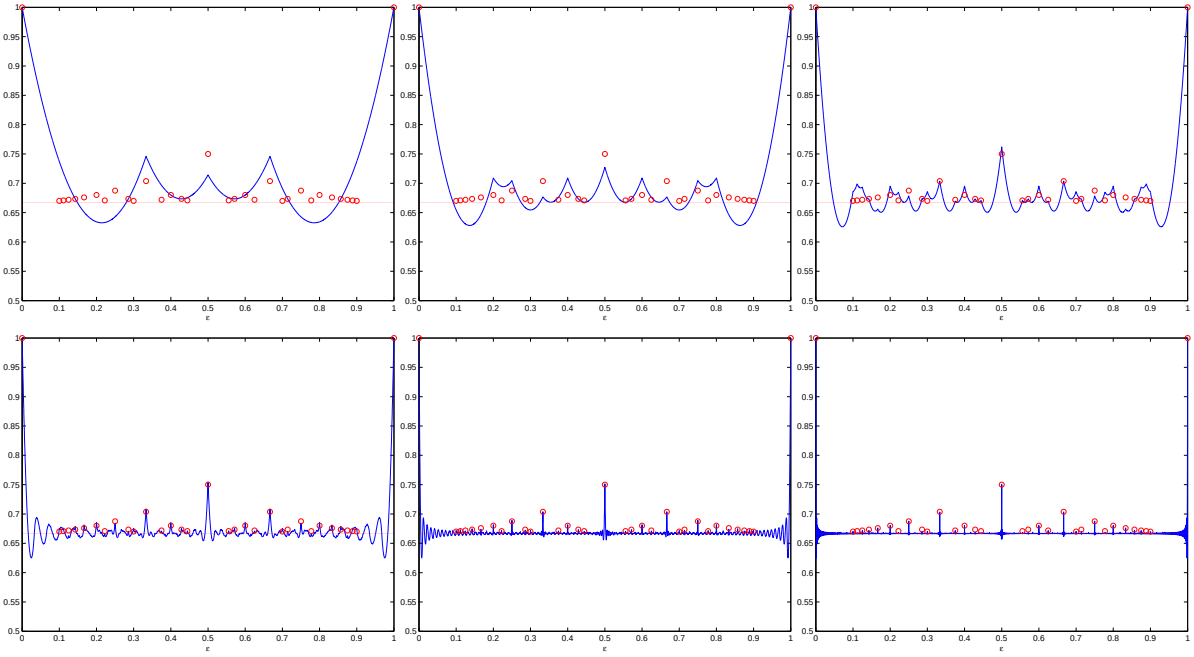

Figure 6.4: Plots of $\bar{\beta}(\epsilon)$ on $[0,1]$ with $l = 3, 5, 10, 30, 100, 500$ (from top left to the bottom right). Red line and circles denote $\lim_{l\to\infty} \bar{\beta}(\epsilon)$. For $\epsilon \in [-1, 0]$, even extensions should be applied.

6.2.2 Variance

Next we will look at the variance of $var_{\tilde{f}}(\epsilon)$. For convenience, define

$$g_{i,j}(\epsilon) := (\delta_{i,j}(\epsilon) - \overline{\delta}_i(\epsilon))^2 + 2(f_{i,j}(\epsilon) - \overline{f}_i(\epsilon))(\delta_{i,j}(\epsilon) - \overline{\delta}_i(\epsilon)).$$

Then $var_{\tilde{f}}(\epsilon)$ can be rewritten as

$$var_{\tilde{f}}(\epsilon) = var_f(\epsilon) + \frac{1}{(2l+1)(2m+1)} \sum_{i=-m}^{m} \sum_{j=-l}^{l} g_{i,j}(\epsilon).$$

Since $var_f(\epsilon)$ is deterministic, we get

$$V\left[var_{\tilde{f}}(\epsilon)\right] = \frac{1}{(2l+1)^2(2m+1)^2} \sum_{i=-m}^{m} \sum_{i'=-m}^{m} \sum_{j=-l}^{l} \sum_{j'=-l}^{l} Cov\left[g_{i,j}(\epsilon), g_{i',j'}(\epsilon)\right].$$

Lemma 6.8 *For fixed ϵ, i, i', j, j', we have*

$$Cov[g_{i,j}, g_{i',j'}] = Cov\left[(\delta_{i,j} - \overline{\delta}_i)^2, (\delta_{i',j'} - \overline{\delta}_{i'})^2\right] + 4(f_{i,j} - \overline{f}_i)(f_{i',j'} - \overline{f}_{i'})Cov\left[\delta_{i,j} - \overline{\delta}_i, \delta_{i',j'} - \overline{\delta}_{i'}\right].$$

Proof. Since the covariance operator is symmetric and bilinear, we have

$$\begin{aligned} Cov[g_{i,j}, g_{i',j'}] = Cov\left[(\delta_{i,j} - \overline{\delta}_i)^2, (\delta_{i',j'} - \overline{\delta}_{i'})^2\right] + 4(f_{i,j} - \overline{f}_i)(f_{i',j'} - \overline{f}_{i'})Cov\left[\delta_{i,j} - \overline{\delta}_i, \delta_{i',j'} - \overline{\delta}_{i'}\right] \\ +2(f_{i',j'} - \overline{f}_{i'})Cov\left[(\delta_{i,j} - \overline{\delta}_i)^2, \delta_{i',j'} - \overline{\delta}_{i'}\right] + 2(f_{i,j} - \overline{f}_i)Cov\left[(\delta_{i',j'} - \overline{\delta}_{i'})^2, \delta_{i,j} - \overline{\delta}_i\right]. \end{aligned}$$

So it suffices to show $Cov\left[(\delta_{i,j} - \overline{\delta}_i)^2, \delta_{i',j'} - \overline{\delta}_{i'}\right] = 0$ for all i, i', j, j'. By the definition of covariance and the fact that $E[\delta_{i',j'}] = E[\overline{\delta}_{i'}] = 0$ from Lemma 6.4, we have

$$\begin{aligned} Cov\left[(\delta_{i,j} - \overline{\delta}_i)^2, \delta_{i',j'} - \overline{\delta}_{i'}\right] &= E[(\delta_{i,j} - \overline{\delta}_i)^2(\delta_{i',j'} - \overline{\delta}_{i'})] - E[(\delta_{i,j} - \overline{\delta}_i)^2] \cdot E[\delta_{i',j'} - \overline{\delta}_{i'}] \\ &= E[(\delta_{i,j} - \overline{\delta}_i)^2(\delta_{i',j'} - \overline{\delta}_{i'})]. \end{aligned}$$

Using the linearity of expectation after expanding $\overline{\delta}_i$ and $\overline{\delta}_{i'}$, we notice that $E[(\delta_{i,j} - \overline{\delta}_i)^2(\delta_{i',j'} - \overline{\delta}_{i'})]$ is represented by a linear combination of $E[\delta_{i,k}\delta_{i,\tilde{k}}\delta_{i',k'}]$, which is claimed to be zero. First note that if $k, \tilde{k}, k'$ are not identical, by the independence and Lemma 6.4, it is obviously zero. So we may assume $k = \tilde{k} = k'$. Also, if $|i - i'| > 1$, again by the independence, it is obviously zero. Thus the only nontrivial cases are $E[\delta_{i,k}^3]$ and $E[\delta_{i,k}^2\delta_{i\pm1,k}]$.

Recall $\delta_{i,j} = nX_{i,j} = n(1 - \alpha_j)X^{i,j} + n\alpha_j X^{i-1,j}$, where $X^{i,k} := X((i - \lfloor \epsilon k \rfloor)\Delta x, j\Delta x) \underset{iid}{\sim} U[-1, 1]$ for each (i, k) and note that $E[X^{i,k}] = E[(X^{i,k})^3] = 0$ and $E[(X^{i,k})^2] = \frac{1}{3}$. Therefore, we

get

$$
\begin{aligned}
E[\delta_{i,k}^3] =& n^3\big((1-\alpha_k)^3E[(X^{i,k})^3] + \alpha_k^3E[(X^{i-1,k})^3] \\
&+ 3(1-\alpha_k)^2\alpha_kE[(X^{i,k})^2]\cdot E[X^{i-1,k}] + 3\alpha_k^2(1-\alpha_k)E[(X^{i-1,k})^2]\cdot E[X^{i,k}]\big) = 0, \\
E[\delta_{i,k}^2\delta_{i+1,k}] =& n^3\big((1-\alpha_k)^3E[(X^{i,k})^2]\cdot E[X^{i+1,k}] + \alpha_k^2(1-\alpha_k)E[(X^{i-1,k})^2]\cdot E[X^{i+1,k}] \\
&+ \alpha_k^3E[(X^{i-1,k})^2]\cdot E[X^{i,k}] + (1-\alpha_k)^2\alpha_kE[(X^{i,k})^3] \\
&+ 2(1-\alpha_k)^2\alpha_kE[X^{i+1,k}]\cdot E[X^{i,k}]\cdot E[X^{i-1,k}] + 2\alpha_k^2(1-\alpha_k)E[(X^{i,k})^2]\cdot E[X^{i-1,k}]\big) = 0.
\end{aligned}
$$

Similarly, $E[\delta_{i,k}^2\delta_{i-1,k}] = 0$. This completes the proof. □

In order to simplify $V\left[var_{\hat{f}}(\epsilon)\right]$, we will first investigate $\sum_{j=-l}^{l}\sum_{j'=-l}^{l} Cov\left((\delta_{i,j}-\overline{\delta}_i)^2, (\delta_{i',j'}-\overline{\delta}_{i'})^2\right)$. Note that

$$
\begin{aligned}
Cov\left((\delta_{i,j}-\overline{\delta}_i)^2, (\delta_{i',j'}-\overline{\delta}_{i'})^2\right) =& Cov(\delta_{i,j}^2, \delta_{i',j'}^2) - 2Cov(\delta_{i,j}^2, \delta_{i',j'}\overline{\delta}_{i'}) + Cov(\delta_{i,j}^2, \overline{\delta}_{i'}^2) \\
&- 2\left(Cov(\delta_{i,j}\overline{\delta}_i, \delta_{i',j'}^2) - 2Cov(\delta_{i,j}\overline{\delta}_i, \delta_{i',j'}\overline{\delta}_{i'}) + Cov(\delta_{i,j}\overline{\delta}_i, \overline{\delta}_{i'}^2)\right) \\
&+ Cov(\overline{\delta}_i^2, \delta_{i',j'}^2) - 2Cov(\overline{\delta}_i^2, \delta_{i',j'}\overline{\delta}_{i'}) + Cov(\overline{\delta}_i^2, \overline{\delta}_{i'}^2).
\end{aligned}
$$

Thus, the following lemma will be helpful.

Lemma 6.9 $Cov(\delta_{i,j}\delta_{i,k}, \delta_{i',j'}\delta_{i',k'}) =$

$$
\begin{cases}
E(\delta_{i,j}^2\delta_{i',j}^2) - E(\delta_{i,j}^2)^2 & \text{if } j = k = j' = k' \\
E(\delta_{i,j}\delta_{i',j})E(\delta_{i,j'}\delta_{i',j'}) & \text{if } k = j',\ k' = j,\ j' \neq j \\
E(\delta_{i,j}\delta_{i',j})E(\delta_{i,k}\delta_{i',k}) & \text{if } j' = j,\ k' = k,\ k \neq j \\
0 & o/w
\end{cases}
$$

Proof. This proof just utilizes the definition of covariance and the independence of $\delta_{i,j}$. □

Using the above lemma, we can rewrite $Cov\left((\delta_{i,j}-\overline{\delta}_i)^2,(\delta_{i',j'}-\overline{\delta}_{i'})^2\right)$ in terms of $Cov(\delta_{i,j}\delta_{i,k},\delta_{i',j'}\delta_{i',k'})$.

Lemma 6.10 *For fixed ϵ, i, i', j, j', we have*

$$\begin{aligned}Cov\left((\delta_{i,j}-\overline{\delta}_i)^2,(\delta_{i',j'}-\overline{\delta}_{i'})^2\right) &= Cov(\delta_{i,j}^2,\delta_{i',j'}^2)-2Cov(\delta_{i,j}^2,\delta_{i',j'}\overline{\delta}_{i'})-2Cov(\delta_{i,j}\overline{\delta}_i,\delta_{i',j'}^2)+4Cov(\delta_{i,j}\overline{\delta}_i,\delta_{i',j'}\overline{\delta}_{i'})\\ &+\frac{2l+3}{(2l+1)^3}\left(Cov(\delta_{i,j}^2,\delta_{i',j}^2)+Cov(\delta_{i,j'}^2,\delta_{i',j'}^2)\right)+Cov(\overline{\delta}_i^2,\overline{\delta}_{i'}^2)\\ &-\frac{4}{(2l+1)^3}\left(\sum_{k=-l}^{l}Cov(\delta_{i,j}\delta_{i,k},\delta_{i',j}\delta_{i',k})+\sum_{k=-l}^{l}Cov(\delta_{i,j'}\delta_{i,k},\delta_{i',j'}\delta_{i',k})\right)\end{aligned}$$

Proof. First note that $Cov(\delta_{i,j}\overline{\delta}_i,\delta_{i',j'}\overline{\delta}_{i'})=\begin{cases}\frac{1}{(2l+1)^2}\sum_{k=-l}^{l}Cov(\delta_{i,j}\delta_{i,k},\delta_{i',j}\delta_{i',k}) & \text{if } j'=j\\ \frac{1}{(2l+1)^2}Cov(\delta_{i,j}\delta_{i,j'},\delta_{i',j'}\delta_{i',j}) & \text{if } j'\neq j\end{cases}$

$$Cov(\delta_{i,j}\overline{\delta}_i,\delta_{i',j'}^2)=\begin{cases}\frac{1}{2l+1}Cov(\delta_{i,j}^2,\delta_{i',j}^2) & \text{if } j'=j\\ 0 & \text{o/w}\end{cases}$$

$$Cov(\delta_{i,j}\delta_{i,k},\overline{\delta}_{i'}^2)=\begin{cases}\frac{1}{(2l+1)^2}Cov(\delta_{i,j}^2,\delta_{i',j}^2) & \text{if } k=j\\ \frac{2}{(2l+1)^2}Cov(\delta_{i,j}\delta_{i,k},\delta_{i',j}\delta_{i',k}) & \text{if } k\neq j\end{cases}$$

$$Cov(\overline{\delta}_i^2,\overline{\delta}_{i'}^2)=\frac{1}{(2l+1)^4}\sum_{j=-l}^{l}\left(2\sum_{k=-l}^{l}Cov(\delta_{i,j}\delta_{i,k},\delta_{i',j}\delta_{i',k})-Cov(\delta_{i,j}^2,\delta_{i',j}^2)\right)$$

$$Cov(\delta_{i,j}\overline{\delta}_i,\overline{\delta}_{i'}^2)=\frac{1}{(2l+1)^3}\left(2\sum_{k=-l}^{l}Cov(\delta_{i,j}\delta_{i,k},\delta_{i',j}\delta_{i',k})-Cov(\delta_{i,j}^2,\delta_{i',j}^2)\right)$$

The proof of all of these are very similar, but we will demonstrate how to prove the cases

for $Cov(\delta_{i,j}\delta_{i,k}, \overline{\delta}^2_{i'})$ as an example.

$$
\begin{aligned}
Cov(\delta_{i,j}\delta_{i,k}, \overline{\delta}^2_{i'}) &= \frac{1}{2l+1}\sum_{j'=-l}^{l} Cov(\delta_{i,j}\delta_{i,k}, \delta_{i',j'}\overline{\delta}_{i'}) = \frac{1}{(2l+1)^2}\sum_{j'=-l}^{j}\sum_{k'=-l}^{l} Cov(\delta_{i,j}\delta_{i,k}, \delta_{i',j'}\delta_{i',k'}) \\
&= \begin{cases} \dfrac{1}{(2l+1)^2}\displaystyle\sum_{j'=-l}^{j}\sum_{k'=-l}^{l} Cov(\delta^2_{i,j}, \delta_{i',j'}\delta_{i',k'}) & \text{if } k = j \\ \dfrac{1}{(2l+1)^2}\displaystyle\sum_{j'=-l}^{j}\sum_{k'=-l}^{l} Cov(\delta_{i,j}\delta_{i,k}, \delta_{i',j'}\delta_{i',k'}) & \text{if } k \neq j \end{cases} \\
&= \begin{cases} \dfrac{1}{(2l+1)^2}\displaystyle\sum_{j'=-l}^{j} Cov(\delta^2_{i,j}, \delta^2_{i',j'}) & \text{if } k = j \\ \dfrac{1}{(2l+1)^2}\displaystyle\sum_{j'=-l}^{j} \big(Cov(\delta_{i,j}\delta_{i,k}, \delta_{i',j'}\delta_{i',k}) + Cov(\delta_{i,j}\delta_{i,k}, \delta_{i',j'}\delta_{i',j})\big) & \text{if } k \neq j \end{cases} \\
&= \begin{cases} \dfrac{1}{(2l+1)^2} Cov(\delta^2_{i,j}, \delta^2_{i',j}) & \text{if } k = j \\ \dfrac{1}{(2l+1)^2}\left(Cov(\delta_{i,j}\delta_{i,k}, \delta_{i',j}\delta_{i',k}) + Cov(\delta_{i,j}\delta_{i,k}, \delta_{i',k}\delta_{i',j})\right) & \text{if } k \neq j \end{cases} \\
&= \begin{cases} \dfrac{1}{(2l+1)^2} Cov(\delta^2_{i,j}, \delta^2_{i',j}) & \text{if } k = j \\ \dfrac{2}{(2l+1)^2} Cov(\delta_{i,j}\delta_{i,k}, \delta_{i',j}\delta_{i',k}) & \text{if } k \neq j \end{cases}
\end{aligned}
$$

Now we can simplify $Cov\left((\delta_{i,j} - \overline{\delta}_i)^2, (\delta_{i',j'} - \overline{\delta}_{i'})^2\right)$.

$$
\begin{aligned}
Cov\left((\delta_{i,j}-\overline{\delta}_i)^2,(\delta_{i',j'}-\overline{\delta}_{i'})^2\right) &= Cov(\delta_{i,j}^2,\delta_{i',j'}^2) - 2Cov(\delta_{i,j}^2,\delta_{i',j'}\overline{\delta}_{i'}) + Cov(\delta_{i,j}^2,\overline{\delta}_{i'}^2) \\
&\quad - 2\left(Cov(\delta_{i,j}\overline{\delta}_i,\delta_{i',j'}^2) - 2Cov(\delta_{i,j}\overline{\delta}_i,\delta_{i',j'}\overline{\delta}_{i'}) + Cov(\delta_{i,j}\overline{\delta}_i,\overline{\delta}_{i'}^2)\right) \\
&\quad + Cov(\overline{\delta}_i^2,\delta_{i',j'}^2) - 2Cov(\overline{\delta}_i^2,\delta_{i',j'}\overline{\delta}_{i'}) + Cov(\overline{\delta}_i^2,\overline{\delta}_{i'}^2) \\
&= Cov(\delta_{i,j}^2,\delta_{i',j'}^2) - 2Cov(\delta_{i,j}^2,\delta_{i',j'}\overline{\delta}_{i'}) + \frac{1}{(2l+1)^2}Cov(\delta_{i,j}^2,\delta_{i',j}^2) \\
&\quad - 2\left(Cov(\delta_{i,j}\overline{\delta}_i,\delta_{i',j'}^2) - 2Cov(\delta_{i,j}\overline{\delta}_i,\delta_{i',j'}\overline{\delta}_{i'}) - \frac{1}{(2l+1)^3}Cov(\delta_{i,j}^2,\delta_{i',j}^2)\right. \\
&\quad \left. + \frac{2}{(2l+1)^3}\sum_{k=-l}^{l}Cov(\delta_{i,j}\delta_{i,k},\delta_{i',j}\delta_{i',k})\right) + \frac{1}{(2l+1)^2}Cov(\delta_{i,j'}^2,\delta_{i',j'}^2) \\
&\quad + \frac{2}{(2l+1)^3}Cov(\delta_{i,j'}^2,\delta_{i',j'}^2) - \frac{4}{(2l+1)^3}\sum_{k=-l}^{l}Cov(\delta_{i,j'}\delta_{i,k},\delta_{i',j'}\delta_{i',k}) \\
&\quad + Cov(\overline{\delta}_i^2,\overline{\delta}_{i'}^2) \\
&= Cov(\delta_{i,j}^2,\delta_{i',j'}^2) - 2Cov(\delta_{i,j}^2,\delta_{i',j'}\overline{\delta}_{i'}) - 2Cov(\delta_{i,j}\overline{\delta}_i,\delta_{i',j'}^2) + 4Cov(\delta_{i,j}\overline{\delta}_i,\delta_{i',j'}\overline{\delta}_{i'}) \\
&\quad + \frac{2l+3}{(2l+1)^3}\left(Cov(\delta_{i,j}^2,\delta_{i',j}^2) + Cov(\delta_{i,j'}^2,\delta_{i',j'}^2)\right) + Cov(\overline{\delta}_i^2,\overline{\delta}_{i'}^2) \\
&\quad - \frac{4}{(2l+1)^3}\left(\sum_{k=-l}^{l}Cov(\delta_{i,j}\delta_{i,k},\delta_{i',j}\delta_{i',k}) + \sum_{k=-l}^{l}Cov(\delta_{i,j'}\delta_{i,k},\delta_{i',j'}\delta_{i',k})\right)
\end{aligned}
$$

□

Lemma 6.11 *For fixed ϵ, i, i', j, we have*

$$\sum_{j'=-l}^{l} Cov\left((\delta_{i,j}-\overline{\delta}_i)^2,(\delta_{i',j'}-\overline{\delta}_{i'})^2\right) = \frac{2l(l^2-5)}{(2l+1)^3}Cov(\delta_{i,j}^2,\delta_{i',j}^2) + (2l+1)Cov(\overline{\delta}_i^2,\overline{\delta}_{i'}^2)$$
$$+\sum_{j'=-l}^{l}\left(\frac{4}{(2l+1)^2}Cov(\delta_{i,j}\delta_{i,j'},\delta_{i',j'}\delta_{i',j}) + \frac{2l-1}{(2l+1)^3}Cov(\delta_{i,j'}^2,\delta_{i',j'}^2)\right.$$
$$\left.-\frac{4}{(2l+1)^3}\sum_{k=-l}^{l}Cov(\delta_{i,j'}\delta_{i,k},\delta_{i',j'}\delta_{i',k})\right)$$

Proof. **Case 1:** $j' = j$

$$Cov\left((\delta_{i,j}-\overline{\delta}_i)^2,(\delta_{i',j}-\overline{\delta}_{i'})^2\right) = \left(1+\frac{2(2l+3)}{(2l+1)^3}\right)Cov(\delta_{i,j}^2,\delta_{i',j}^2) - 2Cov(\delta_{i,j}^2,\delta_{i',j}\overline{\delta}_{i'}) - 2Cov(\delta_{i,j}\overline{\delta}_i,\delta_{i',j}^2)$$
$$+4Cov(\delta_{i,j}\overline{\delta}_i,\delta_{i',j}\overline{\delta}_{i'}) - \frac{8}{(2l+1)^3}\sum_{k=-l}^{l}Cov(\delta_{i,j}\delta_{i,k},\delta_{i',j}\delta_{i',k}) + Cov(\overline{\delta}_i^2,\overline{\delta}_{i'}^2)$$
$$= \left(1+\frac{2(2l+3)}{(2l+1)^3}-\frac{4}{2l+1}\right)Cov(\delta_{i,j}^2,\delta_{i',j}^2) + Cov(\overline{\delta}_i^2,\overline{\delta}_{i'}^2)$$
$$+\left(\frac{4}{(2l+1)^2}-\frac{8}{(2l+1)^3}\right)\sum_{k=-l}^{l}Cov(\delta_{i,j}\delta_{i,k},\delta_{i',j}\delta_{i',k})$$
$$= \frac{(2l-1)(4l^2-3)}{(2l+1)^3}Cov(\delta_{i,j}^2,\delta_{i',j}^2) + Cov(\overline{\delta}_i^2,\overline{\delta}_{i'}^2)$$
$$+\frac{4(2l-1)}{(2l+1)^3}\sum_{k=-l}^{l}Cov(\delta_{i,j}\delta_{i,k},\delta_{i',j}\delta_{i',k})$$

Case 2: $j' \neq j$

$$Cov\left((\delta_{i,j}-\overline{\delta}_i)^2,(\delta_{i',j'}-\overline{\delta}_{i'})^2\right) = \frac{4}{(2l+1)^2}Cov(\delta_{i,j}\delta_{i,j'},\delta_{i',j'}\delta_{i',j}) + \frac{2l+3}{(2l+1)^3}\left(Cov(\delta_{i,j}^2,\delta_{i',j}^2)+Cov(\delta_{i,j'}^2,\delta_{i',j'}^2)\right)$$
$$- \frac{4}{(2l+1)^3}\left(\sum_{k=-l}^{l}Cov(\delta_{i,j}\delta_{i,k},\delta_{i',j}\delta_{i',k}) + \sum_{k=-l}^{l}Cov(\delta_{i,j'}\delta_{i,k},\delta_{i',j'}\delta_{i',k})\right)$$
$$+ Cov(\overline{\delta}_i^2,\overline{\delta}_{i'}^2)$$

$$
\begin{aligned}
\sum_{j'=-l}^{l} Cov\left((\delta_{i,j}-\overline{\delta}_i)^2,(\delta_{i',j'}-\overline{\delta}_{i'})^2\right) &= \frac{(2l-1)(4l^2-3)}{(2l+1)^3}Cov(\delta_{i,j}^2,\delta_{i',j}^2)+\frac{4(2l-1)}{(2l+1)^3}\sum_{k=-l}^{l}Cov(\delta_{i,j}\delta_{i,k},\delta_{i',j}\delta_{i',k}) \\
&\quad + 2l\left(\frac{2l+3}{(2l+1)^3}Cov(\delta_{i,j}^2,\delta_{i',j}^2)-\frac{4}{(2l+1)^3}\sum_{k=-l}^{l}Cov(\delta_{i,j}\delta_{i,k},\delta_{i',j}\delta_{i',k})\right) \\
&\quad + \sum_{\substack{j'\neq j\\ j'=-l}}^{l}\left(\frac{4}{(2l+1)^2}Cov(\delta_{i,j}\delta_{i,j'},\delta_{i',j'}\delta_{i',j})+\frac{2l+3}{(2l+1)^3}Cov(\delta_{i,j'}^2,\delta_{i',j'}^2)\right. \\
&\quad \left. -\frac{4}{(2l+1)^3}\sum_{k=-l}^{l}Cov(\delta_{i,j'}\delta_{i,k},\delta_{i',j'}\delta_{i',k})\right)+(2l+1)Cov(\overline{\delta}_i^2,\overline{\delta}_{i'}^2) \\
&= \frac{8l^3+3}{(2l+1)^3}Cov(\delta_{i,j}^2,\delta_{i',j}^2)-\frac{4}{(2l+1)^3}\sum_{k=-l}^{l}Cov(\delta_{i,j}\delta_{i,k},\delta_{i',j}\delta_{i',k}) \\
&\quad + \sum_{j'=-l}^{l}\left(\frac{4}{(2l+1)^2}Cov(\delta_{i,j}\delta_{i,j'},\delta_{i',j'}\delta_{i',j})+\frac{2l+3}{(2l+1)^3}Cov(\delta_{i,j'}^2,\delta_{i',j'}^2)\right. \\
&\quad \left. -\frac{4}{(2l+1)^3}\sum_{k=-l}^{l}Cov(\delta_{i,j'}\delta_{i,k},\delta_{i',j'}\delta_{i',k})\right)+(2l+1)Cov(\overline{\delta}_i^2,\overline{\delta}_{i'}^2) \\
&\quad - \frac{10l+7}{(2l+1)^3}Cov(\delta_{i,j}^2,\delta_{i',j}^2)+\frac{4}{(2l+1)^3}\sum_{k=-l}^{l}Cov(\delta_{i,j}\delta_{i,k},\delta_{i',j}\delta_{i',k}) \\
&= \frac{2(2l^2-l-2)}{(2l+1)^2}Cov(\delta_{i,j}^2,\delta_{i',j}^2)+(2l+1)Cov(\overline{\delta}_i^2,\overline{\delta}_{i'}^2) \\
&\quad + \sum_{j'=-l}^{l}\left(\frac{4}{(2l+1)^2}Cov(\delta_{i,j}\delta_{i,j'},\delta_{i',j'}\delta_{i',j})+\frac{2l+3}{(2l+1)^3}Cov(\delta_{i,j'}^2,\delta_{i',j'}^2)\right. \\
&\quad \left. -\frac{4}{(2l+1)^3}\sum_{k=-l}^{l}Cov(\delta_{i,j'}\delta_{i,k},\delta_{i',j'}\delta_{i',k})\right)
\end{aligned}
$$

□

Lemma 6.12 *For fixed ϵ, i, i', we have*

$$\sum_{j=-l}^{l}\sum_{j'=-l}^{l} Cov\left((\delta_{i,j}-\overline{\delta}_i)^2,(\delta_{i',j'}-\overline{\delta}_{i'})^2\right)=\frac{2}{(2l+1)^2}\sum_{j=-l}^{l}\left((2l^2-1)Cov(\delta_{i,j}^2,\delta_{i',j}^2)+\sum_{k=-l}^{l}Cov(\delta_{i,j}\delta_{i,k},\delta_{i',j}\delta_{i',k})\right)$$

Proof.

$$\begin{aligned}\sum_{j=-l}^{l}\sum_{j'=-l}^{l} Cov\left((\delta_{i,j}-\overline{\delta}_i)^2,(\delta_{i',j'}-\overline{\delta}_{i'})^2\right)&=\frac{2(2l^2-l-2)}{(2l+1)^2}\sum_{j=-l}^{l}Cov(\delta_{i,j}^2,\delta_{i',j}^2)+(2l+1)^2Cov(\overline{\delta}_i^2,\overline{\delta}_{i'}^2)\\&\quad+\frac{4}{(2l+1)^2}\sum_{j=-l}^{l}\sum_{j'=-l}^{l}Cov(\delta_{i,j}\delta_{i,j'},\delta_{i',j'}\delta_{i',j})\\&\quad+\frac{2l+3}{(2l+1)^2}\sum_{j'=-l}^{l}Cov(\delta_{i,j'}^2,\delta_{i',j'}^2)\\&\quad-\frac{4}{(2l+1)^2}\sum_{j'=-l}^{l}\sum_{k=-l}^{l}Cov(\delta_{i,j'}\delta_{i,k},\delta_{i',j'}\delta_{i',k})\\&=\frac{2l-1}{2l+1}\sum_{j=-l}^{l}Cov(\delta_{i,j}^2,\delta_{i',j}^2)+(2l+1)^2Cov(\overline{\delta}_i^2,\overline{\delta}_{i'}^2)\\&=\frac{2}{(2l+1)^2}\sum_{j=-l}^{l}\left((2l^2-1)Cov(\delta_{i,j}^2,\delta_{i',j}^2)+\sum_{k=-l}^{l}Cov(\delta_{i,j}\delta_{i,k},\delta_{i',j}\delta_{i',k})\right)\end{aligned}$$

□

It is quite straightforward to calculate $Cov\left(\delta_{i,j}-\overline{\delta}_i,\delta_{i',j'}-\overline{\delta}_{i'}\right)$, but instead we calculate
$\sum_{j'=-l}^{l}\sum_{j=-l}^{l}(f_{i',j'}-\overline{f}_{i'})(f_{i,j}-\overline{f}_i)Cov(\delta_{i,j}-\overline{\delta}_i,\delta_{i',j'}-\overline{\delta}_{i'})$.

Lemma 6.13

$$\sum_{j'=-l}^{l}\sum_{j=-l}^{l}(f_{i',j'}-\overline{f}_{i'})(f_{i,j}-\overline{f}_i)Cov(\delta_{i,j}-\overline{\delta}_i,\delta_{i',j'}-\overline{\delta}_{i'})=\sum_{j'=-l}^{l}(f_{i',j'}-\overline{f}_{i'})(f_{i,j'}-\overline{f}_i)Cov(\delta_{i,j},\delta_{i',j'})$$

Proof.

$$
\begin{aligned}
&\sum_{j'=-l}^{l}\sum_{j=-l}^{l}(f_{i',j'}-\overline{f}_{i'})(f_{i,j}-\overline{f}_{i})Cov(\delta_{i,j}-\overline{\delta}_i,\delta_{i',j'}-\overline{\delta}_{i'})\\
&\quad=\sum_{j'=-l}^{l}(f_{i',j'}-\overline{f}_{i'})\left[\left(\sum_{j=-l}^{l}f_{i,j}\left(Cov(\delta_{i,j},\delta_{i',j'})-Cov(\delta_{i,j},\overline{\delta}_{i'})-Cov(\delta_{i',j'},\overline{\delta}_i)+Cov(\overline{\delta}_i,\overline{\delta}_{i'})\right)\right)\right.\\
&\quad\left.-\overline{f}_i\left(\sum_{j=-l}^{l}\left(Cov(\delta_{i,j},\delta_{i',j'})-Cov(\delta_{i,j},\overline{\delta}_{i'})-Cov(\delta_{i',j'},\overline{\delta}_i)+Cov(\overline{\delta}_i,\overline{\delta}_{i'})\right)\right)\right]\\
&\quad=\sum_{j'=-l}^{l}(f_{i',j'}-\overline{f}_{i'})\left[f_{i,j'}Cov(\delta_{i,j'},\delta_{i',j'})-\left(\sum_{j=-l}^{l}f_{i,j}Cov(\delta_{i,j},\overline{\delta}_{i'})\right)\right.\\
&\quad+(2l+1)\left(Cov(\overline{\delta}_i,\overline{\delta}_{i'})-Cov(\delta_{i',j'},\overline{\delta}_i)\right)\overline{f}_i\\
&\quad\left.-\overline{f}_i\left(Cov(\delta_{i,j'},\delta_{i',j'})-\left(\sum_{j=-l}^{l}Cov(\delta_{i,j},\overline{\delta}_{i'})\right)+(2l+1)\left(Cov(\overline{\delta}_i,\overline{\delta}_{i'})-Cov(\delta_{i',j'},\overline{\delta}_i)\right)\right)\right]\\
&\quad=\sum_{j'=-l}^{l}(f_{i',j'}-\overline{f}_{i'})\left[(f_{i,j'}-\overline{f}_i)Cov(\delta_{i,j'},\delta_{i',j'})-\left(\sum_{j=-l}^{l}(f_{i,j}-\overline{f}_i)Cov(\delta_{i,j},\overline{\delta}_{i'})\right)\right]\\
&\quad=\left(\sum_{j'=-l}^{l}(f_{i',j'}-\overline{f}_{i'})(f_{i,j'}-\overline{f}_i)Cov(\delta_{i,j'},\delta_{i',j'})\right)-\left(\sum_{j'=-l}^{l}f_{i',j'}\left(\sum_{j=-l}^{l}(f_{i,j}-\overline{f}_i)Cov(\delta_{i,j},\overline{\delta}_{i'})\right)\right)\\
&\quad+\left(\sum_{j'=-l}^{l}\overline{f}_{i'}\left(\sum_{j=-l}^{l}(f_{i,j}-\overline{f}_i)Cov(\delta_{i,j},\overline{\delta}_{i'})\right)\right)\\
&\quad=\left(\sum_{j'=-l}^{l}(f_{i',j'}-\overline{f}_{i'})(f_{i,j'}-\overline{f}_i)Cov(\delta_{i,j'},\delta_{i',j'})\right)-\left(\sum_{j'=-l}^{l}f_{i',j'}\right)\left(\sum_{j=-l}^{l}(f_{i,j}-\overline{f}_i)Cov(\delta_{i,j},\overline{\delta}_{i'})\right)\\
&\quad+(2l+1)\overline{f}_{i'}\left(\sum_{j=-l}^{l}(f_{i,j}-\overline{f}_i)Cov(\delta_{i,j},\overline{\delta}_{i'})\right)\\
&\quad=\sum_{j'=-l}^{l}(f_{i',j'}-\overline{f}_{i'})(f_{i,j'}-\overline{f}_i)Cov(\delta_{i,j'},\delta_{i',j'})
\end{aligned}
$$

□

Now we can combine the two pieces.

Lemma 6.14

$$\sum_{j=-l}^{l}\sum_{j'=-l}^{l} Cov(g_{i,j}, g_{i',j'}) = \sum_{j=-l}^{l}\Bigg(\frac{4l^2}{(2l+1)^2}\left(E(\delta_{i,j}^2\delta_{i',j}^2) - E(\delta_{i,j}^2)^2\right) - \frac{2}{(2l+1)^2}E(\delta_{i,j}\delta_{i',j})^2$$
$$+4(f_{i',j}-\overline{f}_{i'})(f_{i,j}-\overline{f}_{i})E(\delta_{i,j}\delta_{i',j})\Big) + \frac{2}{(2l+1)^2}\left(\sum_{k=-l}^{l}E(\delta_{i,k}\delta_{i',k})\right)^2$$

Proof.

$$\sum_{j=-l}^{l}\sum_{j'=-l}^{l} Cov(g_{i,j}, g_{i',j'}) = \sum_{j=-l}^{l}\sum_{j'=-l}^{l}\Big(Cov\left((\delta_{i,j}-\overline{\delta}_i)^2, (\delta_{i',j'}-\overline{\delta}_{i'})^2\right)$$
$$+4(f_{i,j}-\overline{f}_i)(f_{i',j'}-\overline{f}_{i'})Cov\left(\delta_{i,j}-\overline{\delta}_i, \delta_{i',j'}-\overline{\delta}_{i'}\right)\Big)$$
$$= \frac{2}{(2l+1)^2}\sum_{j=-l}^{l}\left((2l^2-1)Cov(\delta_{i,j}^2,\delta_{i',j}^2) + \sum_{k=-l}^{l}Cov(\delta_{i,j}\delta_{i,k},\delta_{i',j}\delta_{i',k})\right)$$
$$+4\sum_{j'=-l}^{l}(f_{i',j'}-\overline{f}_{i'})(f_{i,j'}-\overline{f}_i)Cov(\delta_{i,j'},\delta_{i',j'})$$
$$= \sum_{j=-l}^{l}\Bigg(\frac{2(2l^2-1)}{(2l+1)^2}Cov(\delta_{i,j}^2,\delta_{i',j}^2) + 4(f_{i',j}-\overline{f}_{i'})(f_{i,j}-\overline{f}_i)Cov(\delta_{i,j},\delta_{i',j})$$
$$+\frac{2}{(2l+1)^2}\sum_{k=-l}^{l}Cov(\delta_{i,j}\delta_{i,k},\delta_{i',j}\delta_{i',k})\Bigg)$$
$$= \sum_{j=-l}^{l}\Bigg(\frac{4l^2}{(2l+1)^2}Cov(\delta_{i,j}^2,\delta_{i',j}^2) + 4(f_{i',j}-\overline{f}_{i'})(f_{i,j}-\overline{f}_i)Cov(\delta_{i,j},\delta_{i',j})$$
$$+\frac{2}{(2l+1)^2}\sum_{\substack{k=-l\\k\neq j}}^{l}Cov(\delta_{i,j}\delta_{i,k},\delta_{i',j}\delta_{i',k})\Bigg)$$

Then from the proof of lemma 6.10 and the fact that $Cov(\delta_{i,j}, \delta_{i',j'}) = \begin{cases} E(\delta_{i,j}\delta_{i',j}) & \text{if } j' = j \\ 0 & \text{o/w} \end{cases}$, we get

$$\begin{aligned}
\sum_{j=-l}^{l}\sum_{j'=-l}^{l} Cov(g_{i,j}, g_{i',j'}) &= \sum_{j=-l}^{l}\Bigg(\frac{4l^2}{(2l+1)^2}\left(E(\delta_{i,j}^2\delta_{i',j}^2) - E(\delta_{i,j}^2)^2\right) + 4(f_{i',j} - \overline{f}_{i'})(f_{i,j} - \overline{f}_i)E(\delta_{i,j}\delta_{i',j}) \\
&\qquad + \frac{2}{(2l+1)^2}E(\delta_{i,j}\delta_{i',j})\sum_{\substack{k=-l \\ k\neq j}}^{l} E(\delta_{i,k}\delta_{i',k})\Bigg) \\
&= \sum_{j=-l}^{l}\Bigg(\frac{4l^2}{(2l+1)^2}\left(E(\delta_{i,j}^2\delta_{i',j}^2) - E(\delta_{i,j}^2)^2\right) + 4(f_{i',j} - \overline{f}_{i'})(f_{i,j} - \overline{f}_i)E(\delta_{i,j}\delta_{i',j}) \\
&\qquad + \frac{2}{(2l+1)^2}E(\delta_{i,j}\delta_{i',j})\left(\sum_{k=-l}^{l} E(\delta_{i,k}\delta_{i',k}) - E(\delta_{i,j}\delta_{i',j})\right)\Bigg) \\
&= \sum_{j=-l}^{l}\Bigg(\frac{4l^2}{(2l+1)^2}\left(E(\delta_{i,j}^2\delta_{i',j}^2) - E(\delta_{i,j}^2)^2\right) + 4(f_{i',j} - \overline{f}_{i'})(f_{i,j} - \overline{f}_i)E(\delta_{i,j}\delta_{i',j})\Bigg) \\
&\qquad + \frac{2}{(2l+1)^2}\left(\left(\sum_{k=-l}^{l} E(\delta_{i,k}\delta_{i',k})\right)^2 - \sum_{j=-l}^{l} E(\delta_{i,j}\delta_{i',j})^2\right) \\
&= \sum_{j=-l}^{l}\Bigg(\frac{4l^2}{(2l+1)^2}\left(E(\delta_{i,j}^2\delta_{i',j}^2) - E(\delta_{i,j}^2)^2\right) - \frac{2}{(2l+1)^2}E(\delta_{i,j}\delta_{i',j})^2 \\
&\qquad + 4(f_{i',j} - \overline{f}_{i'})(f_{i,j} - \overline{f}_i)E(\delta_{i,j}\delta_{i',j})\Big) + \frac{2}{(2l+1)^2}\left(\sum_{k=-l}^{l} E(\delta_{i,k}\delta_{i',k})\right)^2
\end{aligned}$$

□

For convenvience, define $h_i := \sum_{j=-l}^{l} g_{i,j}$. Then

Lemma 6.15

$$\sum_{i'=-m}^{m} Cov(h_i, h_{i'}) = \frac{2n^4}{45(2l+1)^2}\left(\sum_{j=-l}^{l}\left[\left(8l^2-5\right)\left((1-\alpha_j)^4+\alpha_j^4\right)+\left(56l^2-20\right)(1-\alpha_j)^2\alpha_j^2\right]\right.$$
$$+\left(\sum_{k=-l}^{l}(1-2\alpha_k+2\alpha_k^2)\right)^2+2\left(\sum_{k=-l}^{l}(1-\alpha_k)\alpha_k\right)^2\Bigg)$$
$$+\frac{4n^2}{3}\left(\sum_{j=-l}^{l}(f_{i,j}-\overline{f}_i)\left((f_{i-1,j}-\overline{f}_{i-1}+f_{i+1,j}-\overline{f}_{i+1})(1-\alpha_j)\alpha_j\right.\right.$$
$$\left.\left.+(f_{i,j}-\overline{f}_i)(1-2\alpha_j+2\alpha_j^2)\right)\right)$$

Proof. First note that it is fairly simple to show $E(\delta_{i,j}\delta_{i',j}) = \begin{cases} \frac{n^2}{3}\left(1-2\alpha_j+2\alpha_j^2\right) & \text{if } i'=i \\ \frac{n^2}{3}(1-\alpha_j)\alpha_j & \text{if } i'=i\pm 1 \\ 0 & \text{o/w} \end{cases}$.

Furthermore, $E(\delta_{i,j}^2\delta_{i',j}^2) = \begin{cases} n^4\left(\frac{1}{5}(1-\alpha_j)^4+\frac{2}{3}(1-\alpha_j)^2\alpha_j^2+\frac{1}{5}\alpha_j^4\right) & \text{if } i'=i \\ n^4\left(\frac{1}{9}(1-\alpha_j)^4+\frac{14}{45}(1-\alpha_j)^2\alpha_j^2+\frac{1}{9}\alpha_j^4\right) & \text{if } i'=i\pm 1 \\ \frac{n^4}{9}\left((1-\alpha_j)^2+\alpha_j^2\right)^2 & \text{o/w} \end{cases}$, which is also a simple but tedious calculation. Note the nontrivial case when $|i-i'|>1$.

From this, we get

$$\begin{aligned}
\sum_{i'=-m}^{m} Cov(h_i, h_{i'}) &= \sum_{i'=-m}^{m} \Bigg[\sum_{j=-l}^{l} \Bigg(\frac{4l^2}{(2l+1)^2} \left(E(\delta_{i,j}^2 \delta_{i',j}^2) - E(\delta_{i,j}^2)^2 \right) - \frac{2}{(2l+1)^2} E(\delta_{i,j}\delta_{i',j})^2 \\
&\qquad +4(f_{i',j} - \overline{f}_{i'})(f_{i,j} - \overline{f}_i) E(\delta_{i,j}\delta_{i',j}) \Big) + \frac{2}{(2l+1)^2} \left(\sum_{k=-l}^{l} E(\delta_{i,k}\delta_{i',k}) \right)^2 \Bigg] \\
&= \sum_{j=-l}^{l} \Bigg(\frac{2}{(2l+1)^2} \Big[2l^2 \left(E(\delta_{i,j}^2 \delta_{i-1,j}^2) + E(\delta_{i,j}^4) + E(\delta_{i,j}^2 \delta_{i+1,j}^2) \right) - (6l^2+1) E(\delta_{i,j}^2)^2 \\
&\quad - \left(E(\delta_{i,j}\delta_{i-1,j})^2 + E(\delta_{i,j}\delta_{i+1,j})^2 \right) \Big] \\
&\quad +4(f_{i,j} - \overline{f}_i) \left((f_{i-1,j} - \overline{f}_{i-1}) E(\delta_{i,j}\delta_{i-1,j}) + (f_{i,j} - \overline{f}_i) E(\delta_{i,j}^2) + (f_{i+1,j} - \overline{f}_{i+1}) E(\delta_{i,j}\delta_{i+1,j}) \right) \Big) \\
&\quad + \frac{2}{(2l+1)^2} \left(\left(\sum_{k=-l}^{l} E(\delta_{i,k}\delta_{i-1,k}) \right)^2 + \left(\sum_{k=-l}^{l} E(\delta_{i,k}^2) \right)^2 + \left(\sum_{k=-l}^{l} E(\delta_{i,k}\delta_{i+1,k}) \right)^2 \right) \\
&= \frac{2n^4}{45(2l+1)^2} \Bigg(\sum_{j=-l}^{l} \left[\left(8l^2 - 5\right) \left((1-\alpha_j)^4 + \alpha_j^4 \right) + \left(56l^2 - 20\right) (1-\alpha_j)^2 \alpha_j^2 \right] \\
&\quad + \left(\sum_{k=-l}^{l} (1 - 2\alpha_k + 2\alpha_k^2) \right)^2 + 2 \left(\sum_{k=-l}^{l} (1-\alpha_k)\alpha_k \right)^2 \Bigg) \\
&\quad + \frac{4n^2}{3} \left(\sum_{j=-l}^{l} (f_{i,j} - \overline{f}_i) \left((f_{i-1,j} - \overline{f}_{i-1} + f_{i+1,j} - \overline{f}_{i+1})(1-\alpha_j)\alpha_j + (f_{i,j} - \overline{f}_i)(1 - 2\alpha_j + 2\alpha_j^2) \right) \right)
\end{aligned}$$

□

Theorem 6.16

$$V(var_{\tilde{f}}(\epsilon)) = \frac{2n^4}{9(2l+1)^4(2m+1)} \left(\sum_{j=-l}^{l} \left[\left(\frac{8l^2}{5} - 1 \right) \left((1-\alpha_j)^4 + \alpha_j^4 \right) + \left(\frac{56l^2}{5} - 4 \right) (1-\alpha_j)^2 \alpha_j^2 \right] \right.$$
$$\left. + \left(\sum_{k=-l}^{l} (1 - 2\alpha_k + 2\alpha_k^2) \right)^2 + 2 \left(\sum_{k=-l}^{l} (1-\alpha_k)\alpha_k \right)^2 \right)$$
$$+ \frac{4n^2}{3(2l+1)^2(2m+1)^2} \left(\sum_{i=-m}^{m} \sum_{j=-l}^{l} (f_{i,j} - \overline{f}_i) \left((f_{i-1,j} - \overline{f}_{i-1} \right. \right.$$
$$\left. \left. + f_{i+1,j} - \overline{f}_{i+1})(1-\alpha_j)\alpha_j + (f_{i,j} - \overline{f}_i)(1 - 2\alpha_j + 2\alpha_j^2) \right) \right)$$

Proof. Just using $\mathrm{V}(var_{\tilde{f}}(\epsilon)) = \frac{1}{(2l+1)^2(2m+1)^2} \sum_{i=-m}^{m} \sum_{k=-m}^{m} Cov(h_i, h_k)$ and the previous lemmas, we get the desired result. □

To complete our analysis of the variance, we also want to see what happens as $l \to \infty$ like we did with the expectation.

Lemma 6.17 $\lim_{l \to \infty} V(var_{\tilde{f}}(\epsilon)) = 0$

Proof. Since $|\alpha_j(\epsilon)| < 1$, and $f_{i,j}, \overline{f}_i$ are data and hence, bounded, the result is trivial. □

As noise, n_0 increases, the interpolated $var_{\tilde{f}}(\epsilon)$ becomes distorted due to the lack of interpolation for certain ϵ. For example, as discussed earlier, if $\epsilon = 0, \pm 1$, then none of the data points are interpolated resulting in the largest peaks seen in Figure 6.5. This can be particularly troublesome if the desired $\epsilon_0 = 0, \pm 1$, since there the minimum will never be achieved at these locations. Furthermore, as noise increases, these peaks also increase.

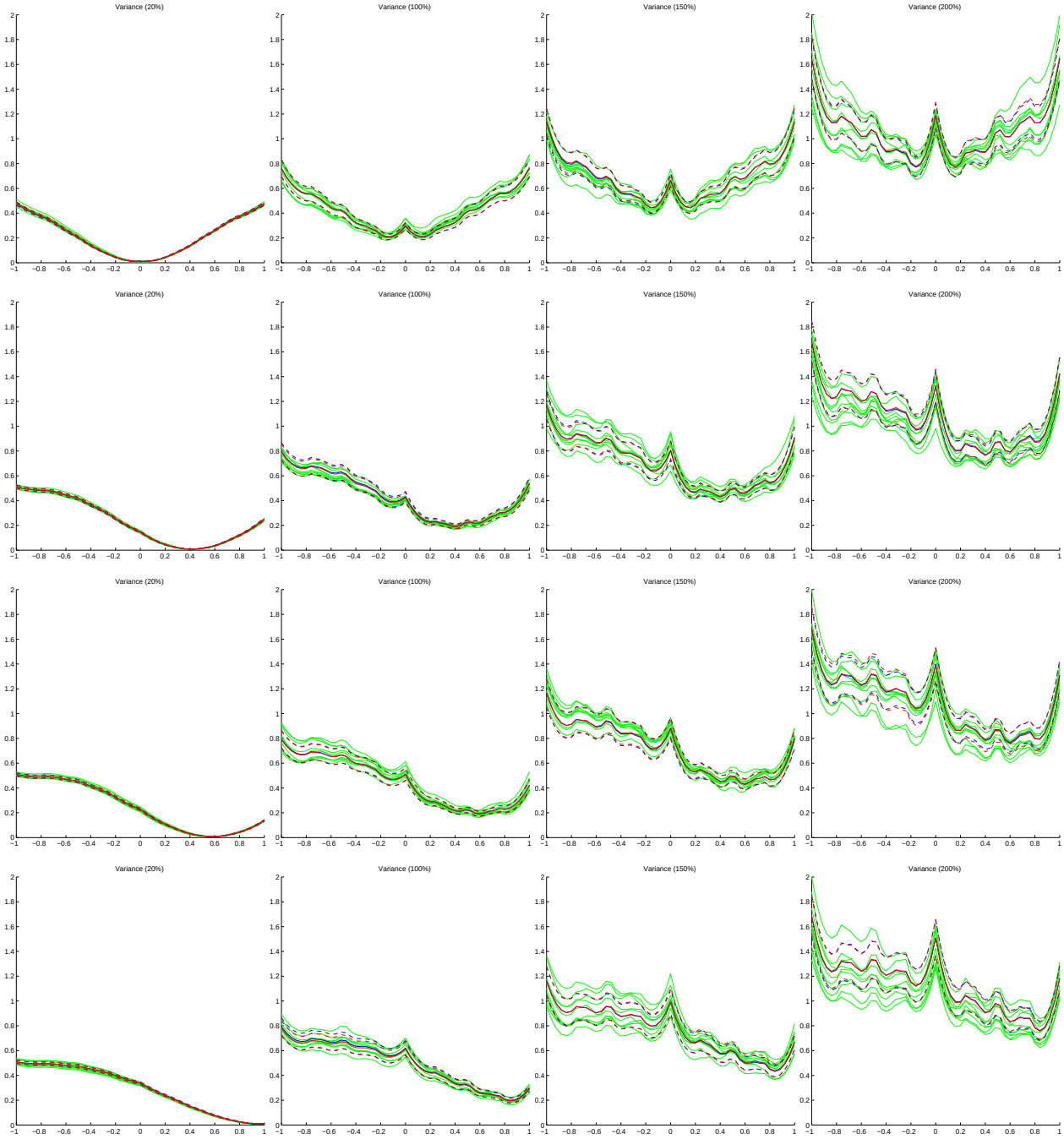

Figure 6.5: var vs noise. Each row corresponds to the angles of 0, $\frac{\pi}{8}$,$\frac{\pi}{6}$, and $\frac{\pi}{4}$. The columns correspond to noise levels of 20%,100%,150%, and 200%. The green lines are sample variances. The blue lines are calculated expectation, μ, (solid) and calculated standard deviation from the expectation, $\mu \pm \sigma$, (dashed). The red lines are sample expectation, μ, (solid) and sample standard deviation from the expectation, $\mu \pm \sigma$, (dashed) using a 100 samples.

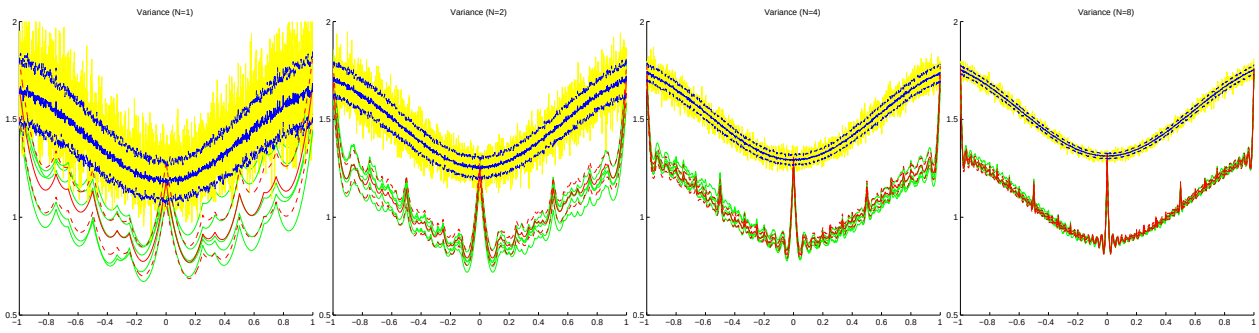

Figure 6.6: var as $l, m \to \infty$. The figures correspond to $l = 4, 8, 16$, and 32 and $m = 2l$. The green lines are sample variances with interpolation. The yellow lines are sample variances without interpolation. The red lines are sample expectation, μ, (solid) and one standard deviation from the expectation, $\mu \pm \sigma$, (dashed) for the interpolated set using a 100 samples. The blue lines are sample expectation, μ, (solid) and one standard deviation from the expectation, $\mu \pm \sigma$, (dashed) for the noninterpolated set using a 100 samples. The noise level is 200%. In these images the resolution is increased to show the peaks caused at the rational numbers.

The shape of these peaks are more distinct if we increase the number of data points in S, i.e. let $l, m \to \infty$, while keeping L_x, L_y constant (see Figure 6.6), which is consistent with Theorem 6.7. In particular, we see that the at $\epsilon = 0$, the expected variance for the interpolated data which closely matches the expected value of the non-interpolated data. This is expected since no interpolation takes place at $\epsilon = 0$. Furthermore, we see how the variance of $var_{\tilde{f}}(\epsilon)$ approaches 0 for both the interpolated and non-interpolated set.

Note that the non-interpolated graphs were created by making the data points such that the shifted data points match precisely with the created data. This is not possible for given experimental data.

We can also compare the the interpolated $var_{\tilde{f}}(\epsilon)$ with the non-interpolated $var_{\tilde{f}}(\epsilon)$ for varying angles. From Figure 6.7, the interpolated graph is smoother because it averages out the noise, even though the average of the non-interpolated graph gives the most desirable function to minimize. Also, note that at $\epsilon = 0, \pm 1$, the interpolated and non-interpolated graphs are the same as expected.

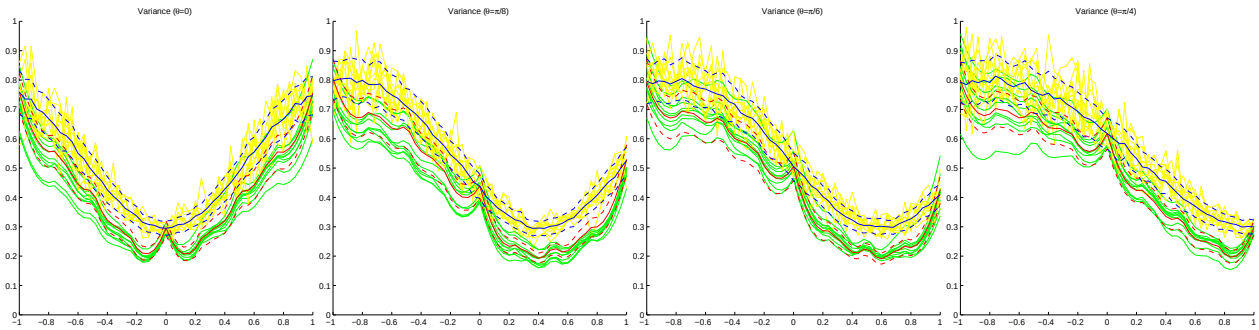

Figure 6.7: Interpolated var vs Non-interpolated var. The figures correspond to the angles of 0, $\frac{\pi}{8}$,$\frac{\pi}{6}$, and $\frac{\pi}{4}$. The green lines are sample variances with interpolation. The yellow lines are sample variances without interpolation. The red lines are sample expectation, μ, (solid) and one standard deviation from the expectation, $\mu \pm \sigma$, (dashed) for the interpolated set using a 100 samples. The blue lines are sample expectation, μ, (solid) and one standard deviation from the expectation, $\mu \pm \sigma$, (dashed) for the noninterpolated set using a 100 samples. The noise level is 100%.

Bibliography

[1] Abramowitz, M. and Stegun, I., *Handbook of Mathematical Functions with Formulas, Graphs, and Mathematical Tables*, U.S. Department of Commerce.

[2] Asbach, P., Klatt, D., Hamhaber, U., Braun, J., Somasundaram, R., Hamm, B., Sack, I., Assessment of liver viscoelasticity using multifrequency MR Elastography, *Magnetic Resonance in Medicine*, 60 (2008), pp. 373-379.

[3] Anderssen R.S. and Hegland, M., For Numerical Differentiation, Dimensionality Can Be a Blessing, *Mathematics of Computation*, vol. 68, num. 227 (1999), pp. 1121-1141.

[4] Angell, T., Kleinman, R., and Hettlich, F., The resistive and conductive problems for the exterior Helmholtz equation, *SIAM J. Appl. Math.*, vol. 50 (1990), pp. 1607–1622.

[5] Arridge, S.R., Optical tomography in medical imaging, *Inverse Problems*, 15 (1999), R41-R93.

[6] Bates, G.E., Joint distributions of time intervals for the occurrence of succesive accidents in a generalized Polya urn scheme, *Annals of Mathematical Statistics*, 26 (1955), pp. 705–720.

[7] Charlier J.P. and Crowet, F., Wave equations in linear viscoelastic materials, *J. Acoust. Soc. Am.* 79(4) (April 1986), pp. 895-900.

[8] Cheney, M., Isaacson, D., and Newell, J., Electrical Impedance Tomography, *SIAM Review*, 41(1) (1999), pp. 85-101.

[9] Colton, D. and Kress, R., *Inverse Acoustic and Electromagnetic Scattering Theory*, Berlin: Springer-Verlag, 1992.

[10] Fung, Y. C., *Biomechanics: Mechanical Properties of Living Tissues*, 2nd ed., New York: Springer-Verlag, 1993.

[11] Klatt, D., Hamhaber, U., Asbach, P., Braun, J., and Sack, I., Noninvasive assessment of the rheological behavior of human organs using multifrequency MR elastography: a study of brain and liver viscoelasticity, *Phys. Med. Biol.*, vol. 52 (2007), pp. 7281-7294.

[12] Korner, T.W., *Fourier Analysis*, Cambrige University Press, (1986), pp.11

[13] Kress, R. and Roach, G., Transmission problems for the Helmholtz equation, *J. Math. Phys.*, vol. 19 (1978), pp. 1433–1437.

[14] Manduca, A., Lake, D., and Ehman, R., Improved inversion of MR elastography images by spatiotemporal directional filtering, *Proc. SPIE Int. Soc. Opt. Eng.*, 5032 (2003), pp.445–452.

[15] Manduca, A., Lake, D., Kruse, S., and Ehman, R., Spatio-temporal directional filtering for improved inversion of MR elastography images, *Med. Image Anal.*, 7 (2003), pp. 465–473.

[16] Manduca, A., Oliphant, T., Dresner, M., Mahowald, J., Kruse, S., Amromin, E., Felmlee, J., Greenleaf, J., and Ehman, R., Magnetic resonance elastography: Noninvasive mapping of tissue elasticity. *Med. Image Anal.*, 57 (2001), pp. 237–254.

[17] McCracken, P., Manduca, A., Felmlee, J., and Ehman,L., Mechanical transient-based magnetic resonance elastography, *Magnetic Resonance in Medicine*, 53 (2005), pp. 628–639.

[18] Mclaughlin J., Renzi D., and J.R. Yoon, Variance Controlled Shear Stiffness Images for MRE Data, 3rd IEEE International Symposium on Biomedical Imaging: Nano to Macro (2006), pp.960-963.

[19] McLaughlin, J., Oberai, A., Yoon, J., Formulas for detecting a spherical stiff inclusion from interior data: a sensitivity analysis for the Helmholtz equation, *Inverse Problems*, 084004 (21pp) (2012).

[20] Mukhopadhyay, N., *Probability and Statistical Inference*, Marcel Dekker Inc. (2000), pp. 149–150.

[21] Muthupillai, R. and Ehman, R., Magnetic resonance elastography. *Nature Medicine*, 2(1996), pp. 601–603.

[22] Muthupillai, R., Lomas, D., Rossman, P., Greenleaf, J., Manduca, A., and Ehman R., Magnetic resonance elastography by direct visualization of propagating acoustic strain waves, *Science*, vol. 269 (1995), pp. 1854–1857.

[23] Oliphant, T., Kinnick, R., Manduca, A., Ehman, R., and Greenleaf, J., An error analysis of Helmholtz inversion for incompressible shear, vibration elastography with application to filter-design for tissue characterization. *Proc. IEEE Ultrason. Symp.*, (2000), pp. 1795–1798.

[24] Oliphant, T., Manduca, A., Ehman, R. and Greenleaf, J., Complex-valued stiffness reconstruction for magnetic resonance elastography by algebraic inversion of the differential equation. *Magnetic Resonance in Medicine*, 45(2001), pp.299–310.

[25] Rouviere, O., Yin, M., Dresner, M., Rossman, P., Burgart, L., Fidler, J., and Ehman, R., MR elastography of the liver: Preliminary results. *Radiology*, 240(2006), pp.440–448.

[26] Sinkus, R, Tanter, M., Xydeasc, T., Catheline, S., Bercoff, J., and Fink, M., Viscoelastic shear properties of in vivo breast lesions measured by MR elastography, *Magnetic Resonance Imaging*, vol. 23 (2005), pp. 159-165.

[27] Watson, G.,*A Treatise on the Theory of Bessel Functions*, Cambridge University Press, 1995.

[28] White, C., *Sensitivity Analysis and Detectability for Magnetic Resonance Elastography*, Clemson University (2012).

[29] Van Houten, E., Doyley, M., Kennedy, F., Weaver, J., and Paulsen, K., Initial in vivo experience with steady-state subzone-based MR elastography of the human breast, *J. Magn. Reson. Imaging*, 17(2003), pp. 7285.

[30] Van Houten, E., Doyley, M., Kennedy, F., Weaver, J., and Paulsen, K., Elasticity reconstruction from experimental mr displacement data: Initial experience with an overlapping sub zone finite element inversion process, *Med. Phys.*, 27(2000), pp. 101107.